2016

Aeroelastic Investigation of a Circumferentially Varying Tip Gap in an Axial Compressor Rotor

Ornan David Canon
University of Central Florida

AEROELASTIC INVESTIGATION OF A CIRCUMFERENTIALLY VARYING TIP GAP IN AN AXIAL COMPRESSOR ROTOR

by

DAVID CAÑÓN
B.S.M.E. University of Illinois – Chicago, 1999
M.S.A.E. University of Cincinnati, 2002

A dissertation submitted in partial fulfillment of the requirements
for the degree of Doctor of Philosophy
in the Department of Mechanical and Aerospace Engineering
in the College of Engineering and Computer Science
at the University of Central Florida
Orlando, Florida

Summer Term
2016

Major Professor: Jayanta Kapat

ABSTRACT

The tip leakage flow in axial compressors is a significant factor in engine performance and a subject of investigation over the last several decades. Many studies have already shown that the vortices generated by this tip leakage can have a negative impact on the surrounding flow field and overall performance, and could potentially lead to excitations as well. This study examines the effect of these vortices on aeroelasticity. Specifically, it looks at the effect from a circumferentially varying tip gap, such as that produced by casing ovalization.

For this project, the casing ovalization of an industrial gas turbine compressor was modeled using a frequency domain solver, without the need for a full wheel model. Both the vibratory and aerodynamic calculations were conducted in order to assess the aeroelastic response of the blade, as well as the aerodynamic impact. Engine test data was implemented in order to model realistic levels of casing ovalization and to calibrate the analytical models. Comparisons to a well-established method are also conducted to further calibrate the models.

The calculations showed that for the gap variations imposed, the instantaneous effects aligned with expectations. However, the variation from small and large gaps had a canceling effect on each other over the cycle of oscillation around the engine.

To My Family

ACKNOWLEDGMENTS

First and foremost I would like to thank God, through whom all things are possible. In the words of Bach: *Soli Deo Gloria*

I would also like to express my sincere gratitude to my advisor Dr. Kapat for his help and support over the past few years. His guidance and discussions on the technical matters were very valuable and much appreciated, as well as his patience and support on the logistical difficulties and extended length of this work…thank you.

This work was made possible by the support of Siemens Energy Inc., both in the financial backing, as well as the technical assistance and permission to use their data. I would like to acknowledge the many colleagues in the Compressor and MT departments at Siemens for their contributions in various aspects of this work, specifically Bernhard Kuesters, Marc Mittelbach and Eric Berrong for supporting me throughout this undertaking. Special thanks as well to Dr. Hans-Juergen Kiesow, Dr. Matt Montgomery and Dr. Stefan Schmitt for the many useful discussions. Dr. Chad Custer and Cassandra Carpenter from CD-Adapco also played an instrumental role in providing technical support and advice.

TABLE OF CONTENTS

LIST OF FIGURES

LIST OF TABLES

NOMENCLATURE

BB	Blade to Blade
BC	Boundary Condition
CFD	Computational Fluid Dynamics
CPU	Central Processing Unit
DLR	Deutsches Zentrum für Luft- und Raumfahrt (German Aerospace Center)
DOF	Degree of Freedom
E	Energy
EO	Engine Order
FE	Finite Element
GPU	Graphical Processing Unit
HB	Harmonic Balance
HCF	High Cycle Fatigue
LE	Leading Edge
ND	Nodal Diameter
NSV	Non-Synchronous Vibration
OEM	Original Equipment Manufacturer
P	Pressure
PS	Pressure Side
Pt	Total Pressure
R	Radius
SS	Suction Side

T	Temperature
TE	Trailing Edge
V	Velocity
c	Damping Coefficient
k	Spring Constant
m	Mass
s	Entropy
u	Velocity, X-Component
v	Velocity, Y-Component
w	Velocity, Z-Component
Ω	Rotor Speed
β	Tangential Angle
ϕ	Nodal Displacement
γ	Radial Angle
η	Efficiency
θ	Theta (circumferential coordinate)
ρ	Density
ω	Frequency of Vibration
ζ	Critical Damping Ratio

CHAPTER 1: INTRODUCTION

1.1 Background

Radial tip gaps in axial compressors are well known to have a significant impact on engine performance and operability. There are many factors that influence these gaps, such as manufacturing, assembly, engine operation, etc. However, this study will concentrate on casing ovalization and how it affects the flow through these gaps.

Casing ovalization is important because it can generate a circumferentially varying tip gap. This can potentially have a negative impact on the aeroelastic response of the rotor blades; this is the focus of this study. The difficulty with ovalization in the context of aeromechanics is that it requires at least a half wheel unsteady simulation of the flow, which can be very expensive.

Traditionally, these types of flows have been studied using single passage models, either single-row or multi-row, both steady and unsteady, as shown in Zhang [1] and Du [2]. Other papers have dealt with full annulus simulations ranging from one to a few rows, but mostly steady calculations. For examples, see Kang [3], Im [4], and Chen [5].

More recently, unsteady CFD (Computational Fluid Dynamics) using frequency domain solvers has become more popular due to the time/cost savings associated with them. Reductions of 1 to 2 orders of magnitude over time domain solvers were reported by Hall [67]. However, these types of solvers (either time linearized or harmonic balance) have been mostly applied to the standard turbomachinery configuration (single passage, constant gap, single or multi row), as in Moffatt [6] and Moffatt [7]. Another

emerging topic of research in CFD is utilizing GPU's (Graphical Processing Unit) to run full wheel, multi-row models, Pullan [15]. This approach holds a lot of promise in terms of run-time, with a savings factor of 10 reported by Brandvik [73]. However, the use GPU's in CFD has only been introduced in the last few years, and has not been widely adopted in industry yet.

For this study, the unsteady flow field emerging from a circumferentially varying tip gap is modeled using a Harmonic Balance solver. Mailach [8] has shown that this particular type of flow generates vortical structures migrating from the PS to the SS (through the tip gap), which have a strong influence on compressor efficiency and stability margin. These vortices are a function of the gap size, Kang [9], so a circumferentially varying tip gap is expected to generate vortical structures that vary circumferentially as well. This is important in terms of aeroelasticity because the tip vortex could be altered (by the gap variation) to be in phase with the natural frequency of the blade, pushing it into resonance. A related scenario of vortex induced vibration has long been studied for circular cross section bodies, Au-Yang [12], and is still under study for airfoils and other non-standard shapes independent of any gap, Besem [10] and Fric [13]. The presence of the tip gap in the present study is a complicating factor; the circumferentially variation of this gap compounds the problem even more.

As new gas turbine designs are expected to increase blade loadings, it will become more important to accurately model and predict the aeromechanic response of airfoils in order to retain dynamic integrity. This is a difficult challenge that is not expected to be thoroughly solved within the scope of this project. Nevertheless, the aim here is to take

an initial step toward modeling it in a practical manner and assessing the impact on the aeromechanic response of the blade.

1.2 Rotor Tip Clearance

The rotor tip clearance refers to the gap between the rotating airfoil and the stationary casing inside of a gas turbine engine. Figure 1.1 shows a schematic of a compressor rotor disk, airfoil (rotating airfoils are also called blades, stationary ones are called vanes) and casing. It is obvious that in order to have the airfoil rotating relative to the stationary casing, there must be a physical “radial gap” between the blade tip and the casing; this is the tip clearance (or tip gap).

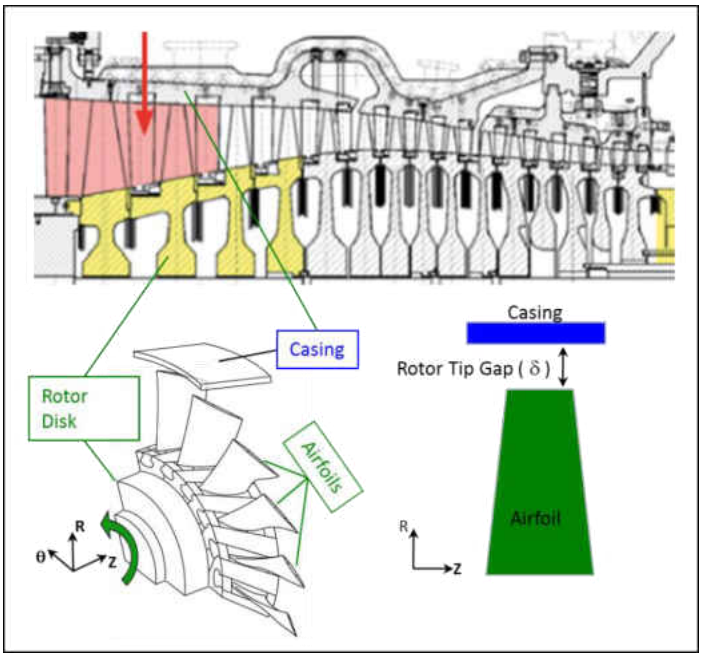

Figure 1.1: Tip Clearance Schematic

In principle, there would be no gap at all for optimum performance. However, due to manufacturing tolerances, engine assembly and operability, some amount of gap is unavoidable. Consequently, different interactions arise in terms of the compressor aerodynamics as well as thermo-mechanical considerations, some of which will be discussed in chapter 2. These interactions make tip gaps both critical to performance, as well as very difficult to analyze.

1.3 Aerodynamic Considerations

The field of Aerodynamics studies the movement of air and the interaction with the bodies it surrounds. This section gives a brief description of some of the main aerodynamic concepts relevant to this project. For the sake of discussion, these concepts are presented in a manner simplified from the actual implementation in this project. For a more complete treatment on the subject, the reader is referred to Platzer [16], Tannehill [17], Cumpsty [18] and Verdon [19].

1.3.1 Steady vs. Unsteady

Within the context of the rotor tip gap flow, the behavior of air is inherently time dependent, as will be discussed later. This is where a major distinction in aerodynamics is made, whether the flow can be assumed to be constant over time (steady), or if time dependencies need to be considered (unsteady). From the computation point of view, a steady flow can be described as converging toward a single value as the solution

marches in time. By contrast an unsteady flow will not converge toward a single value, as shown schematically in Figure 1.2.

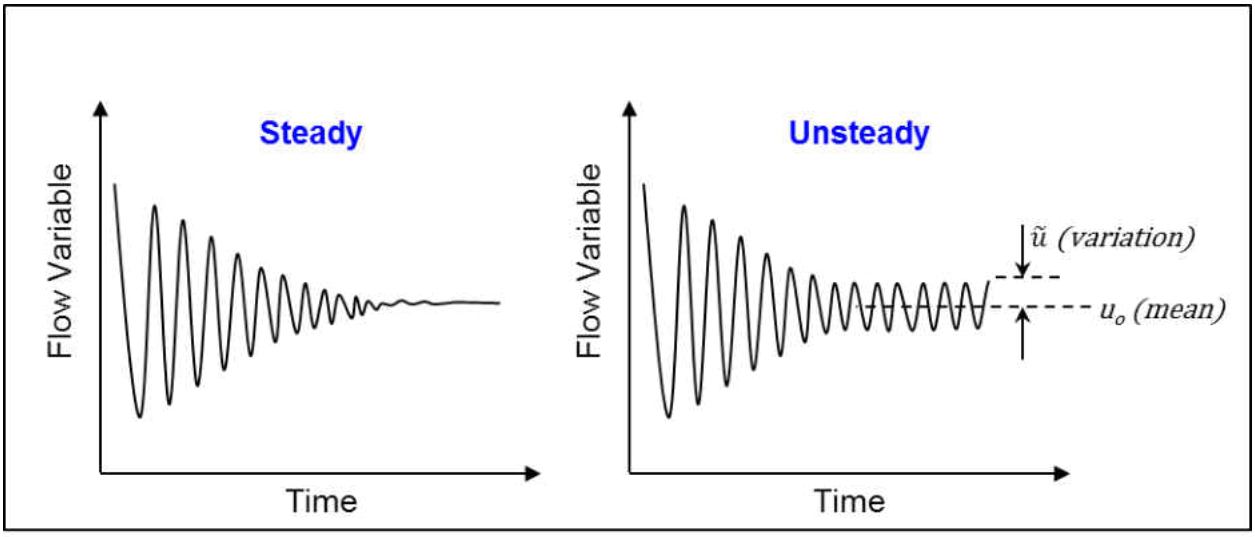

Figure 1.2: Steady vs. Unsteady Flow

The unsteady flow could be either stochastic, or become periodic in time, as shown in the figure. In the latter case, the flow is described as having a variation ($\tilde{u}$) that oscillates about a mean (u_o). This type of periodic unsteady flow is very common in turbomachinery (as well as in other disciplines) and appropriate to be analyzed using a frequency domain approach. This is where a sub-division in unsteady aerodynamics is made, in the way in which time is resolved. Currently the two main approaches for dealing with unsteady aerodynamics are time domain and frequency domain.

1.3.2 Time Domain

The time domain analysis has been the traditional approach and still the more common due to its versatility. It is well established and applicable to many different problems, although it's the more computationally expensive of the two.

For simplification, the flow is assumed to be a 2D Newtonian fluid without heat addition. The continuity equation, together with the equations of motion (Navier-Stokes), energy and state (Equations 1.1 through 1.5) provide a complete description for this idealized flow.

$$\frac{\partial \rho}{\partial t} + \frac{\partial (\rho u)}{\partial x} + \frac{\partial (\rho v)}{\partial y} = 0 \qquad (1.1)$$

$$\rho\left(\frac{\partial u}{\partial t} + u\frac{\partial u}{\partial x} + v\frac{\partial u}{\partial y}\right) = -\frac{\partial p}{\partial x} + \rho g_x + \mu\left(\frac{\partial^2 u}{\partial x^2} + \frac{\partial^2 u}{\partial y^2}\right) \qquad (1.2)$$

$$\rho\left(\frac{\partial v}{\partial t} + u\frac{\partial v}{\partial x} + v\frac{\partial v}{\partial y}\right) = -\frac{\partial p}{\partial y} + \rho g_y + \mu\left(\frac{\partial^2 v}{\partial x^2} + \frac{\partial^2 v}{\partial y^2}\right) \qquad (1.3)$$

$$\frac{\partial E}{\partial t} + \frac{\partial}{\partial x}\left(Eu + pu - u\tau_{xx} - v\tau_{xy}\right) + \frac{\partial}{\partial y}\left(Ev + pv - u\tau_{xy} - v\tau_{yy}\right)$$

$$= \rho(f_x u + f_y v) \qquad (1.4)$$

$$p = \rho RT \qquad (1.5)$$

These are nonlinear, second order, partial differential equations not amenable to an exact solution. For illustrative purposes, further simplifications are made; viscosity

and body forces will be neglected, reducing this problem to a 2D Euler formulation. Finally, the conservation-law equations are written in vector form:

$$\frac{\partial U}{\partial t} + \frac{\partial E}{\partial x} + \frac{\partial F}{\partial y} = 0 \qquad (1.6)$$

Where:

$$U = \begin{bmatrix} \rho \\ \rho u \\ \rho v \\ E \end{bmatrix} \qquad (1.7)$$

$$E = \begin{bmatrix} \rho u \\ \rho u^2 + p \\ \rho uv \\ (E_t + p)u \end{bmatrix} \qquad (1.8)$$

$$F = \begin{bmatrix} \rho v \\ \rho uv \\ \rho v^2 + p \\ (E_t + p)v \end{bmatrix} \qquad (1.9)$$

$$E_t = \rho(e + \frac{V^2}{2} + Potential\ Energy) \qquad (1.10)$$

The next steps are to non-dimensionalize Equation (1.6) and discretize the flow domain in both time and space. The solution is then marched in physical time until a prescribed convergence criteria is met. This approach is relatively straightforward, which makes it manageable to code and applicable to many types of flows. Also, since it

is non-linear, it captures both linear and non-linear effects. It has been commonly used in the field of computational fluid dynamics, so there are many widely accepted and well established solving techniques.

1.3.3 Frequency Domain

The second approach to handle unsteady aerodynamics is to solve in the frequency domain rather than in time. This type of approach has been around for a while, predominantly in the field of electronics. However, in recent years researchers have been applying this technique to unsteady CFD. In the frequency domain approach, the periodic behavior of the flow is leveraged to transform the governing equations such that the conserved variables are posed as a Fourier series in time, and the Fourier coefficients solved. Obviously this approach is only valid for flows that are naturally periodic. Fortunately, the unsteady flows in discussion display such behavior. Solving in the frequency domain is advantageous because it is more efficient than an equivalent time domain approach by one to two orders of magnitude. Also, the description of acoustic, vortical and entropic waves is simplified, according to Hall [65]. Today there are two main approaches when solving in the frequency domain: time-linearized and harmonic balance.

1.3.3.1 Time Linearized

In this first sub-division, the state variables are broken into two parts: a non-linear steady component (u_o), and a small linear perturbation ($\tilde{u}$). The small perturbation is assumed to be harmonic in time, so that Equation (1.6) can be re-written as:

$$\frac{\partial \hat{U}}{\partial t} + \frac{\partial \hat{E}}{\partial x} + \frac{\partial \hat{F}}{\partial y} = 0 \qquad (1.11)$$

Where:

$$\hat{U}(\vec{x}, t) = U(\vec{x}) + u(\vec{x})e^{i\omega t} \qquad (1.12)$$

Making the appropriate substitutions and collecting the zeroth order (steady), and first order (linear unsteady) terms, results in the linearized Euler equations, as described by Hall [65]:

$$\frac{\partial \boldsymbol{u}}{\partial \tau} + i\omega \boldsymbol{u} + \frac{\partial}{\partial x}\left(\frac{\partial \boldsymbol{F}}{\partial \boldsymbol{U}}\boldsymbol{u}\right) + \frac{\partial}{\partial y}\left(\frac{\partial \boldsymbol{G}}{\partial \boldsymbol{U}}\boldsymbol{u}\right) = 0 \qquad (1.13)$$

The addition of the first term by Ni [66], make the equations hyperbolic in pseudo time τ. This allows for the use of traditional time marching solvers that iterate this term to zero. Of course this approach can then be extended to 3D and viscous flows, as implemented in the codes used for this project.

The implementation of this technique by DLR's LinearTrace code requires that the steady solution be provided as input to the unsteady calculation. The perturbation quantities are then solved in a time comparable to the steady solution. So the steady

solution is used to calculate the perturbation, but itself is not changed during the unsteady calculation.

1.3.3.2 Harmonic Balance

The second subdivision in frequency domain solvers is the harmonic balance approach. This is similar to the linearized technique, with a notable improvement that allows it to capture more of the physics. The harmonic balance is capable of modeling non-linearities, which are by definition missed in the linearized approach. Another advantage of harmonic balance over the linearized approach is that the harmonic balance calculates both the steady and unsteady in the same solution. So the steady component is updated by the unsteady calculation.

For simplicity, the flow considered will be again 2D inviscid, periodic in time. The temporal periodicity is given by:

$$U(x, y, t) = U(x, y, t + T) \quad (1.14)$$

In this equation, T is the period of the unsteadiness. Spatial periodicity could also be applied (though not required in StarCCM+), as expressed in terms of the pitch, $\Delta\theta$.

$$U(x, y + \Delta\theta, t) = U(x, y, t + \Delta T) \quad (1.15)$$

Where ΔT is the time lag associated with the flow unsteadiness. In other words, the flow in a given passage varies in time, and the flow in the adjacent row is a copy of the

first, but lagged in time. The time variation is assumed to be harmonic so that the flow can be represented by a trigonometric series, as shown in Equation (1.16)

$$w(\vec{x}, t) = w_0(\vec{x}) + \sum_{n=1}^{M} A_n \cos(\omega n t) + B_n \sin(\omega n t) \qquad (1.16)$$

In this equation:

w_0 represents the "Steady" or "Mean" solution at point $\vec{x} = (x, y)$

A_n & B_n are the Fourier Coefficients

ω is the frequency of the unsteadiness

M is the number of modes or harmonics retained in the solution

Equation (1.16) can be substituted into the conserved variables of the governing equations, hence transforming them from unsteady time periodic, into steady non-linear Fourier series equations. Similar to the linearized approach, a fictitious time is introduced in order to apply conventional CFD techniques to solve the resulting vector equations, and iterate this pseudo time to zero.

1.4 Structural Dynamics

The structural part of the aeroelasticity problem can be as challenging as the aerodynamic portion. However, it is probably more common, or at least seems more familiar since structural analyses have a wider implementation in a large variety of engineering problems. Industries ranging from civil engineering to almost any kind of machine design have been implementing structural theories long before the

development of airfoil theory back in the late 1800's. This chapter will give a brief overview of the structural aspect of aeromechanics, specifically vibratory analysis; more details can be found in Thomson [62] and Takacs [63].

As a simplification for illustrative purposes, a one degree of freedom oscillator is considered, as shown in Figure 1.3.

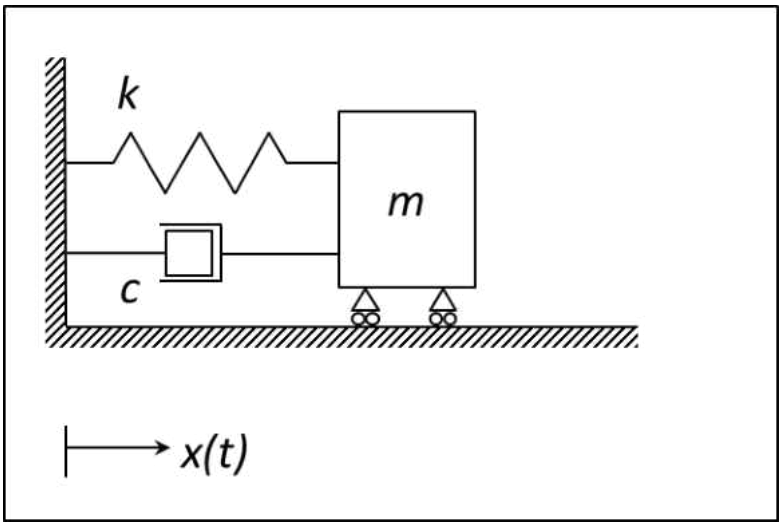

Figure 1.3: Single Degree of Freedom Oscillator

The system consists of a linear spring (constant k), and a viscous damper (coefficient c) attached to a mass (m) sliding along the *x* direction without friction. From Newton's Second Law, the inertial, damping and spring forces must balance out:

$$F_{Inertia} + F_{Damper} + F_{Spring} = 0 \qquad (1.17)$$

$$m\ddot{x} + c\dot{x} + kx = 0 \qquad (1.18)$$

The assumed solution to the differential equation takes the form:

$$x = Xe^{\lambda t} \quad (1.19)$$

$$\dot{x} = X\lambda e^{\lambda t} \quad (1.20)$$

$$\ddot{x} = X\lambda^2 e^{\lambda t} \quad (1.21)$$

Substituting back into Equation (1.18)

$$Xe^{\lambda t}(m\lambda^2 + c\lambda + k) = 0 \quad (1.22)$$

For the term in parenthesis to equal zero, the solution must have two roots

$$\lambda_{1,2} = \frac{-c}{2m} \pm \sqrt{\left(\frac{c}{2m}\right)^2 - \frac{k}{m}} \quad (1.23)$$

The term *k/m* is defined as ω^2, which is recognized as the natural frequency for an undamped system (*c=0*). Also, for the term inside the radical there are three possibilities:

a) $\left(\frac{c}{2m}\right)^2 > \frac{k}{m}$: The solution has all real numbers and it represents an overdamped system, so there are no oscillations.

b) $\left(\frac{c}{2m}\right)^2 < \frac{k}{m}$: The solution has an imaginary exponent and it represents an underdamped system, so it oscillates

c) $\left(\frac{c}{2m}\right)^2 = \frac{k}{m}$: This is the boundary between the previous two conditions. It represents a critically damped system. For this case the critical damping can be defined as:

$$\left(\frac{c_c}{2m}\right)^2 = \frac{k}{m} \quad (1.24)$$

$$c_c = 2m\sqrt{\frac{k}{m}} = 2m\omega \quad (1.25)$$

The critical damping ratio is defined as:

$$\zeta = \frac{c}{c_c} = \frac{c}{2m\omega} \quad (1.26)$$

Plugging back into Equation (1.23)

$$\lambda_{1,2} = -\omega\left(\zeta \pm \sqrt{\zeta^2 - 1}\right) \quad (1.27)$$

The final solution to the original equation then becomes:

$$x = e^{-\zeta\omega t}\left(Ae^{\sqrt{\zeta^2-1}\cdot t} + Be^{-\sqrt{\zeta^2-1}\cdot t}\right) \quad (1.28)$$

Where the constants *A & B* can be evaluated subject to initial conditions *x(0)* and $\dot{x}(0)$.

This same concept can be extended to multiple bodies tied together by a series of springs and dampers, as shown in Figure 1.4. As the number of point mases grows, they get closer to a real body, which is what a Finite Element Model (FEM) represents.

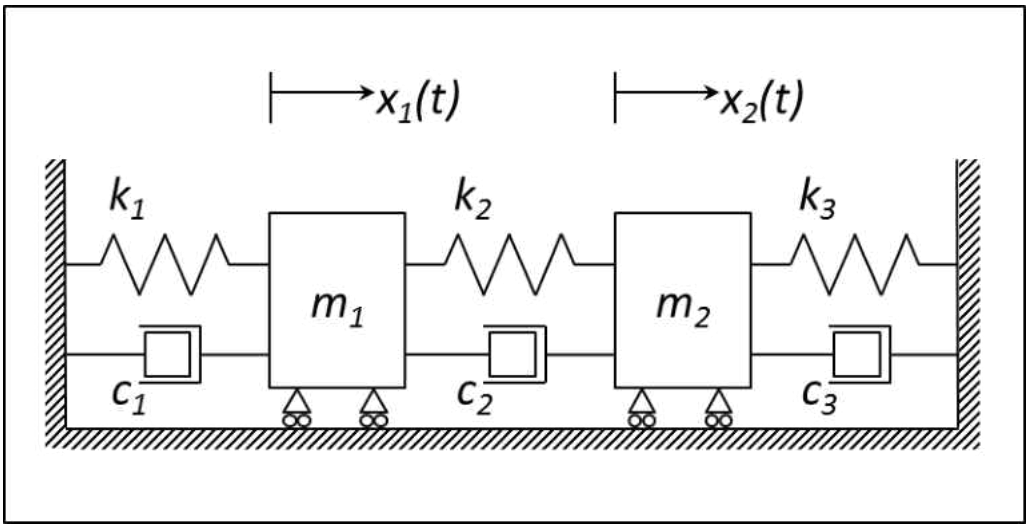

Figure 1.4: Multiple DOF Oscillators

Applying a force balance again will now yield two equations:

$$m_1\ddot{x}_1 + (c_1 + c_2)\dot{x}_1 - c_2\dot{x}_2 + (k_1 + k_2)x_1 - k_2x_2 = 0$$

$$m_2\ddot{x}_2 - c_2\dot{x}_1 + (c_2 + c_3)\dot{x}_2 - k_2x_1 + (k_2 + k_3)x_2 = 0 \qquad (1.29)$$

This can be written in matrix form:

$$\begin{bmatrix} m_1 & 0 \\ 0 & m_2 \end{bmatrix}\begin{bmatrix} \ddot{x}_1 \\ \ddot{x}_2 \end{bmatrix} + \begin{bmatrix} c_1 + c_2 & -c_2 \\ -c_2 & c_2 + c_3 \end{bmatrix}\begin{bmatrix} \dot{x}_1 \\ \dot{x}_2 \end{bmatrix} +$$

$$\begin{bmatrix} k_1 + k_2 & -k_2 \\ -k_2 & k_2 + k_3 \end{bmatrix}\begin{bmatrix} x_1 \\ x_2 \end{bmatrix} = \begin{bmatrix} 0 \\ 0 \end{bmatrix} \qquad (1.30)$$

In general, a large number of bodies/equations can be written in matrix form, and solved by the FEM

$$\mathbb{M}\ddot{x} + \mathbb{C}\dot{x} + \mathbb{K}x = 0 \qquad (1.31)$$

Once an FEM solution provides the vibratory response of an airfoil (Eigen vectors), the blade deflections (in 3 dimensions) can be classified according to the main direction of deformation; these are called the fundamental mode shapes. For example deforming in the circumferential direction (bending or flexural modes), or twisting about a span-wise axis (torsional). Figure 1.5 shows a schematic of some of the more common fundamental modes. For a stand-alone blade, each of these modes will occur at different frequencies, and that frequency is a function of the blade shape, material, operating conditions, etc. Although the order in which the modes appear may vary, the simpler deflections (i.e. first bending) tend to appear first (lower frequencies), while the more complex shapes (chord-wise second bending – not shown) tend to occur at higher frequencies. The really intricate shapes (combinations of more than one fundamental shape) can occur at very high frequencies and require more energy to excite. Their prediction is less accurate and not typically considered in a standard design process.

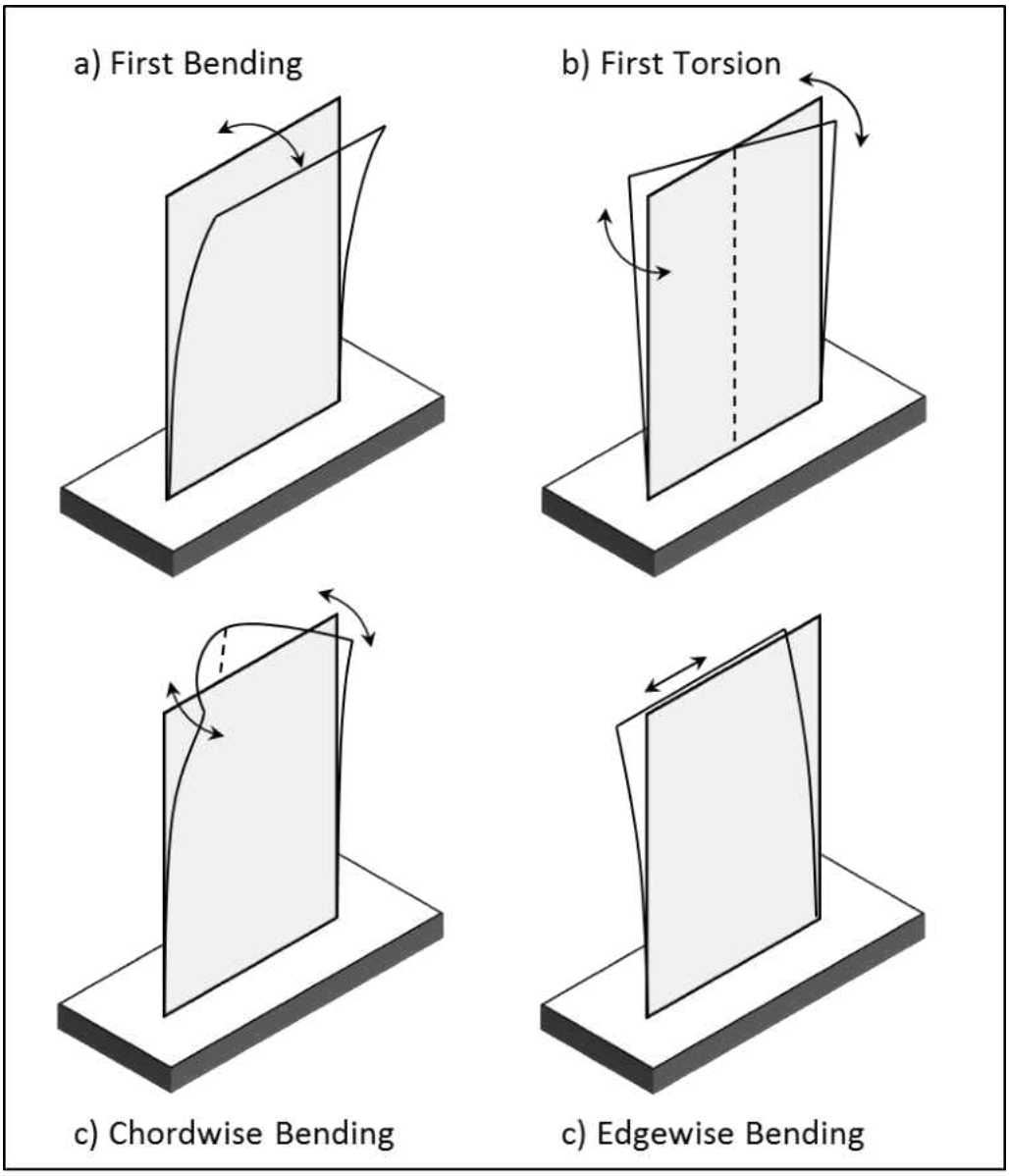

Figure 1.5: Fundamental Airfoil Mode Shapes

A final concept considered here regarding structural dynamics, is that of Nodal Diameters (ND). Just like the airfoils can be categorized by their deflections, the disks holding these airfoils also undergo distinctive vibratory displacements. For circular

membranes (i.e. the disks), the vibrations are such that lines of zero deflection are formed along the radial, circumferential and/or axial directions. However, in gas turbine disk applications, the nodal diameters (zero displacement lines along the radial direction) are the most common; some examples are shown in Figure 1.6.

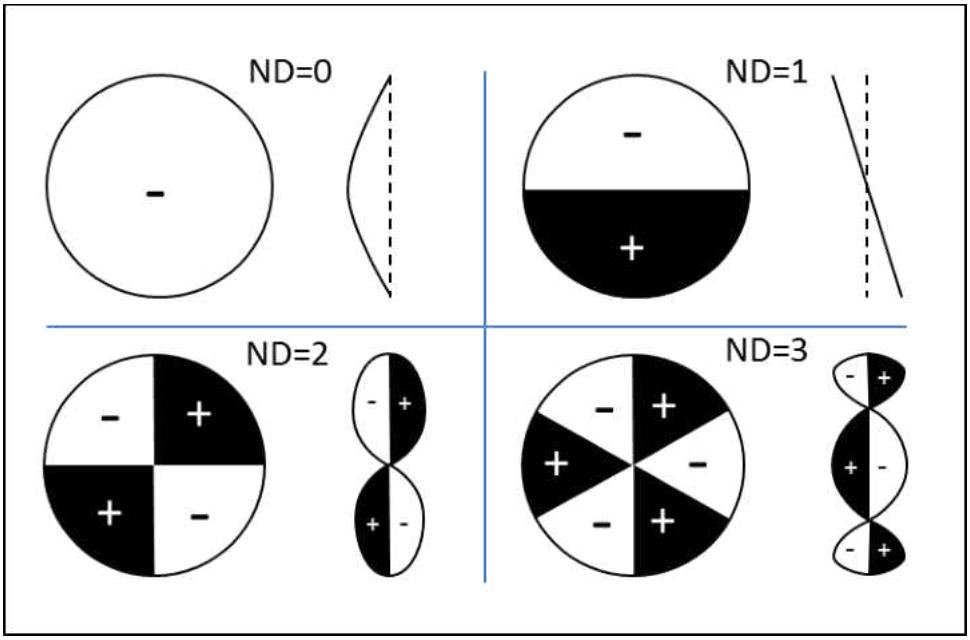

Figure 1.6: Disk Nodal Diameters

The figure only shows ND=0, 1, 2, and 3, but they can go up to:

$$ND_{max} = \frac{Num.\ of\ Blades}{2} \quad \rightarrow \quad even\ Num.\ of\ Blades \qquad (1.32)$$

$$ND_{max} = \frac{Num.\ of\ Blades - 1}{2} \quad \rightarrow \quad odd\ Num.\ of\ Blades \qquad (1.33)$$

As with blades, the frequency of each of these distinctive displacements increases with the complexity of the shape. Since disks and blades display different vibratory displacement characteristics, a bladed disk is expected to exhibit some combination of the two. For disks that are relatively stiff, the blade frequency will be relatively independent of the disk nodal diameter; this is the case for most axial compressor applications. However, for relatively flexible disks, there is a lot more interaction. It turns out that for a particular blade mode shape, the frequency can increase as the number of nodal diameters increases. This is the case for turbine bladed disks (specially shrouded blades), and is depicted in Figure 1.7.

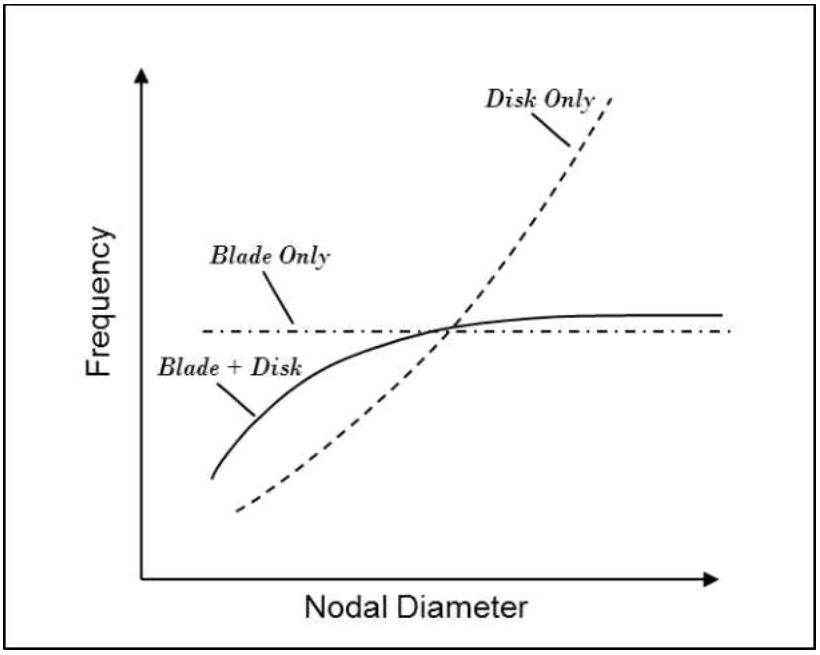

Figure 1.7: Bladed Disk Frequency Interference

1.5 Aeroelasticity

The field of aeroelasticity deals with the interactions between the aerodynamic, elastic and inertial forces between a fluid and the object it surrounds. These interactions are often depicted by Collar's triangle, which can be complemented by a Venn diagram as shown in Figure 1.8.

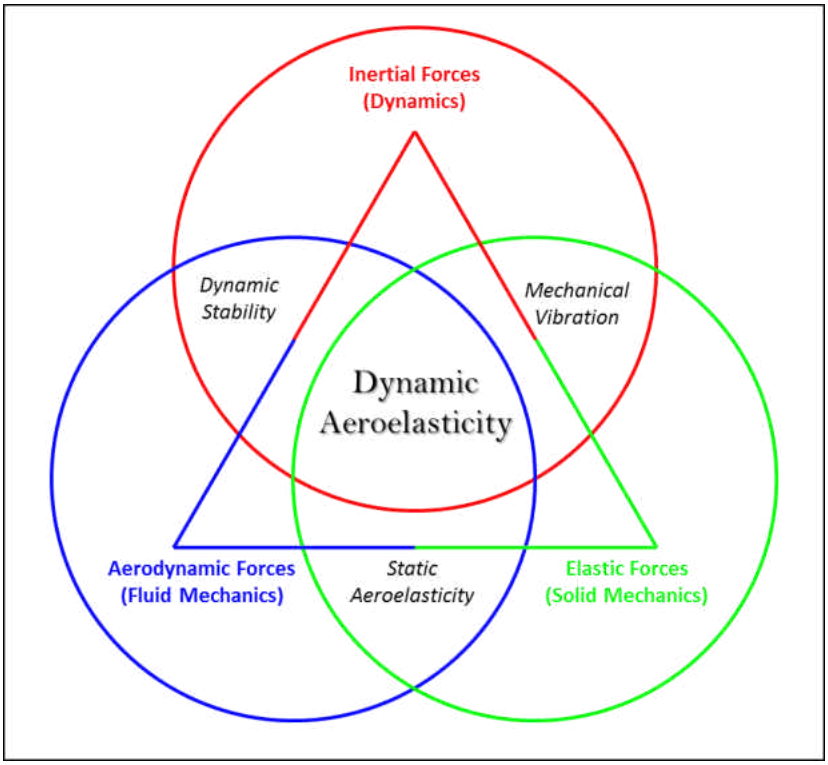

Figure 1.8: Collar's Triangle

Traditionally, static and dynamic aeroelasticity have taken the spotlight. However, modern considerations that take into account high temperature environments give rise to the term "Aero-Thermo-Elasticity". Similarly, applications that take into account

guidance and control systems are termed “Aero-Servo-Elasticity”. Initially constrained to aircraft design, the field now encompasses applications in civil engineering, turbomachinery, flexible pipes and nuclear engineering. Today there are many great resources that deal with the subject; two that stand out are Bisplinghoff [67] and Dowell [68].

1.5.1 Historical Perspective

According to Weisshaar [69], the term aeroelasticity was first coined by two English engineers, Alfred Pugsley and Harold Roxbee Cox, working for the Royal Aircraft Establishment in the early 1930’s. Today, the term aeromechanics is used interchangeably and encompasses not just aircraft, as it did originally, but also rotor machinery, as well as stationary structures and even objects submerged in liquids. The initial development of this field closely followed the development of aircraft during the early part of the 20th century. However, as Garrick [70] pointed out, this development was mostly reactionary to field issues uncovered as aircraft design evolved. As such, most of the theories on the subject have been developed for the phenomenon as it applies to aircraft wings. However, the concerns addressed by aeromechanics are equally present and detrimental in the internal flows encountered by gas turbines.

One of the first well known aircraft fiascos, due to what today has been classified as an aeroelastic failure, was the Langley Aerodrome’s second crash in December 8, 1903; a mere 9 days earlier than the Wright brothers’ historic first manned flight. Today

it is thought that the collapse, shown in Figure 1.9, was due to what is currently described as wing torsional divergence.

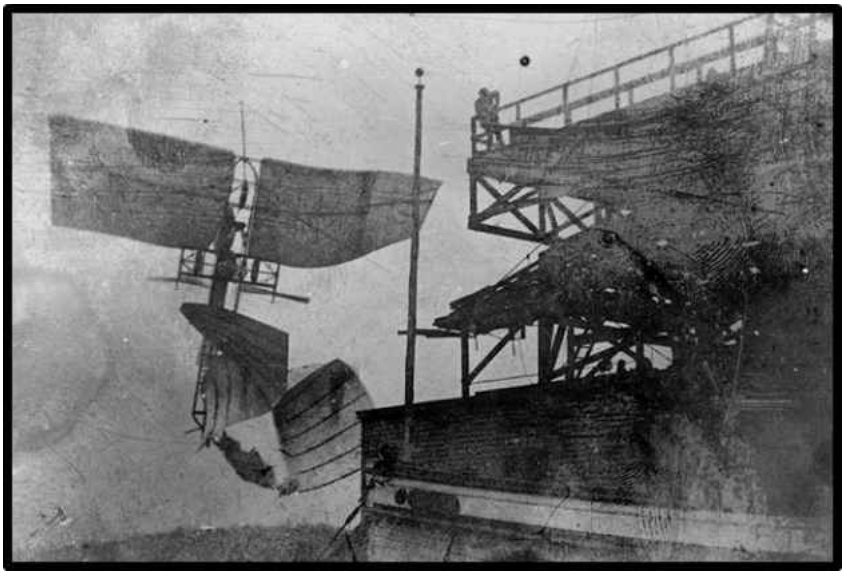

Source: Smithsonian Institute Research Information System. http://www.siris.si.edu/

Figure 1.9: Langley's Aerodrome Second Crash. December 8, 1903

Perhaps a better known example of an aeroelastic fiasco is the Tacoma Narrows Bridge. It was inaugurated on July 1, 1940, and collapsed 4 months later on November 7. There had been some disagreement/confusion on the exact cause of the failure in the first ~50 years since the event, but today it has been attributed to a "single degree of freedom torsional flutter" by Bilah [71]. Figure 1.10 shows snapshots from different views that captured the spectacular motion and ultimate collapse of the bridge.

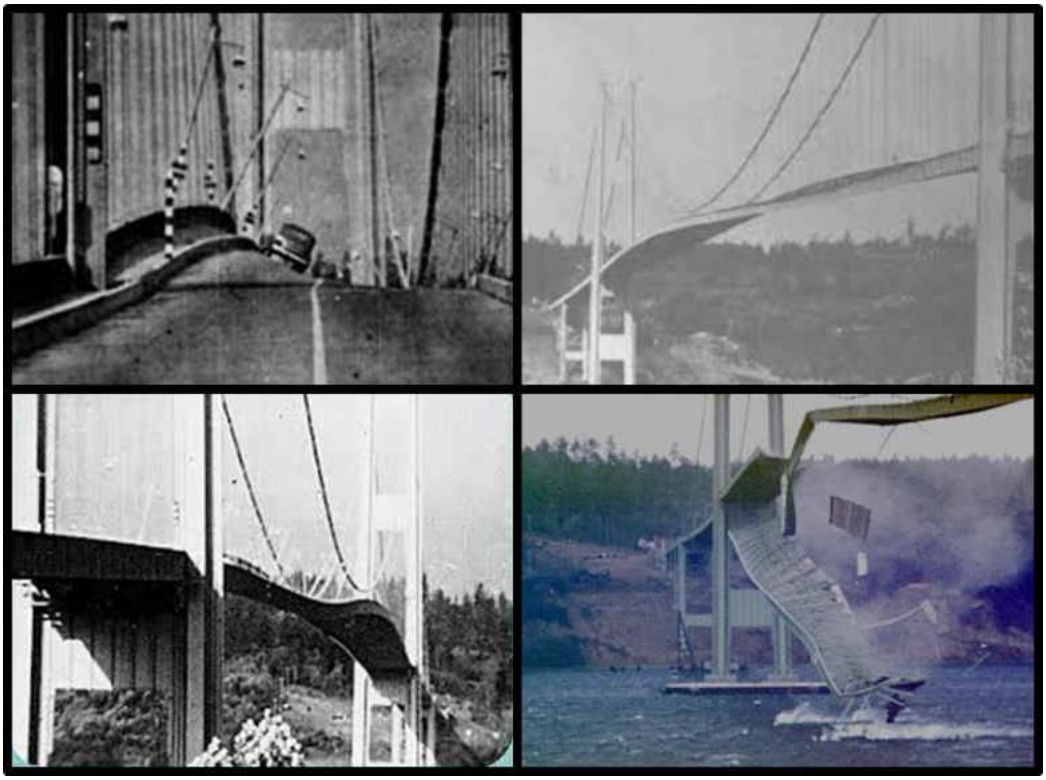

Source: Lectures on Physics. http://www.vias.org/physics/copyright.html

Figure 1.10: Tacoma Narrows Bridge Collapse

1.5.2 Flutter

Since the topic of this project is restricted to turbomachinery, focus will be given to the two main aeroelastic concerns in gas turbines: flutter and forced response. Beginning with flutter, the term first appeared in 1924 in a paper by R.T. Glazebrook "Yearbook of the British Aeronautical Committee", according to Weisshaar [69]. Flutter is a self-excited oscillatory instability where the vibratory motion of the airfoil produces an unsteady aerodynamic load. This load feeds energy back into the airfoil, hence

amplifying the vibration further. This feedback loop can eventually cause a high cycle fatigue (HCF) failure of the blade, and potentially the whole engine.

Long slender airfoils are more susceptible to flutter than small sturdy ones; hence flutter has been a bigger problem for axial compressors versus radial ones. It generally occurs at frequencies that are not integral multiples of engine orders, which categorizes it as a non-synchronous vibration (NSV). It actually occurs at the natural frequency of the airfoil, although this can be complicated by different modes blending into one, or by mistuning effects. Specific to turbomachinery, there are different types of flutter. Although there is some ambiguity regarding how flutter is categorized, there are several regions on a compressor map that exhibit different mechanism that induce flutter, these are shown in Figure 1.11. A concise description of each of these regions is given by Cumpsty [18].

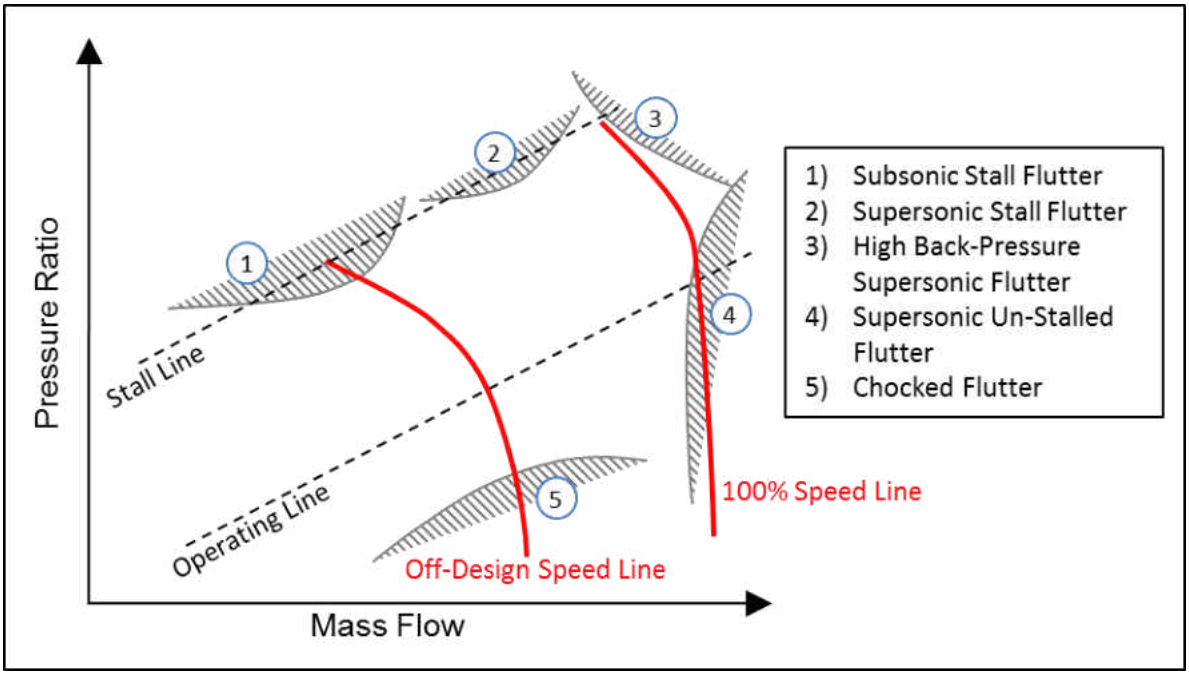

Source: Reproduced after Mikolajczak, 1975 [64] and Cumpsty [18]

Figure 1.11: Compressor Map: Flutter Regions

1.5.3 Forced Response

In forced response, the unsteady aerodynamic load is not produced by the airfoil vibration. Instead, it comes from external sources such as acoustic waves (from upstream or downstream potential flow fields), and/or entropic or vortical disturbances (from upstream viscous layers or wakes), Platzer [16]; this is depicted in Figure 1.12.

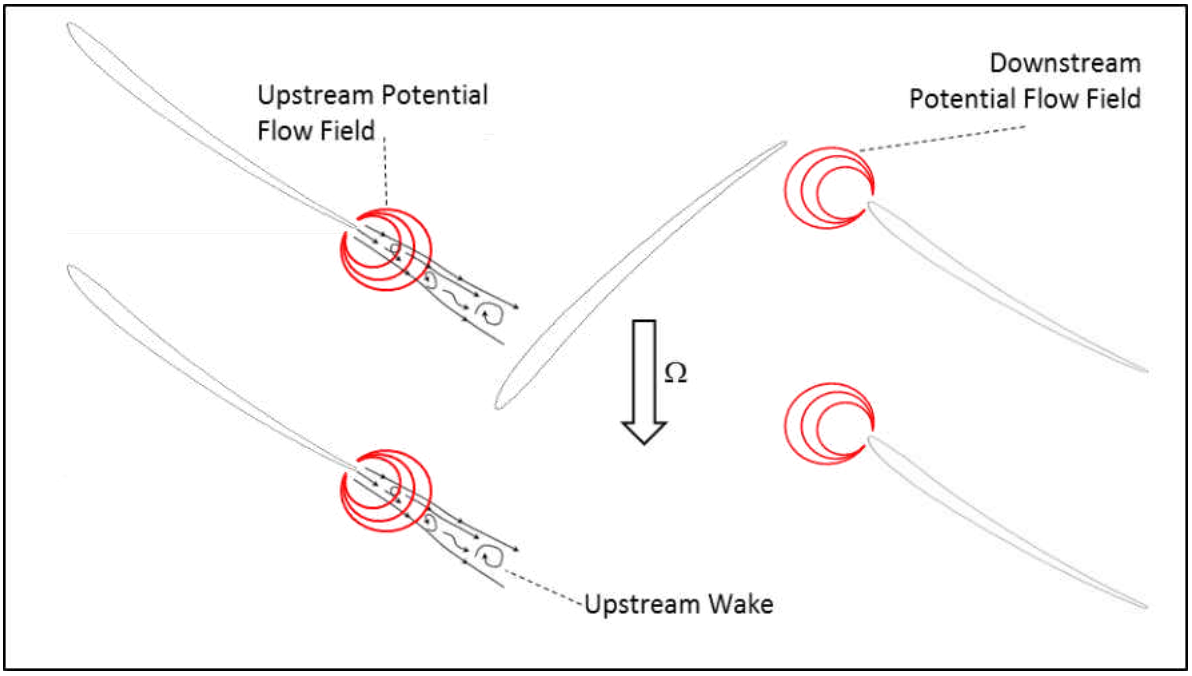

Figure 1.12: Forced Response Drivers

If this aerodynamic load is periodic in time, with a frequency that coincides with one of the Eigen frequencies of the airfoil, it will feed energy into the system causing it to vibrate violently.

In order to ascertain whether an unsteady disturbance will coincide with one of these vibration modes, a Campbell diagram is typically employed, Figure 1.13.

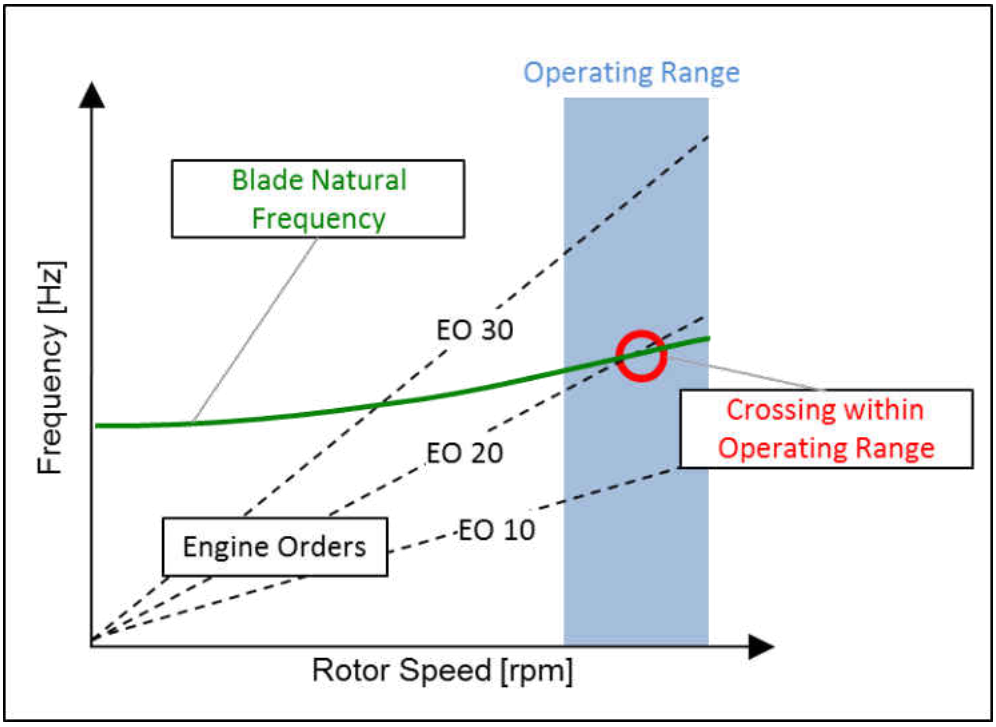

Figure 1.13: Campbell Diagram

The diagram places the airfoil's natural frequency in the ordinate, plotted against the rotational speed in the abscissa. Disturbances that occur at harmonics of the rotor speed are shown by the Engine Order lines (EO). As an example, if there is a disturbance that occurs 20 times per rotation, it is depicted by the EO 20 line. Such disturbances typically come from one of the adjacent row's airfoil count, but integer differences of airfoil counts, or counts from rows further away can also become a disturbance. If a disturbance coincides with one of the natural frequencies of the airfoil (solid line) within the operating range of the engine, then the crossing could represent a problem. Other effects that will determine whether this crossing will result in damage to

the blade are: the mechanical damping of the blade/disk assembly (typically low), the material capability, operating speed, magnitude of the disturbance, etc. In practice, the fundamental modes of a blade are designed to avoid crossings with certain harmonics (low EO drivers, adjacent row airfoil counts, etc.), but it is impossible to design (or tune) airfoils away from all drivers.

Another complicating factor is the concept of mistuning. The term refers to the frequency differences that exist amongst airfoils of the same row. Analytically, all airfoils in a row are typically designed to have the same Eigen frequencies. However, in reality differences arise from manufacturing tolerances and/or other unavoidable variations from blade to blade. For forced response, mistuning aggravates the problem because when a crossing occurs, the energy does not get distributed equally amongst all blades, but could potentially become concentrated in just a few. In the case of flutter, mistuning can be useful because differences between blades can add damping to the system, Cumpsty [18].

1.5.4 Work per Cycle

The way in which the flow unsteadiness interacts with the airfoil vibration, in either flutter or forced response, can be quantified by the work per cycle. Conceptually, this is a simple calculation of the work generated by the unsteady pressure ($\widetilde{\boldsymbol{P}}$) forces acting on the surface of the airfoil, which is moving at the velocity given by the frequency of vibration ($\widetilde{\vec{\boldsymbol{V}}}$); this is shown in Figure 1.14.

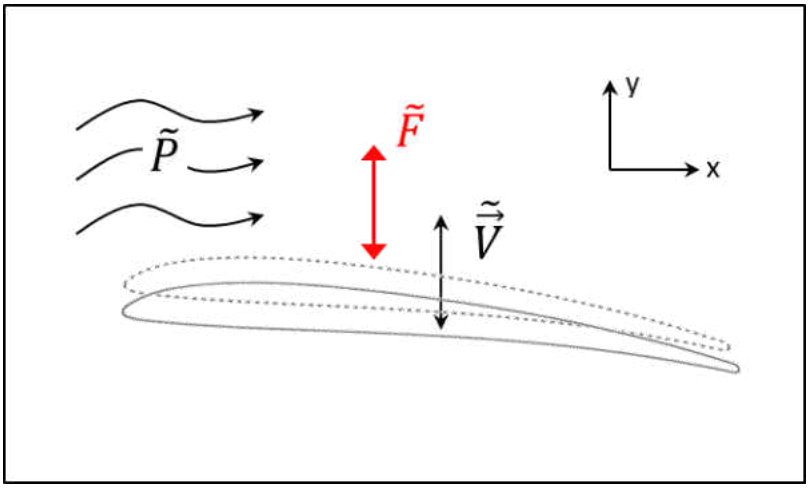

Figure 1.14: Work per Cycle Schematic

When the pressure perturbation pushes down on the surface (force acting in the –y direction) at the same time that the airfoil moves upward (+y), energy is removed from the airfoil; this is considered positive aerodynamic damping. Inversely, when both the pressure force and the airfoil displacement act in the same direction, energy is added to the airfoil from the air; this is negative aerodynamic damping. If the amount of mechanical damping present in the system (from material properties, mechanical attachment, etc.) is not sufficient to absorb the added energy during negative damping, the amplitude of vibration increases. As more and more energy is successively added to the blade on each oscillation cycle, it can lead to failure. The effects can range from mild to catastrophic depending on the actual mode of vibration. For example for a vibratory mode where only the airfoil trailing edge tip is participating, a small piece of the airfoil may break off, hence self-correcting the vibratory excitation. Of course if the

active mode is one where the entire airfoil participates (such as a first bending mode), and a large portion of metal breaks-off, it can cause severe damage to adjacent rows and/or the entire engine. Figure 1.15 shows examples of these two scenarios.

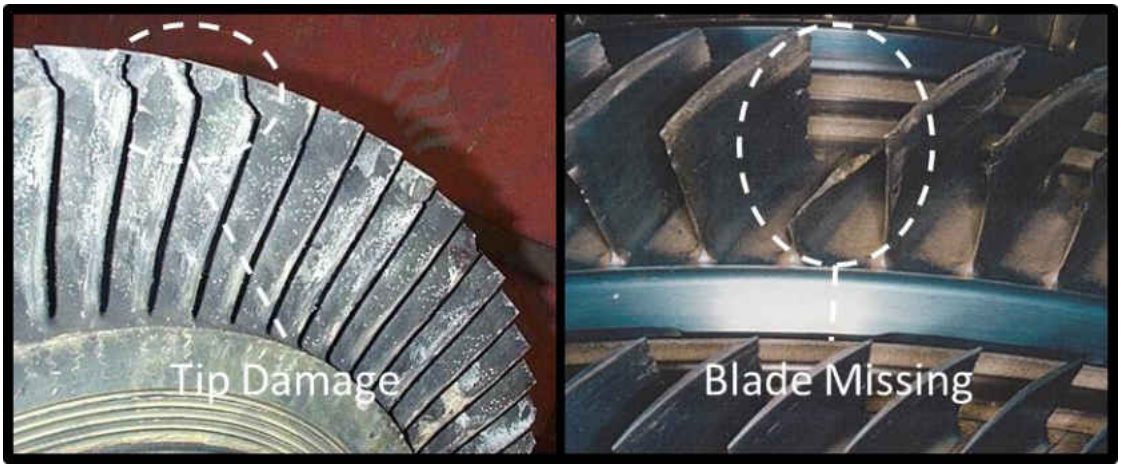

Source: www.marineturbo.co.uk and articles.sae.org

Figure 1.15: Airfoil Damage

The actual calculation of the work per cycle is performed, as the name suggests, for one cycle of vibration, and integrated over the entire airfoil surface. This is expressed by Equation (1.34); see Kielb [72] and Platzer [16]. The integral seems simple enough from a cursory look. However, since the perturbation pressure and velocity are expressed in complex form, the details take a little more effort.

$$W_{Cyc} = \int_0^T \left[\int_A -\dot{\Phi}\, P\, dA \right] dt \tag{1.34}$$

Here $\dot{\Phi}$ is the vibratory velocity of the airfoil (node displacements). Now, using the following definitions:

$$\Phi = Re\left(\Phi e^{-i\omega t}\right) = \frac{1}{2}\left(\Phi e^{-i\omega t} + \bar{\Phi} e^{i\omega t}\right) \quad (1.35)$$

$$\dot{\Phi} = \frac{1}{2}\left(-i\omega\Phi e^{-i\omega t} + i\omega\bar{\Phi} e^{i\omega t}\right) = \frac{i\omega}{4}\left(-\Phi e^{-i\omega t} + \bar{\Phi} e^{i\omega t}\right) \quad (1.36)$$

$$P = Re\left(p e^{-i\omega t}\right) = \frac{1}{2}\left(p e^{-i\omega t} + \bar{p} e^{i\omega t}\right) \quad (1.37)$$

The bar superscript ($^{-}$) refers to the complex conjugate

$$p = p_r + ip_i \quad , \quad \bar{p} = p_r - ip_i \quad (1.38)$$

Plugging these into Equation (1.34)

$$W_{Cyc} = \int_A \left[\int_0^T -\frac{i\omega}{4}\left(-\Phi e^{-i\omega t} + \bar{\Phi} e^{i\omega t}\right)\left(p e^{-i\omega t} + \bar{p} e^{i\omega t}\right) dt\right] dA \quad (1.39)$$

$$\left(-\Phi e^{-i\omega t} + \bar{\Phi} e^{i\omega t}\right)\left(p e^{-i\omega t} + \bar{p} e^{i\omega t}\right)$$

$$= -\Phi\bar{p} + \bar{\Phi}p - \Phi p e^{-2i\omega t} + \bar{\Phi}\bar{p} e^{2i\omega t} \quad (1.40)$$

$$W_{Cyc} = \int_A \left[\int_0^T -\frac{i\omega}{4}\left(-\Phi\bar{p} + \bar{\Phi}p - \Phi p e^{-2i\omega t} + \bar{\Phi}\bar{p} e^{2i\omega t}\right) dt\right] dA \quad (1.41)$$

The integration of the last two terms evaluates to zero

$$\int_0^T \left(-\Phi \mathrm{p} e^{-2i\omega t} + \bar{\Phi}\bar{\mathrm{p}} e^{2i\omega t}\right) dt = -\frac{\Phi \mathrm{p}}{2i\omega} e^{-2i\omega t}\Big|_0^T + \frac{\bar{\Phi}\bar{\mathrm{p}}}{2i\omega} e^{2i\omega t}\Big|_0^T$$

$$= -\frac{\Phi \mathrm{p}}{2i\omega}(e^{-2i\omega T} - e^0) + \frac{\bar{\Phi}\bar{\mathrm{p}}}{2i\omega}(e^{2i\omega T} - e^0) \quad (1.42)$$

Since the frequency can be expressed in terms of the period for one cycle:

$$\omega = \frac{2\pi}{T} \quad (1.43)$$

$$-\frac{\Phi \mathrm{p}}{2i\omega}(e^{-4i\pi} - 1) + \frac{\bar{\Phi}\bar{\mathrm{p}}}{2i\omega}(e^{4i\pi} - 1) =$$

$$-\frac{\Phi \mathrm{p}}{2i\omega}(\cos(4\pi) - i\sin(4\pi) - 1) + \frac{\bar{\Phi}\bar{\mathrm{p}}}{2i\omega}(\cos(4\pi) + i\sin(4\pi) - 1) = 0 \quad (1.44)$$

To evaluate the first two terms in Equation (1.44), the cosine and sine terms for a backward traveling wave were employed.

$$W_{Cyc} = \int_A \left[\int_0^T -\frac{i\omega}{4}(-\Phi\bar{\mathrm{p}} + \bar{\Phi}p)\, dt\right] dA \quad (1.45)$$

$$\Phi = \Phi_c + i\Phi_s \quad , \quad \bar{\Phi} = \Phi_c - i\Phi_s \quad (1.46)$$

$$\mathrm{p} = \mathrm{p}_r + i\mathrm{p}_i \quad , \quad \bar{\mathrm{p}} = \mathrm{p}_r - i\mathrm{p}_i \quad (1.47)$$

Plugging these into Equation (1.45) and working out the algebra:

$$(-\Phi\bar{\mathrm{p}} + \bar{\Phi}p) = -(\Phi_c + i\Phi_s)(\mathrm{p}_r - i\mathrm{p}_i) + (\Phi_c - i\Phi_s)(\mathrm{p}_r + i\mathrm{p}_i)$$

$$= 2i\Phi_c \mathrm{p}_i - 2i\Phi_s \mathrm{p}_r \quad (1.48)$$

$$\int_0^T -\frac{i\omega}{4}(2i\Phi_c \mathrm{p}_i - 2i\Phi_s \mathrm{p}_r)\, dt = \frac{\omega \mathrm{t}\Phi_c \mathrm{p}_i}{2}\Big|_0^T - \frac{\omega \mathrm{t}\Phi_s \mathrm{p}_r}{2}\Big|_0^T$$

$$= \pi(\Phi_c \mathrm{p}_i - \Phi_s \mathrm{p}_r) \quad (1.49)$$

$$W_{Cyc} = \pi \int_A (\Phi_c \mathrm{p}_i - \Phi_s \mathrm{p}_r)\, dA \quad (1.50)$$

The pressure terms can also be expressed in terms of the cosine and sine components:

$$\mathrm{p} = \mathrm{p}_{cr} + i\mathrm{p}_{ci} + i(\mathrm{p}_{sr} + i\mathrm{p}_{si}) \quad (1.51)$$

$$\mathrm{p}_r = \mathrm{p}_{cr} - \mathrm{p}_{si} \quad , \quad \mathrm{p}_i = \mathrm{p}_{ci} + \mathrm{p}_{sr} \quad (1.52)$$

$$W_{Cyc} = \pi \int_A (\Phi_c(\mathrm{p}_{ci} + \mathrm{p}_{sr}) - \Phi_s(\mathrm{p}_{cr} - \mathrm{p}_{si}))\, dA \quad (1.53)$$

Finally, the work per cycle can be broken down into the main contributors

$$W_{Cyc} = \pi \int_A \Phi_c \mathrm{p}_{ci} dA + \pi \int_A \Phi_c \mathrm{p}_{sr} dA$$

$$-\pi \int_A \Phi_s \mathrm{p}_{cr} dA + \pi \int_A \Phi_s \mathrm{p}_{si} dA \quad (1.54)$$

$$W_{Cyc} = W_{cc} + W_{cs} - W_{sc} + W_{ss} \quad (1.55)$$

The work per cycle is the final product of an aeroelastic analysis. Unfortunately, since it is calculated using airfoil modal displacements, it is bounded by the same restrictions. In an FEM vibratory solution, the actual displacements are arbitrary. They can be very large, or very small, or can be normalized to 1.0. So the actual displacement values are not useful for calculating stresses. Usually, strain gage data (or other forms of test data) is used to turn the relative displacements to more physically meaningful numbers. Hence, the work calculated from those displacements is only useful on a relative basis, unless anchored by test data. For example if the actual displacements are known from strain gage and/or tip timing measurements, then the work per cycle can be scaled accordingly. Lastly, in flutter analyses, an aerodynamic damping is obtained by normalizing the work per cycle by the kinetic energy (KE) of the vibration.

$$\xi = \frac{W_{Cyc}}{2KE} = \frac{W_{Cyc}}{2\left(\frac{1}{2}M\omega^2\right)} \qquad (1.56)$$

Where M is the modal mass and ω is the frequency of vibration.

As mentioned earlier, negative aerodynamic damping corresponds to energy added from the air into the airfoil, and is a condition to be avoided.

CHAPTER 2: LITERATURE REVIEW

Research on gas turbine tip clearances has been a subject of investigation over the last six decades, with some of the earliest research dating back to the 1950's and 60's; including the Parallel Compressor Theory from the late 60's, Reid [74]. Even further back, aeroelastic phenomena (flutter / forced response) has been observed since the early days of aviation, as was discussed in section 1.5.1. For both of these, early papers were mainly a combination of experimental and analytical research on reduced order models. Today, numerical simulations are much more prevalent due to advancements in computer science, and much research is dedicated to the development of numerical methods.

In this chapter, a review of the literature is presented for different aspects of tip clearance flows, followed by forced response/flutter investigations; finally some observations on the latest numerical modeling techniques are discussed.

2.1 Tip Flow Injection

The injection of air (typically cooling) is a common way to alter an undesired flow characteristic in gas turbines. Specifically to clearances, tip flow injection refers to the addition of flow around the tip clearance in order to alleviate some of the unfavorable consequences of the flow in this region.

Tip flow injection is usually considered a type of end-wall treatment, but here it is considered as a separate tactic because the mechanism utilized is not the modification

of the casing wall. However, it does require a physical change to this wall at discrete locations where the flow is injected, as can be seen in Figure 2.1.

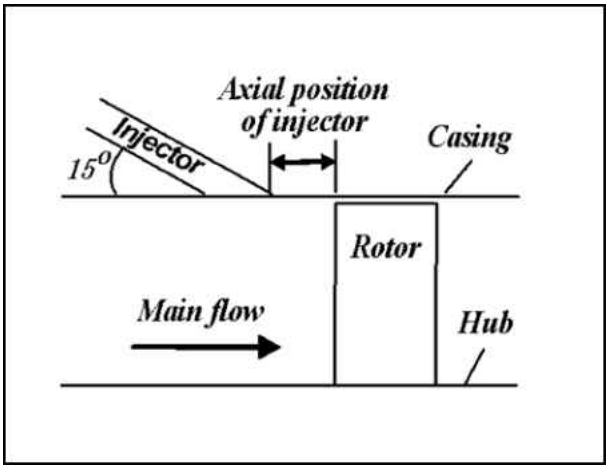

Source: Geng, [23]

Figure 2.1: Tip Flow Injection

This is a relatively newer area of research that has not made it into the mainstream design process. As the name suggests, the idea is to add flow at the OD wall in front of the rotor leading edge, in order to influence/control the tip leakage flow. Dobrzynski [20], Frechette [21] and Jothiprasad [22] demonstrated that this helps to extend the stall margin of a rotor, with the consensus being that larger flows are generally better. The benefit comes by keeping the tip leakage flow moving axially, rather than perpendicular to the flow, Geng [23]. This is one of the criteria for the onset of stall, Vo [24], which in turn can lead to flutter. There is also an unloading of the blade tip, which can be

quantified by a reduction of the loading parameter. Flow injection also helps to reduce the tip leakage unsteadiness, which is helpful since Ha [25] and Milach [8] have shown that the tip leakage vortex oscillations increase as the compressor operation approaches stall.

However, Bae [26] has pointed out that the gains in stall margin do not necessarily outweigh the power spent to generate the injection; this could actually result in a net loss in efficiency. Another drawback of tip injection is that at the rotor exit there is an introduction of non-axisymmetric flow conditions. These can disrupt the downstream stator's inlet boundary conditions, hence generating aerodynamic losses, Dobrzynski [20]. One proposed solution to the first concern is the recirculation of flow, so that the penalty for injection can be reduced. This consists of extracting flow from over the tip region, and re-injecting it upstream of the leading edge, as shown by Weichert [27] in Figure 2.2.

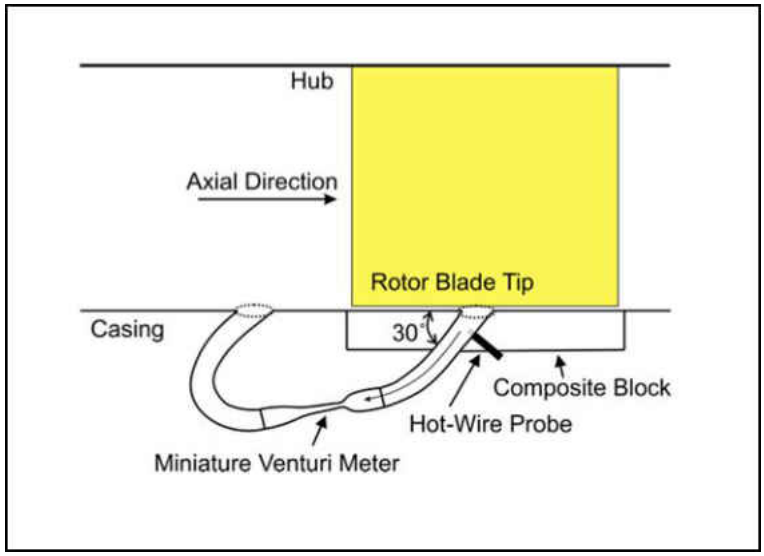

Source: Weichert [27]

Figure 2.2: Flow Injection Recirculation

The set up contains a loop that self regulates the amount of air being re-injected, with a minimum at design point and a maximum at off-design. The reported improvement of 2% was obtained without the typically accompanying loss of design point efficiency.

2.2 Tip Clearance Size

A large number of papers have focused on the aerodynamic impact/influence of a prescribed constant tip gap on the main flow. In contrast, the papers discussed in this section consist of trade studies on the size of the radial clearance, by varying the height

of the blade. However, the same gap variant is applied to all the blades in the row, so the different gaps are constant for the entire wheel.

Earlier cascade tests found that larger clearance values generated more losses, Doukelis [28], as well as an increase in the region of influence, Juan [2]. Consequently, decreasing the gap can reduce the blockage generated by the clearance flows, Sakulkaew [29]. Another finding by Zhang [1], important for unsteady considerations, is that larger gaps increase the fluctuations of the tip clearance vortex. Other investigators, Mailach [8], Hah [25] and Sakulkaew [29], have also found this to be one of the significant factors leading to reduced stall margins. Furthermore, an increased gap augments the unsteadiness of the oscillating tip clearance flow in terms of both amplitude and frequency. Du [2] found that as the gap increases, this oscillation shifts from the PS of the leading edge (LE) to where the shock interacts with the clearance flow (in transonic compressors).

Although the consensus of most of the literature is that smaller gaps are generally better aerodynamically, Sakulkaew [29] found that there is actually an optimum value of gap size, not necessarily at the minimum clearance value. As the gap is reduced, the tip vortex losses are also reduced. However, as the gap goes toward zero, secondary losses similar to those in a shrouded vane begin to increase. This causes the total losses in the tip region to increase again. At off-design conditions (reduced rotor speeds), the optimum value for the tip gap is smaller since the blades have higher loading and increased losses. Conversely, for increased rotor speeds the optimum value is larger.

Another kind of gap size is obtained by varying the clearance in the axial direction, as shown in Figure 2.3 (c). For this scenario, the clearance was increased as the axial coordinate increased. This resulted in better efficiency under the same conditions as a flat clearance, Abdel [76]. Similar observations were obtained by Wang [30] and Mohan [31]. They reasoned that the increased gap allowed more interaction of the leakage flow with the secondary flow vortices, the casing boundary layer and the vortex flow, which are more pronounced in the aft portion of the blade

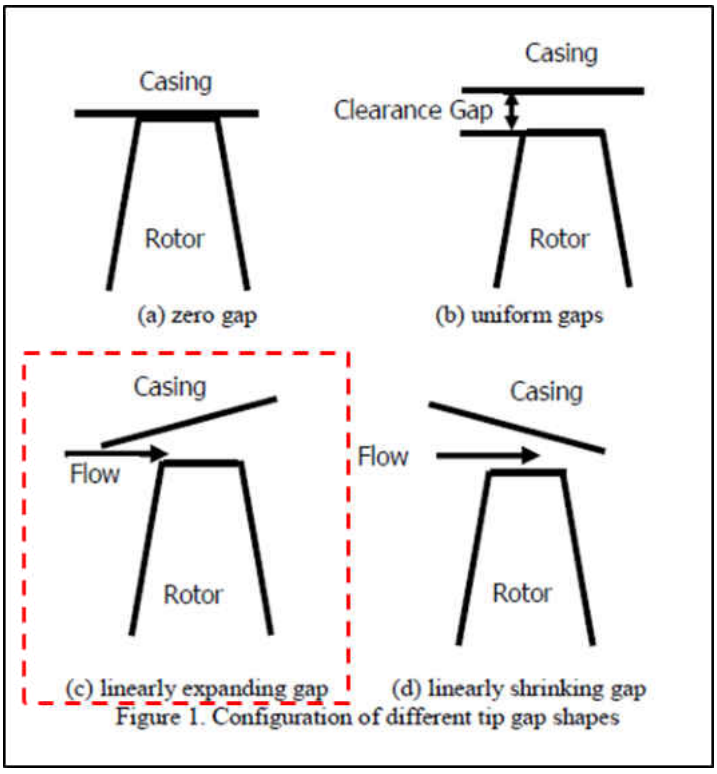

Source: Abdel [76]

Figure 2.3: Axially Varying Gap

A final type of clearance configuration that was shown to have some benefit is a stepped gap machined on the blade in the circumferential direction, as shown in Figure 2 4. This is a concept similar to what is also known as a squealer tip, but larger and with a different motivation. Instead of providing blade material that can wear down if rubbing occurs, the intent here is to reduce the blockage produced by the leakage flow. Ma [32] described the mechanism at play as a weakening of the tangential migration of the low momentum flow, again resulting in a benefit relative to a flat tip.

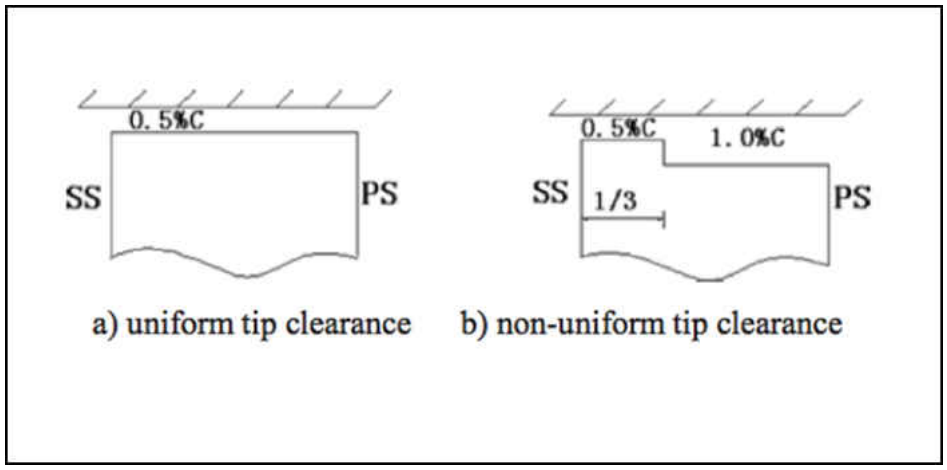

Source: Ma [32]

Figure 2.4: Tangential Tip Step

2.3 End-Wall Treatments

This segment of the literature deals with any modification to the flowpath walls. Technically, this includes some of the configurations of tip gaps and flow injection at the

OD wall described above, therefore in this section those modifications will not be discussed further.

The studies in this section refer to modifying the outer and/or inner cylindrical/conical walls enclosing the flowpath. Generally speaking, these walls are smooth axisymmetric surfaces that are only interrupted for cooling air injection/extraction (at the OD or ID), and at the interfaces of the rotating and stationary components (at the ID only). Modifications of the walls may take many forms; the most popular are listed below and summarized in Figure 2.5:

a) End-Wall Contouring: This is the creation of a concave surface at the ID (hub) in the middle of the rotor passage. It is typically applied at the front of the compressor, but beneficial in the turbine as well. It has been demonstrated that this is an effective means of reducing the secondary flow losses near the wall, hence improving performance. Unfortunately, Glen [33] and Praisner [34] observed that modifications at the hub, may also have unintended negative effects on tip leakage flows.

b) Circumferential Grooves: As the name implies, these are channels in the circumferential direction cut into the outer wall. Investigations have shown that for small clearances, the trailing edge flow had a greater impact in the stall process. On the other hand, for larger gaps the leading edge dominated. Consequently, the location and width of the grooves was shown to influence the stall characteristics of the rotor, Xudong [35].

c) Tip Injection: Already discussed in section 2.1.

d) Abradable Walls: This usually consists of a pocket on the OD wall filled with material that can be scraped and/or worn down by the blade. The intent is that as the blade grows thermally and centrifugally it will run into the casing and form the optimum gap at nominal operating conditions. This way, the cold clearances can be reduced, which leads to an improvement in efficiency and a reduction in fuel consumption, according to Nezym [36] and Hajmrie [37]. This is sometimes used as a work-around/fix when the pinch-point in a hot re-start forces an unintended blade incursion into the casing. Instead of replacing any hardware, it is sometimes possible to rebuild it by means of abradable coatings, hence attempting to restore nominal operating performance.
e) Stepped Tip Gaps: Xudong [35] and Lu [38] studied these gaps, which are similar to circumferential grooves, but deeper, axially longer cavities machined into the casing. The intent is to entrap the tip leakage vortices into the casing, hence improving stability and performance.

The different configurations mentioned above are depicted in Figure 2.5.

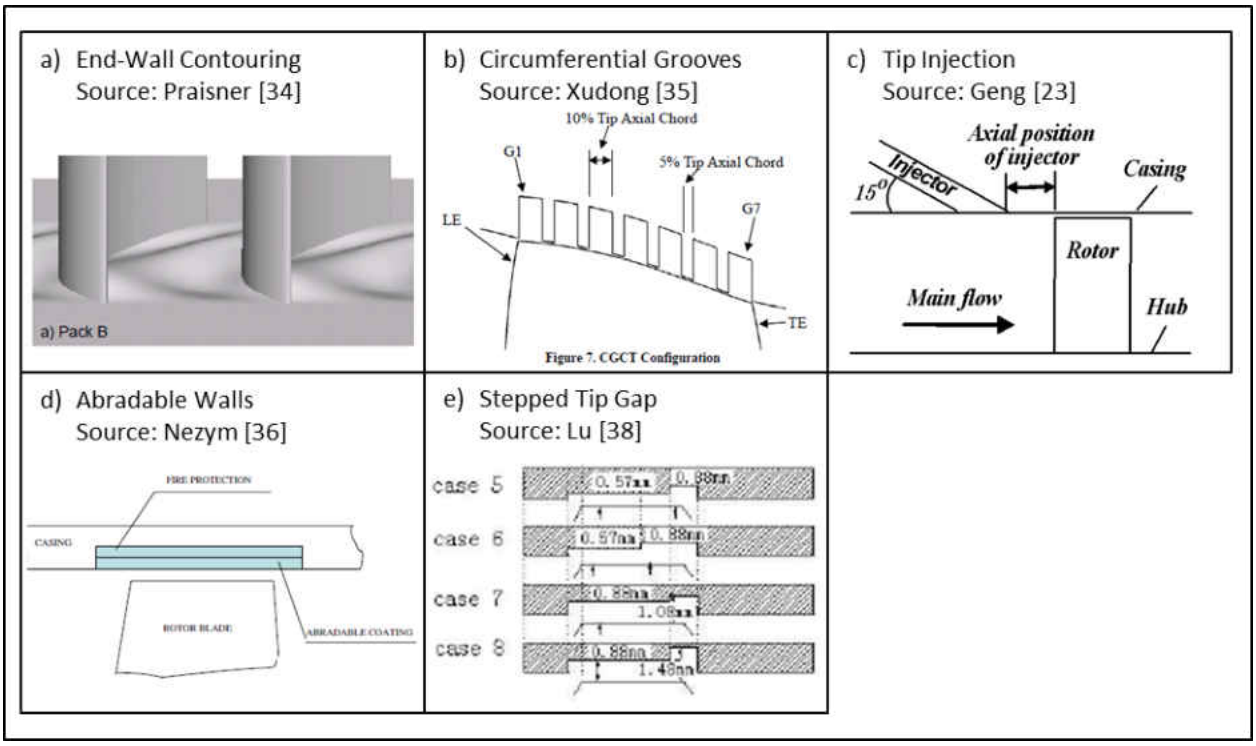

Figure 2.5: Casing Treatments

In general, the intent of these different types of modifications is to improve stability (i.e. stall margin) and/or performance (i.e. efficiency). As such, these studies focused on the aerodynamic impact of the casing modification, and not necessarily on the aeroelastic interactions that the treatment may have on the machine. Unfortunately, the aeromechanical response induced by any of these changes was not part of any these studies. This is a big unknown that could have significant effects considering that most wall treatments produce some sort of asymmetry in the flow field; this could be one of the reasons why they have not become more popular in standard designs. Cost, complexity and net benefit are of course contributing factors as well.

2.4 Non-Axisymmetric Clearances

A more directly applicable sub-category in the tip clearances literature are studies dealing with non-axisymmetric gaps, although there are relatively few papers on the subject. Most research found was experimental, with a few analytical and computational papers.

The direct effect of casing ovalization on the tip clearance flow is that it opens up the gap at some locations (top and bottom), while closing at others (sides). Zhu [39] found that the larger gap regions negatively impact performance, as with uniform gaps. On the other hand, during steady operation, or for time-averaged results, asymmetry was not a major factor on performance, per Cameron [40]. While counter-intuitive at first, this makes sense because when the gap is opened at one clock position, it must be closed at another. So on average, the effects (good and bad) may cancel each other. However, for time accurate models and/or off-design conditions, Kang [9] described a circumferential redistribution of the axial velocities (induced by the varying gaps) that is increased; this was found to have a negative impact on performance.

There have also been fluctuations observed by Morris [41] in the short-length scale disturbances (spike type) near the region of low flow coefficient (low axial velocity), which were dissipated in the regions of high flow coefficient. This spike is commonly associated with rotating stall and has been independently attributed to substantial fluctuations of the tip clearance vortex by Hah [42]. Another important observation by Kang [3] is that these circumferential disturbances were stochastic for a uniform gap, but could be correlated to gap variation in the asymmetric case.

Besides the effect on the rotor passage, a non-uniform gap also influences the downstream pressure going into the vane. At lower flow coefficients, this pressure field had more variation and was not synchronized with the gap variation (flow was less ordered), while the opposite was true for higher flow coefficients (less redistribution and synchronous with gap size). Kang [3] attributed this to the larger axial momentum dominating the circumferential flow redistribution for the higher flow coefficient. This is a significant observation, and indirectly substantiates the findings of Kang [9] and Cameron [40]. At design point (high flow coefficient) the circumferential flow distributions do not get re-distributed (the flow is more ordered). In the circumferential direction, larger gaps have higher losses and smaller gaps have lower losses, so they may get averaged out in terms of performance. At off-design (lower flow coefficient, lower stall margin), the losses from the higher gaps get re-distributed circumferentially, which could generate a problem for performance.

The issue that was not addressed for the asymmetric gap studies found, and the focus of this research, is the aeroelastic impact. If at design point the flow is more ordered and the circumferential variation remains, it also means that there is a greater potential for the wakes to generate a synchronous vibration problem. It is the intent of this project to model and quantify the aeroelastic impact in order to build a predictive capability.

2.5 Aeroelasticity

The phenomena of forced response and flutter have been observed since the early days of aviation, and still a significant concern. Earlier literature dealt with laying out the fundamentals and building correlations based on experimental data. As an example, the work by Wilfred Campbell [43] in 1924 was instrumental in quantifying the vibration problem in turbine disks and in introducing analytical methods, such as the Campbell diagram (discussed earlier), which is still fundamental in the study of aeromechanics today.

Most modern studies consist of some form of order reduction (simplification of the analysis) such as: time linearization, inviscid flow and airfoil count changes, amongst others. Sometimes the order reduction is applied to a new code development. Or in some cases, the simplifications can be applied on an existing code, as done by Custer [44].

Due to the advent of parallelization in CFD and FE analyses, several current studies consist of defining new methodologies of how to integrate the structural and aerodynamic codes. Grids consisting of several million nodes are now considered relatively normal, which would have been considered extremely large 10 years ago (more on that later). The following is a short (by no means comprehensive) list of some of the features that new aeroelastic methodologies include:

a) New code development: Many OEM's (Original Equipment Manufacturer) proprietary CFD codes are now tailored for forced response/flutter, or completely new formulations are developed by universities. Just to name a

few, see Mayorca [45], Vahdati [46], Schmitt [47] and Im [48]. Since aeroelasticity analyses are so intimately tied to test data, it is often desired to keep code development in-house rather than to provide this data to external code developers. Another reason is that for new code development, it is often easier (not always – see Custer [44]) to implement new techniques of formulating the mathematical models, rather than to modify an existing code. For example, the displacement of fluid nodes to accommodate structural movement was combined with a Favre-averaged Navier-Stokes formulation, as discussed by Wu [49].

b) Fully coupled vs. un-coupled fluid-structure interaction: Traditionally, a modal analysis is conducted independent of the aero solution, and then the two combined to extract the unsteady aerodynamic work. However, the underlying assumption is that the aero solution does not change the natural frequency of the blade. In contrast, new fully coupled methods can solve both the aero and modal problems in a conjugate calculation. In some cases the aero mesh is moved at each time step (based on the structural mesh displacement). This allows for the aero damping to be incorporated automatically into the FEM, as presented by Vahdati [46]. Having a de-coupled aero-structural approach may be acceptable given the type of damping. Mayorca [45] pointed out that the importance of a fully coupled approach is mainly seen when the source of damping is mostly

aerodynamic. Also, when non-uniform aerodynamic fluctuations cause changes in the vibratory and structural response of the blade, Zhang [50].

c) Time domain vs. frequency domain: Most CFD solvers currently march the flow equations in time until all residuals fall below a predetermined "convergence" level for steady calculations, or until the solution becomes periodic for unsteady runs. While this is somewhat intuitive, the disadvantage is that some flows require very small time steps in order to resolve certain flow features appropriately. This leads to very expensive computations that could run for weeks at a time. The relatively new frequency domain approaches are less intuitive, but are very powerful in reducing computation requirements. The idea is that the conserved variables in the governing equations are re-formulated as a Fourier series and the coefficient solved, Custer [44]. This allows for much faster solution times and fits in well with modal analyses, where the problem is already posed in terms of frequencies. This was discussed in more detail in Chapter 1.3.3.

d) Multiple vibratory modes: This is a relatively new approach that includes the impact of several modes (of natural vibration), rather than analyzing one mode at a time. The obvious advantage here is that the effects of different mode families on aerodynamic damping are captured, as well as their interactions, Mayorca [45]. Unfortunately, this is a prohibitively expensive computation for most production environments.

Other research has focused on conducting trade studies based on existing methodology/tools. The following list is intended to provide a flavor of the type of flow interactions that are relevant to aeroelastic analyses; it is by no means a complete list:

a) Axial spacing: It is typically desired to keep the space between the blades (rotating airfoils) and vanes (stationary) at a minimum in order to reduce engine length, and thus cost. However, especially for transonic rotors, there must exist enough of a gap to prevent leading edge bow waves and shocks in one row from interacting with the adjacent one. This interaction was shown by Gorrell [51] to produce a pressure field that propagated upstream, reducing pressure ratio and efficiency. In terms of aeroelasticity, a larger spacing has been reported by Hutton [52] to reduce the magnitude of the vibratory response of the rotor by as much as 50%.
b) Effect of bleed flow extraction: Traditional analyses usually account for bleed flows only by subtracting the appropriate amount of flow and applying a loss model to the flow field. It is not customary to include the extraction cavities, although today it is possible with modern tools. For aeroelastic calculations, this is still not always the norm, although Di Mare [53] showed that it may indeed be necessary for higher nodal diameters. It was also reported that ignoring the bleed flows could result in response levels being over predicted.

c) Wake strength control through flow addition: In principle this is similar to adding flow at the casing in order to control the tip gap flow. Here though, the flow was injected at the trailing edge of the upstream stator (an IGV) in order to reduce the wake strength. As a result, the vibratory amplitude of the downstream rotor was reported by Bailie [54] to have been reduced by 66%. This was for a 1st torsional mode, and was also accompanied by a moderate performance improvement.

2.6 Modeling Techniques

Of the numerical studies found, most (at least all recent ones) had an unsteady component, and some sort of validation to test data. The consensus being that unsteady modeling is necessary to capture tip leakage effects. Most were for a single passage, with some for a full annulus CFD [42, 3, 4, 55, 56, 5, 57, 46, 58, 59 and 49]. Some of these (full annulus) were for a single row [42, 3, 4 and 56], with the remainder having more than one airfoil row [55, 5, 57, 46, 58, 59 and 49]. In general, full annulus multi-row CFD is just now becoming cost-effective for research, although not yet for commercial design environments.

So far, the full annulus computational research in axial compressors has been concentrated on characterizing the unsteadiness of the flow field as it approaches a stalled condition. This has also been the aim of much of the single passage numerical research, with added variations such as flow injection/extraction, varying gap configurations, etc. From the full annulus numerical models, Kang [3] addressed

asymmetric gaps, but it was for a steady, single row and a very coarse mesh (total of ~4 million nodes), see Figure 2.6 a).

An interesting paper by Chen [5] conducted an unsteady, multi row, full wheel analysis; it dealt with unsteady effects near stall. It was a model of the NASA Compressor Stage 37 with 67 million grid points, Figure 2.6 c). In 2007, this took 240 [hrs] per solution, 1440 [hrs] for a six point speed-line (~2 months w/ 328 CPUs).

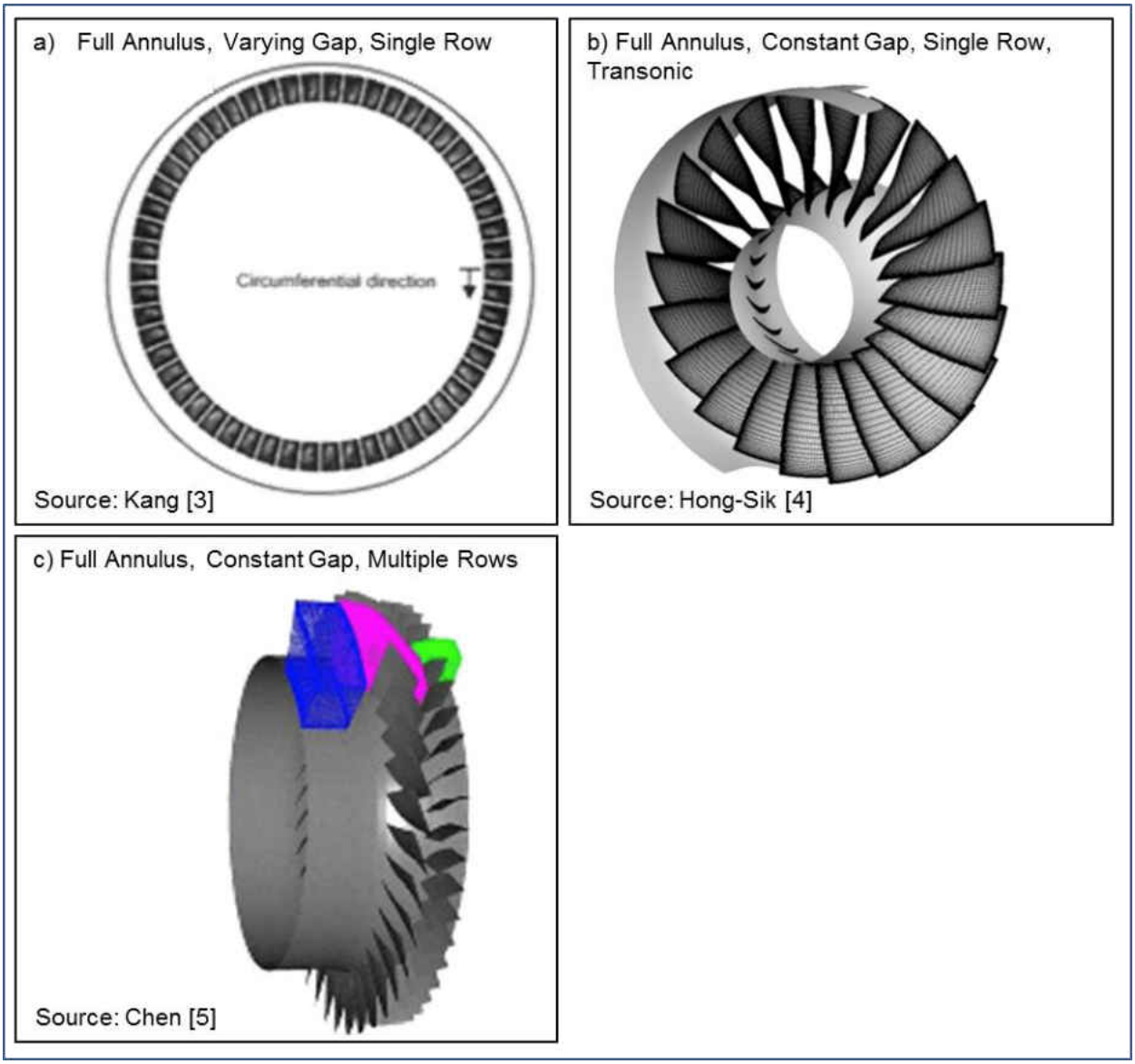

Figure 2.6: Full Annulus CFD

Clearly, this is not an ideal turnaround time for investigative purposes, let alone for production work, which is why full wheel analyses are still not the norm. In an effort to address this issue, recent advances using graphical processing units (GPU's) give hope

that such large models can be solved in more reasonable times. Brandvik [73] reported time reductions of 10x when using GPU vs traditional hardware. However, the issue of handling (not just solving) such large models still makes them unattractive. To store and manage models that consist of several tens of gigabytes for a single steady simulation is far from ideal. If an unsteady calculation is also desired, then this really becomes a prohibitive analysis for most industrial applications.

Fortunately, engineers now have other options when running unsteady calculations that would typically require either a full wheel, or some sort of simplified geometry. Recent advances in frequency domain solvers allow designers to model an entire wheel using a single passage grid. There are several codes that employ different flavors of time linearized or harmonic balance theory. In this project, the two codes utilized were: LinearTrace (from DLR) and StarCCM+'s Harmonic Balance solver (from CD Adapco).

CHAPTER 3: METHODOLOGY

3.1 Model Description

The focus of this project was to investigate the aeroelastic impact of a circumferential varying tip gap on the rotor blade. The specific stage (rotor + stator) investigated was from a mid-stage compressor airfoil of a Siemens industrial gas turbine. The investigation used separate computer models of the airfoil for both the structural and aerodynamic calculations. Test data was also utilized in the calibration of these models and for setting up the boundary conditions; more on test data will be discussed in chapter 3.3.

Figure 3.1 shows a schematic of the main tasks within each branch of the process. In general, the steady / unsteady aerodynamic solution provided the unsteady pressure on the airfoil surface. In Parallel, a structural model provided the vibratory displacements of the same airfoil surface. These two outputs were then combined to generate the unsteady aerodynamic work (work per cycle). More details on this process chain will be given in the following sections.

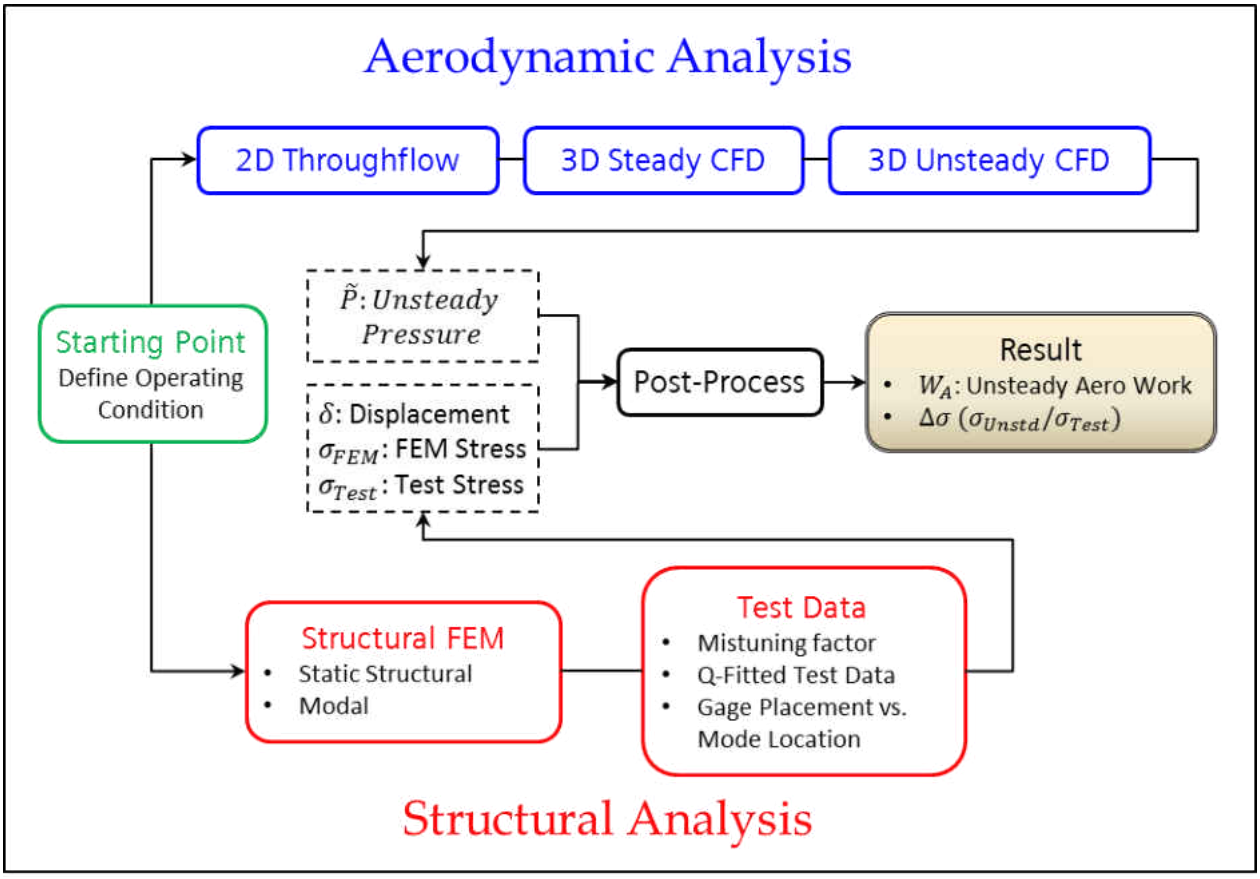

Figure 3.1: Aeroelastic Process

3.1.1 Structural Model

The structural component of the calculation consisted of an FEM of the blade+disk (stator was not modeled), with a fully hexahedral mesh. Contact elements were implemented between the blade and disk at the root attachment. The disk sector used cyclic symmetry at the periodic faces to model the appropriate sector, as shown in Figure 3.2.

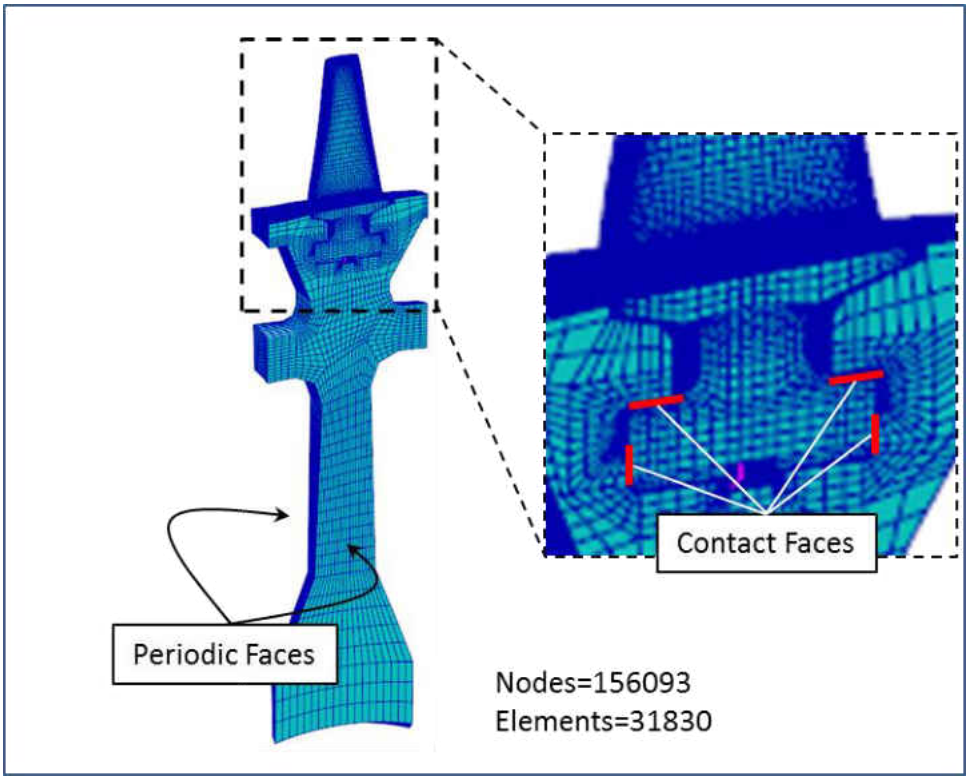

Figure 3.2: Structural FE Model

The structural analysis was run in two steps using Abaqus. The first step consisted of a static stress solution that included the centrifugal, thermal and gas pressure loads. In this step, the contact between the disk and blade was allowed to slip with a friction coefficient of 0.2. The second step was the vibratory (modal) solution, which was run to extract the first 20 modes (Eigen frequencies). For the modal analysis, the solution was run for a Nodal Diameter=24 (half the number of blades), which is the max value. This meant that all of the airfoils were assumed to respond equally, i.e. a tuned system. For certain designs, the Eigen frequencies depend on the number of nodal diameters and it

is necessary to run several ND's. This is true for blade vibration modes with a lot of participation near the root, and that are near in frequency with disk modes that also have participation in that region. However, for the conditions being investigated here, it had been previously determined that the vibratory response was independent of ND and only one ND (24) was used.

3.1.2 Aerodynamic Model

There were a couple of unconventional techniques used for the aerodynamic model of this analysis that have not been encountered in the open literature. These will be discussed in later sections. Right now, it will suffice to say that some calibration of the harmonic balance solution was first necessary.

As discussed previously, modeling a circumferential variation of the tip gap is not a common task. Also uncommon in industry (although gaining popularity in recent years), is the use of frequency domain solvers for turbomachinery applications. Since this project implemented a harmonic balance solver to circumferentially vary the tip gap, it was first desired to validate this new process chain. The overall scheme for this validation and subsequent aerodynamic calculations was:

1. Run a baseline steady solution using CFX. This was part of an established process chain that yields thrusted results (the details of this validation/calibration are outside the scope of this project). This was a single passage, constant gap model.

2. Run a corresponding steady solution using StarCCM+, and compare it to the CFX model.
3. Run a baseline unsteady solution. This was a frequency domain, time linearized calculation using LinearTrace. The CFX solution from step 1 was provided as the underlying steady flow solution. This still had a constant gap.
4. Run the unsteady solution for the harmonic balance model. This was simply accomplished by turning on the harmonic balance solver in StarCCM+. Again, still had a constant gap, so it was directly comparable to step 3.
5. Run a steady solution in StarCCM+ with a gap variation. This used a 180 degree sector model in which the gap variation was built into the mesh. This 180 degree model was later abandoned, but will be discussed to illustrate some valuable information it provided.
6. Turn on the gap variation in the unsteady StarCCM+ model. This was accomplished through the use of flutter motion; more on that later. The initial amount of gap variation was ±75% of the nominal gap, which will also be defined later.
7. Finally, additional amplitudes of gap deformation were considered: ±5, ±10, ±25, ±50 and ±65%.

This incremental set of calculations is summarized in Table 3.1.

Table 3.1: Case Matrix

Case	Label	Time Domain	Gap	Description
1	Base Steady	Steady	Constant	CFX: 1Pass: Const Gap
2	Base Unsteady	Unsteady Linear	Constant	Trace: 1Pass: Const Gap
3	Star Steady	Steady	Constant	Steady: Constant Gap
4	Star Unsteady	Unsteady HB	Constant	HB: Constant Gap
5	Star Steady Ovalized	Steady	± 75%	Steady: w/ Gap Variation: 180deg
6	Star Unsteady Ovalized	Unsteady	± 75%	HB: w/ Gap Variation: Single Pass
7	Star Unsteady Ovalized	Unsteady	±5, 10, 25 and 50%	HB: w/ Gap Variation: Single Pass

All of the aerodynamic models included the rotor and downstream stator, except for the LinearTrace unsteady baseline (case #2), which only included the rotor. These grids were generated by AutoGrid (form Numeca) and consisted of two rows: the rotor and downstream stator. Both rows were fully structured, multi-block domains generated through an automatic process chain. The inputs to the code were the flowpath definition, blade profile definitions (at several span locations) and some meta-data specific to the case: tip gap, fillet size and minimum cell heights, etc. This meshing process has been tailored for turbomachine annulus calculations, which results in the efficient, high quality grids shown in Figure 3.3.

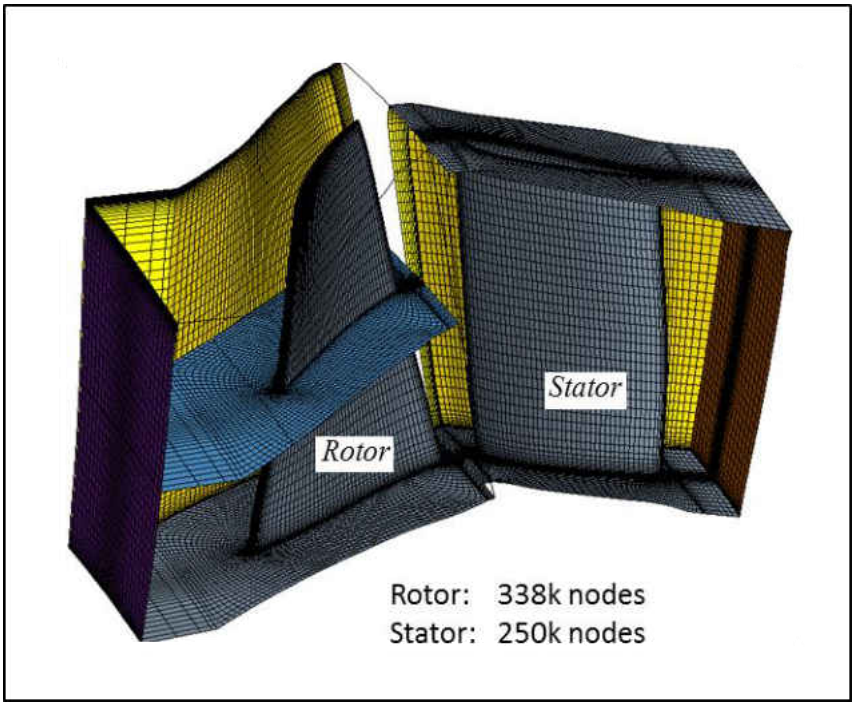

Figure 3.3: Baseline CFD Grids

As noted in the figure, the rotor count was 338k nodes and the stator 250k nodes. There was actually a coarser mesh originally available (250k and 200k nodes for the rotor and stator correspondingly), but a clean baseline was desired for this project, hence the slightly finer mesh.

Since the intent of the initial validation was to ensure a back-to-back comparison between CFX/Trace and StarCCM+, the same grids used in the baseline were imported into StarCCM+, instead of using the mesh generator available in StarCCM+.

As expected, not all settings were directly transferable since there were three different solvers implemented. Nonetheless, the final setup yielded very close results (as will be discussed later). A summary of some of the settings is shown in Table 3.2.

Table 3.2: CFD Settings

	CFX	LinTrace	StarCCM+
Grid	R06+S06	R06	R06+S06
Material Propeties			
Dynamic Viscosity	Sutherland's Law: Constant = 110.6 [K] Ref Value = 1.716E-5 [Pa*s] Ref Temp = 273.15 [K]	Sutherland's Law: Constant = 110.0 [K] Ref Value = 1.7198E-5 [Pa*s] Ref Temp = 273.0 [K]	Sutherland's Law: Constant = 110.6 [K] Ref Value = 1.716E-5 [Pa*s] Ref Temp = 273.15 [K]
Gas Constant	-	R = 287.102 [J/(kg.K)]	-
Specific Heat Ratio	-	gam = 1.3771	-
Molecular Weight	28.96 [kg/kmol]		28.96 [kg/kmol]
Specific Heat	4th order poly. f(Temp)	cp = 1048.44 (constant)	4th order poly. f(Temp)
Ref. Temperature	273.15 [K]		273.15 [K]
Thermal Conductivity	Sutherland's Law: Constant = 194.4 [K] Ref Value = 0.02414 [W/(m K)] Ref Temp = 273.15 [K]	- - - -	Sutherland's Law: Constant = 194.4 [K] Ref Value = 0.02414 [W/(m K)] Ref Temp = 273.15 [K]
Turbulent Prandtl No.	0.9		0.9
Solver	Steady State Turbulent SST w/ reattachment Wall Function High Speed	- - - - - -	Steady All y+ Wall Treatment Coupled Energy Coupled Flow: Implicit 2nd Order K-Omega Turbulence RANS
	- - - -	Time Linearized -- Frequency domain 2nd Order NSTurbulent Frozen Mu	Harmonic Balance --NonLinear frequency domain
Rotor-Stator Interface	Mixing Plane	Non-Reflecting Giles2	Non-Reflecting: 10 modes

3.1.2.1 Grid Independence

One final note on the aerodynamic model was a grid refinement study. The initial working models for the steady (CFX) solution came from a standard process chain at Siemens. The standard meshing approach for this type of production environment is to generate the coarsest mesh that will yield an accurate solution. However, this type of grid does not always provide enough fidelity for academic purposes. Further, to capture unsteady effects, this level of mesh coarseness may not always be adequate depending on the information sought. As an example, and directly applicable to this project, the tip gap region only contained 9 grid points. This can capture overall steady effects fairly well, but not the detailed information sought in this project. By contrast the propagation of the bow-wave emanating from the downstream leading edge was captured adequately. It contained enough points to capture the circumferential pressure variation, as shown in Figure 3.4.

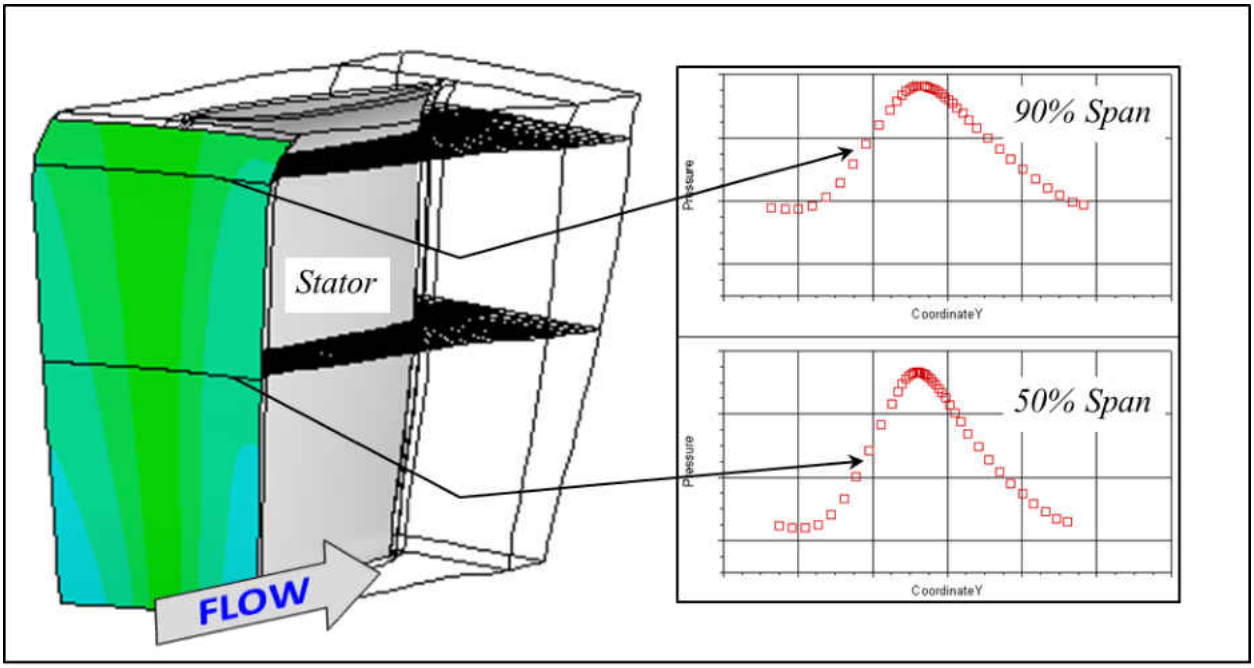

Figure 3.4: Acoustic Wave Grid Density

Since the end goal was to quantify an aeromechanic effect, the unsteady work was used as the figure of merit for this grid independence study. For this task, the rotor grid was refined mainly along the radial direction, with the necessary accompanying refinement in the other two directions. The stator grid was not modified since that flow domain was only present to provide the correct forcing function to the unsteady solution, but no detailed information was sought there. The final grid used consisted of ~1.1 million points in the rotor domain, with 25 points in the tip gap. Figure 3.5 shows the extremes of the different grids attempted.

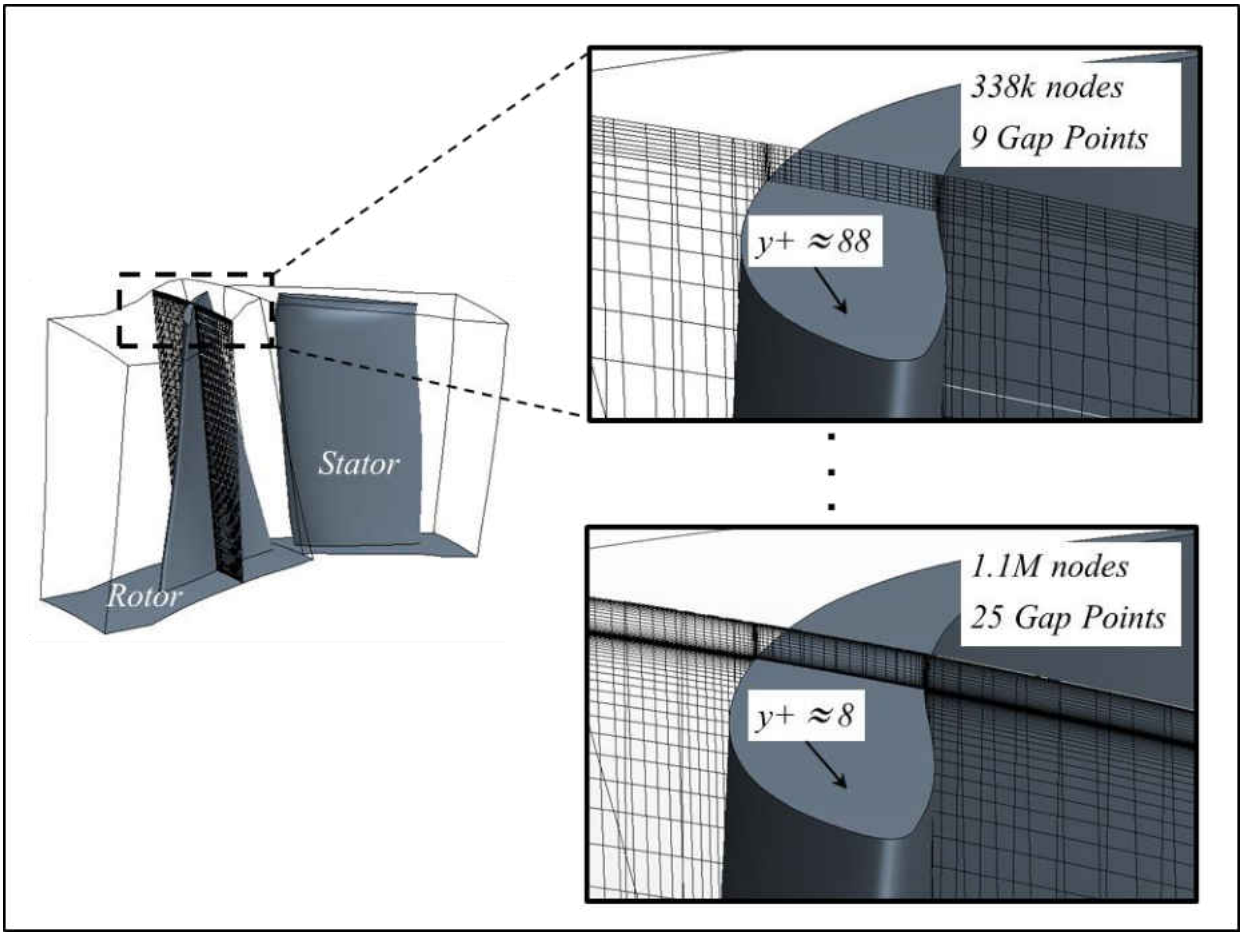

Figure 3.5: Grid Independence: Tip Mesh

As noted in the figure, the increased number of points in the tip gap reduced the y+ value from ~88 down to ~8; a factor of ~11 reduction. There was another finer grid run of roughly ~1.5 million points which showed that the solution did not change much between 1.1 and 1.5 million. Therefore, all final calculations were performed with the 1.1 million nodes model. This grid sensitivity was carried out and the work per cycle plotted for the various meshes, see Figure 3.6.

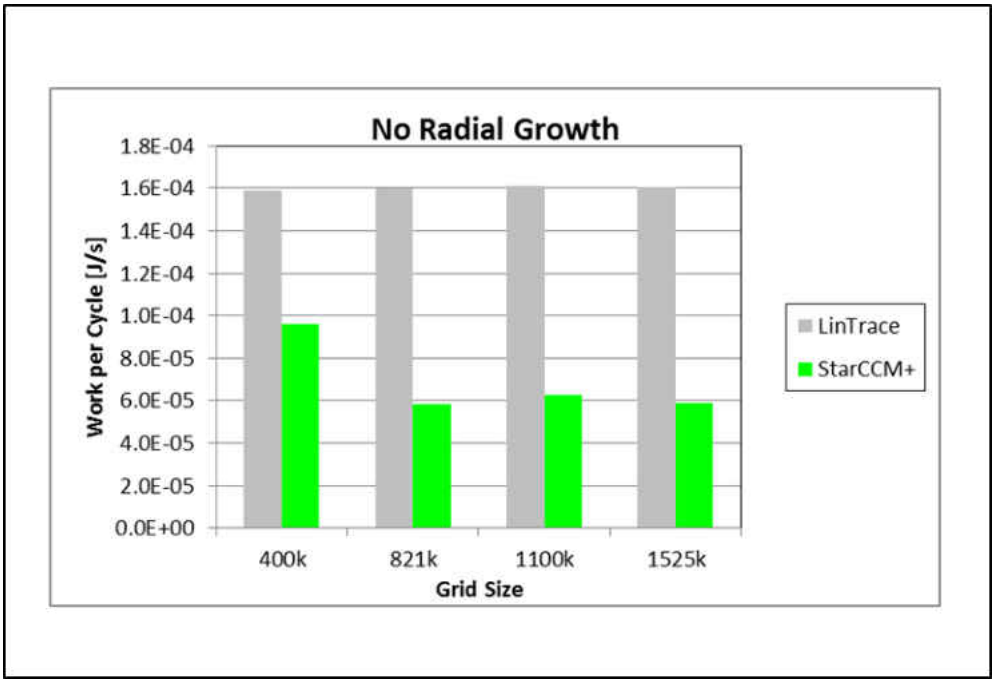

Figure 3.6: Grid Independence: Work per Cycle

The plot shows the work per cycle calculated for the case where the gap was not varying. For this configuration, the work was calculated with both LinearTrace and StarCCM+ (cases #2 and #3). The plot shows that LinearTrace (gray bars) was insensitive to the grid refinement. By contrast, StarCCM+ was very sensitive for the coarsest mesh. The plot also shows that the work per cycle in the LinearTrace solution was ~2.6 times larger than in the harmonic balance solution. Differences of similar magnitude have been observed by other investigators, Li [60]; further details for the differences seen in the present project will be discussed later. A similar trade study was conducted for the Aerodynamic work from the model with a tip gap variation of ±75%.

Those results will be shown in section 4.6; for right now, it will suffice to mention that they also demonstrated a grid independent solution.

.

3.2 Boundary Conditions

3.2.1 Operating Conditions

The geometry and conditions analyzed were obtained from an actual Siemens industrial gas turbine compressor mid stage. The airfoil count and other parameters of interest are shown in Table 3.3 in non-dimensional form.

Table 3.3: Operating Conditions

Variable	Units	Value
Num Rotors	[-]	48
Num Stators	[-]	72
Rotor Speed	[%]	97%
Pt Ratio	[-]	1.25
Aspect Ratio	[-]	0.42
TipClearance/Height	[%]	0.53%

3.2.2 Structural BC's

As discussed previously, one of the two main inputs to the aeromechanic model came from a structural analysis of the blade. Specifically, it was a modal (vibratory) analysis that took into account the centrifugal loading, the gas pressures and temperature. Figure 3.7 shows the pressure loads applied to an Abaqus FE model of

the blade. The thermal environment for this compressor mid-stage was fairly benign, so a constant temperature of 200 [^{o}C] was used. This was a valid assumption since the main source of air heat up came from the compression process and there were neither combustion hot spots, nor any active cooling as in the turbine. Therefore, the metal temperature would result in a relatively uniform field.

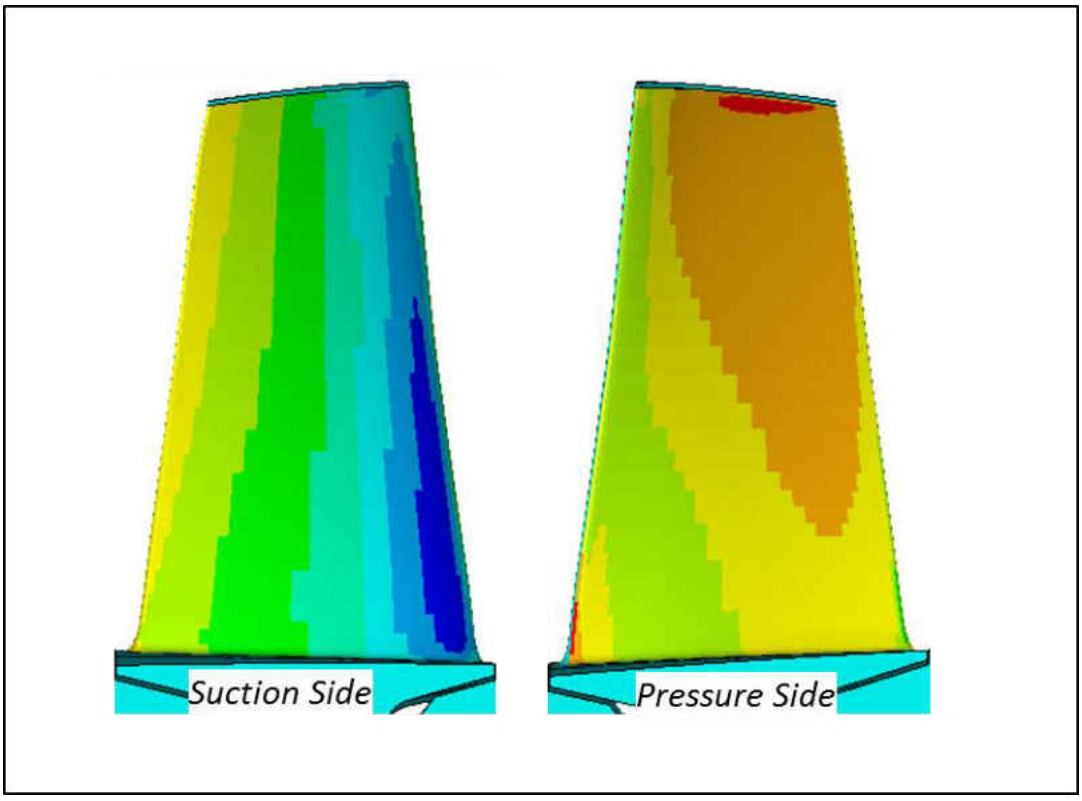

Figure 3.7: FEM Pressure

This airfoil design was known to have a vibratory behavior independent of the disk. Therefore, only one nodal diameter was run (ND= No.Blades / 2 = 24), with 20 modes

(Eigen frequencies) extracted. For this particular blade, test data showed a response of the chord-wise second bending mode at an off-design operating point, as shown in Figure 3.8; more on test data in chapter 3.3. This FEM solution was obtained by running a structural static analysis in a first step, and then solved for the Eigen frequencies in a second step that used the first step as a pre-stress condition.

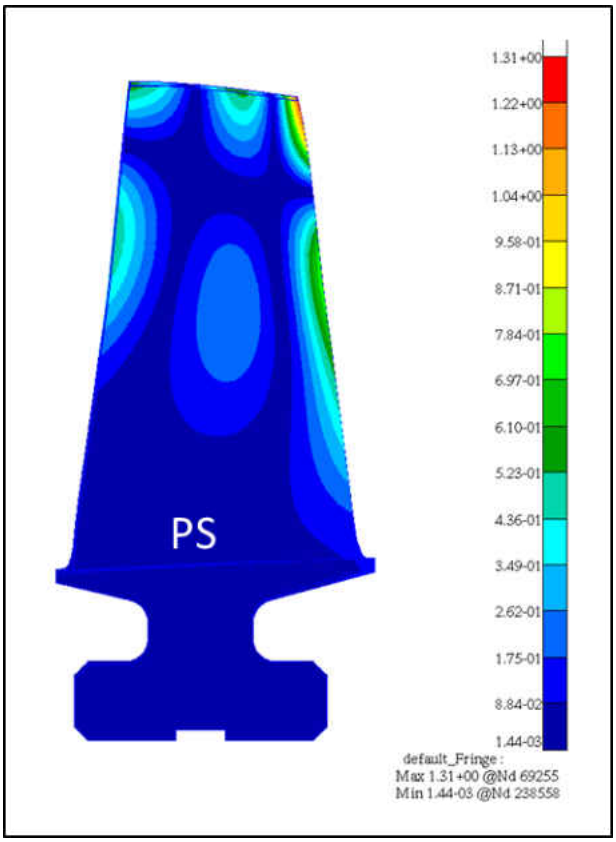

Figure 3.8: FEM Mode Shape: Chord-wise 2nd Bending

The results of this modal solution were used as a boundary condition to the aeromechanic model, which used a different mesh (it used the aero mesh). The process of mapping these displacements from the FEM mesh onto the CFD grid was performed by the LinearTrace code automatically; results of this mapping are shown on Figure 3.9. For the StarCCM+ model, a mapping routine was written in python. It yielded nearly identical results, so they are not shown.

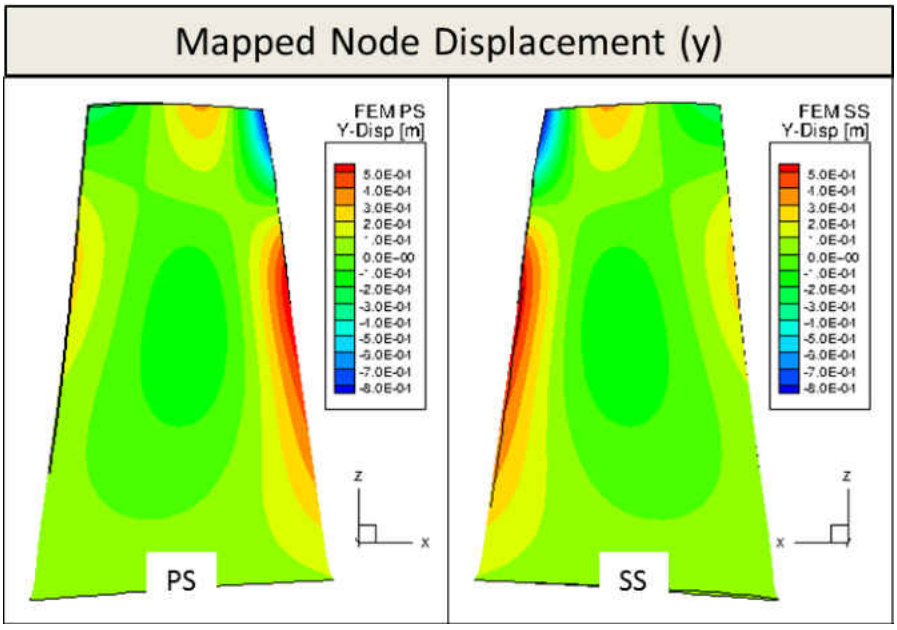

Figure 3.9: Mapped FEM Displacements onto CFD Grid

3.2.3 Aerodynamic BC's

The boundary conditions to the CFX steady model consist of flow variables profiles specified at the inlet and exit of the domain. This steady solution in turn becomes a

boundary condition to the unsteady LinearTrace solver. For the harmonic balance approach, only the flow variables at the inlet and exit are specified. The code then solves both the steady and unsteady solutions from these profiles.

The two main approaches for specifying boundary conditions for turbomachinery steady aerodynamics are to define either a pressure ratio, or the mass flow; the former was used in this project. For this type of boundary, radial distributions of total pressure, total temperature and flow angles were specified at the inlet of the rotor domain. At the exit, only the static pressure was necessary to define the pressure ratio across the domain. The flow angle distributions are shown in Figure 3.10 in non-dimensional form. From here it can be seen that the radial angle around the midsection was nearly zero, while there was a small radial component near the walls (at span = 0.0 & 1.0). This was the expected distribution for a converging compressor flowpath, and a direct result of the radial equilibrium condition. The tangential angle also had a small change from hub to tip, which of course manifests itself in the blade twist along the span.

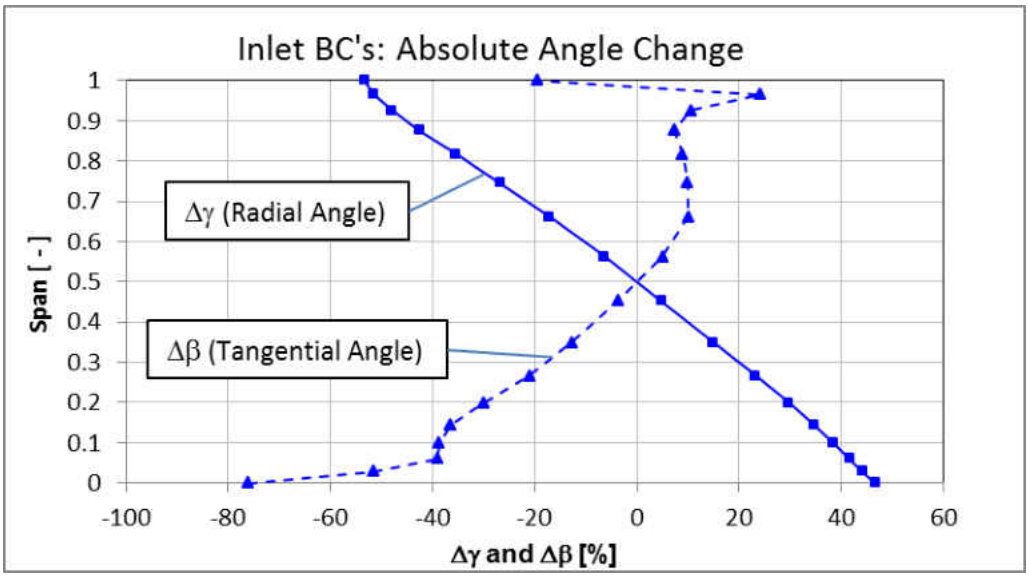

Figure 3.10: Aero BC's: Inlet Flow Angles

The non-dimensional temperature and pressure radial distributions are shown in Figure 3.11. The plot shows that the pressure coming in (Ptot.in) is hub-strong, while the temperature has a flatter profile.

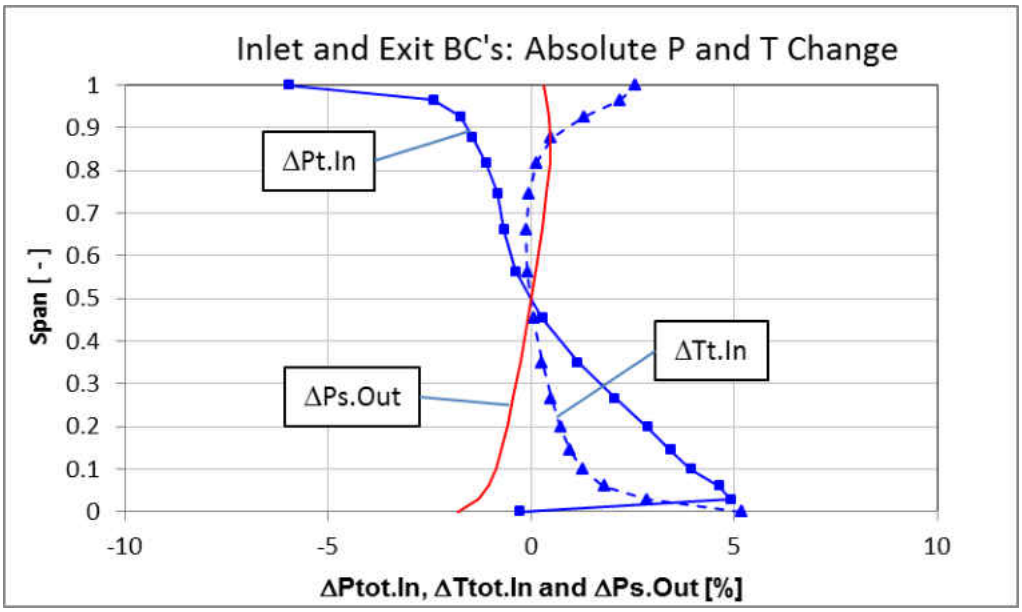

Figure 3.11: Aero BC's: Temperature and Pressure Distributions

3.3 Test Data

In order to calibrate the FEM and CFD models as well as the overall analytical processes, two separate sets of test data were utilized. These were not from experimental setups, but rather measurements from an actual engine. The benefit of such data is that these are 'real world' measurements, not idealized conditions in a controlled environment. This adds a certain level of validity and practicality that is sometimes missing from rig experiments. The downside is that there are lots of variables at play during a real engine test. Many of these are simplified, or ignored altogether in analytical models. Controlling them is also a big challenge, so there is a certain level on uncertainty associated with every factor that influences this test data:

tolerances, ambient conditions, blade-to-blade variability, instrumentation survivability/error, etc.

The first set of data was from a Siemens engine (engine 1), which provided information to define the circumferential gap variation. This engine was not the same for which the present study was conducted, but it provided the desired set of data that could be scaled to fit the desired conditions. The second set of data was from the actual Siemens engine being studied here (engine 2). This data was directly used to calibrate the vibratory results. The reason for having test data from two different engines is that engine 2 provided data for the vibratory response, but did not have tip gap measurements. Conversely, engine 1 provided good tip gap measurements, but no vibratory information.

3.3.1 Ovalization Definition

Enough measurements of casing ovalization are not always part of a standard production engine monitoring. Nevertheless, tip gap data was available for a few rows, at a few circumferential locations. Although this data did not paint a complete picture of the casing ovalization, it was enough to create an envelope of the magnitude of ovalization that could be experienced in a real engine. Figure 3.12 shows these measured tip gaps using a linear, non-contact, capacitive probe. This particular type of probe had a range of measurement of <4.5 [mm], with a tolerance of 1%, which was within the levels measured. They were installed into the casing at four circumferential locations, as shown in the left picture. The right picture shows the measurements as a

function of time. The scales on this plot were normalized due to proprietary reasons; however, the main piece of information extracted from this data was the overall deformation of the casing. The data suggests that the casing was warped by a maximum of ±80% form the nominal. This proved to be too much to handle in the analytical models, so this project used ±75% as the max circumferential variation.

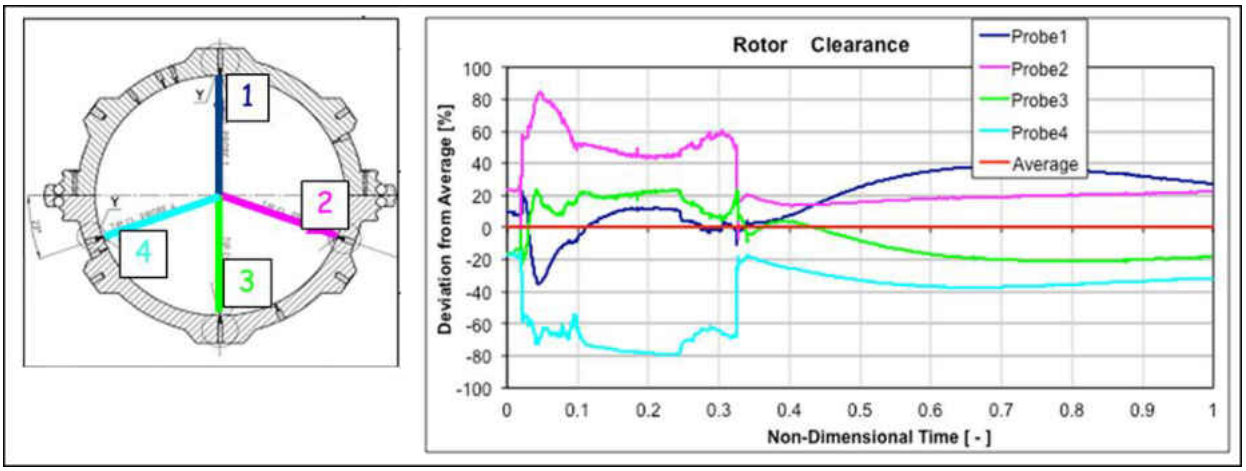

Figure 3.12: Test Data: Measured Tip Gaps

This information was utilized to define a generic casing ovalization, as shown in Figure 3.13. This definition utilized mirror symmetry about the main vertical and horizontal axes. So it was an idealized shape, a little different from the less uniform shape implied by Figure 3.12. However, this symmetrical shape was better suited for numerical modeling.

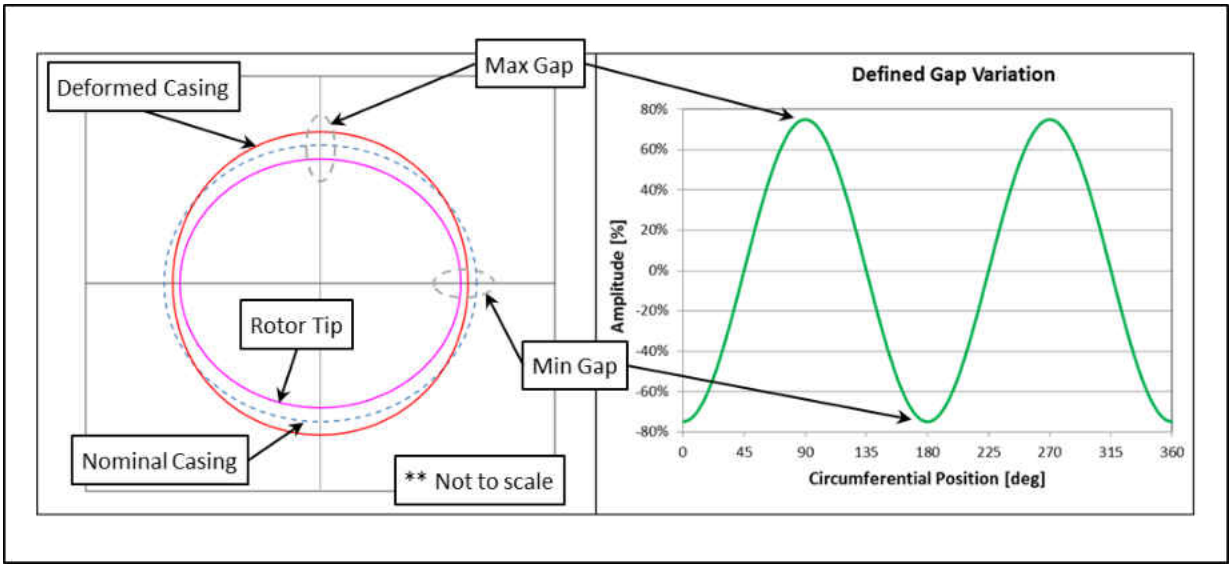

Figure 3.13: Defined Ovalization

Having the desired shape, the next (and more difficult) step was to build a CFD model that captured it. There were a few different alternatives attempted to accomplish this, three of these are discussed next.

I. This initial intent for this project was to model a half wheel for the rotor (so 24 rotors - still a single passage stator) with the casing ovalization built into the mesh. This was actually built and run up to the steady solution. Unfortunately, in this type of model each blade would see a different gap, but that gap would be constant for any one particular blade. However, the goal for this study was for a single blade to see a different gap as it rotated around the annulus, so this model was abandoned. Like the baseline, this grid was also built in AutoGrid, but it used the node projection capability for

capturing the ovalization. The process involved generating a regular, half wheel axisymmetric mesh. Then, the ovalized casing surface was imported and the nodes representing this casing were projected toward the new surface (other nodes in the vicinity were also stretched). Only a steady solution was obtained, and it will be shown to compare the differences with respect to the final approach adopted and the baseline.

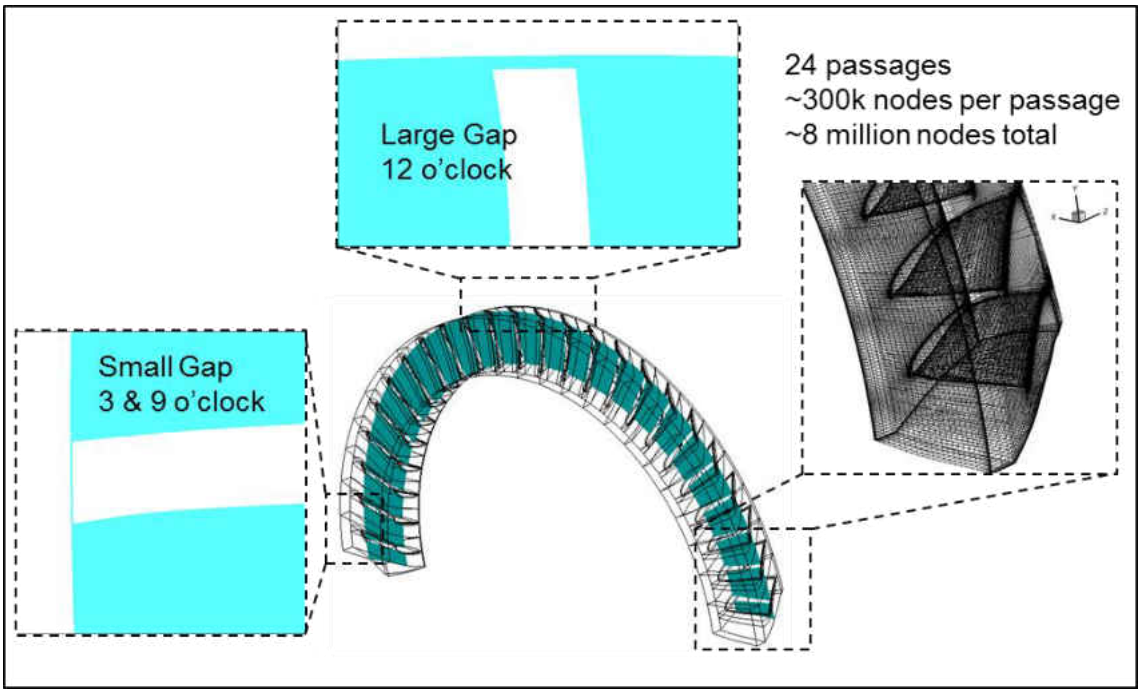

Figure 3.14: 180^{o} Mesh

II. In the next attempt, a single passage was modeled with flutter motion of the casing surface. This was a good representation of the physics because from the rotor's frame of reference, the casing was the one moving and it

generated the circumferential gap variation sought for a particular blade. However, this posed a problem for the harmonic balance solver since the movement of the casing along the circumference generated slightly different adjacent passages. In turn, this generated non-cyclic periodic walls that violated the periodicity assumption inherent to the harmonic balance approach. Several attempts to run this configuration failed.

III. The final attempt was to model a single passage and apply a radial motion to the blade: max deflection at the tip, while holding the hub constant. So the airfoil was stretched and compressed at twice the rotation frequency to generate the ovalized tip gap. This captured the desired effect of the gap variation over the same blade and the periodic walls remained compatible for a harmonic solution; it also allowed for faster running time versus the half annulus model. The fact that the blade height was not constant meant that the radial distribution of the flow angles also changed. However, because the gap change was relatively small compared to the blade height, this was considered to be a small error.

3.3.2 Strain Gage Measurements

This next set of data corresponded to strain gage measurements on the blade surface. For this specific rotor, this data showed that the airfoil responded at a very specific operating condition. Figure 3.15 shows the speed sweep during which the blade

responded. This can be clearly seen by the spikes in Amplitude at a rotor speed of ~97% in both the ramp down and ramp up.

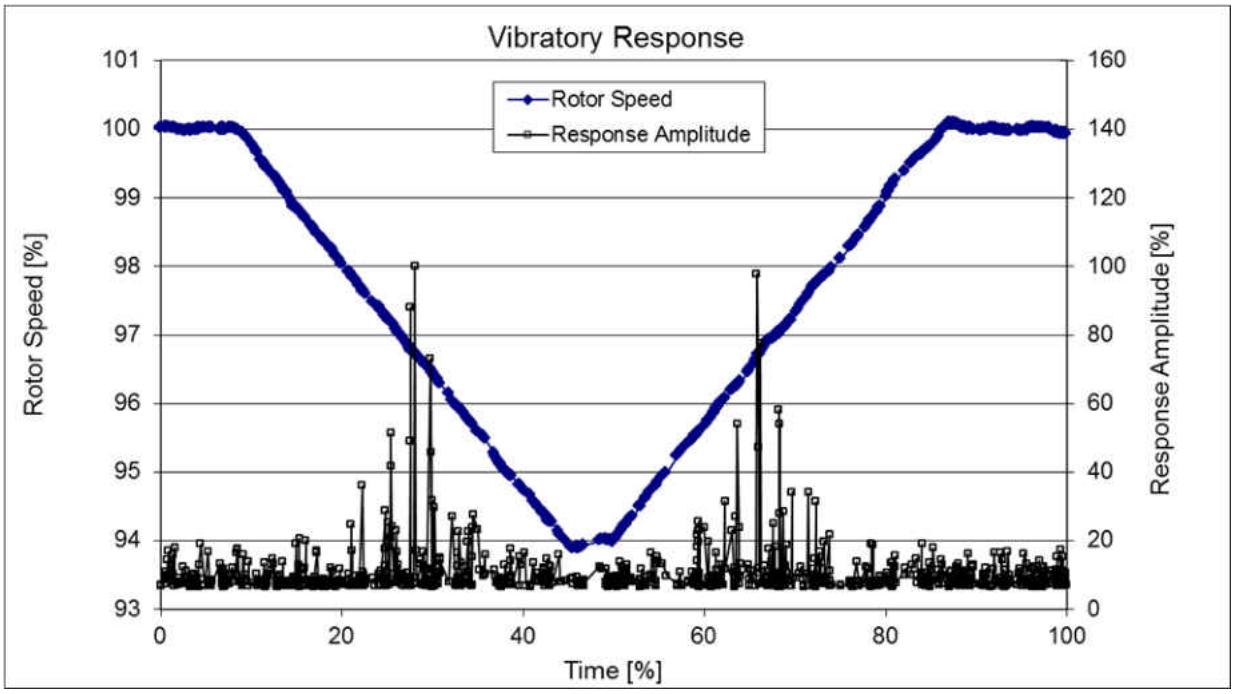

Figure 3.15: Test Data: Speed Sweep

The corresponding response frequency for this test is shown in Figure 3.16. In the figure, the two largest amplitudes stand out at engine order (EO) drivers of 72 and 36 respectively. The 72 EO driver was clearly the stator count; this is why the aeromechanic model consisted of the excited rotor and downstream stator. The 36 EO driver did not correspond to any other airfoil count in this compressor, nor to the count difference of the neighboring rows. It is difficult to pinpoint the source of this driver, but one possible explanation could be that this is half of the downstream count. So if the

casing was ovalized it could have generated two distinct flow fields around the circumference, hence introducing a 36 count driver.

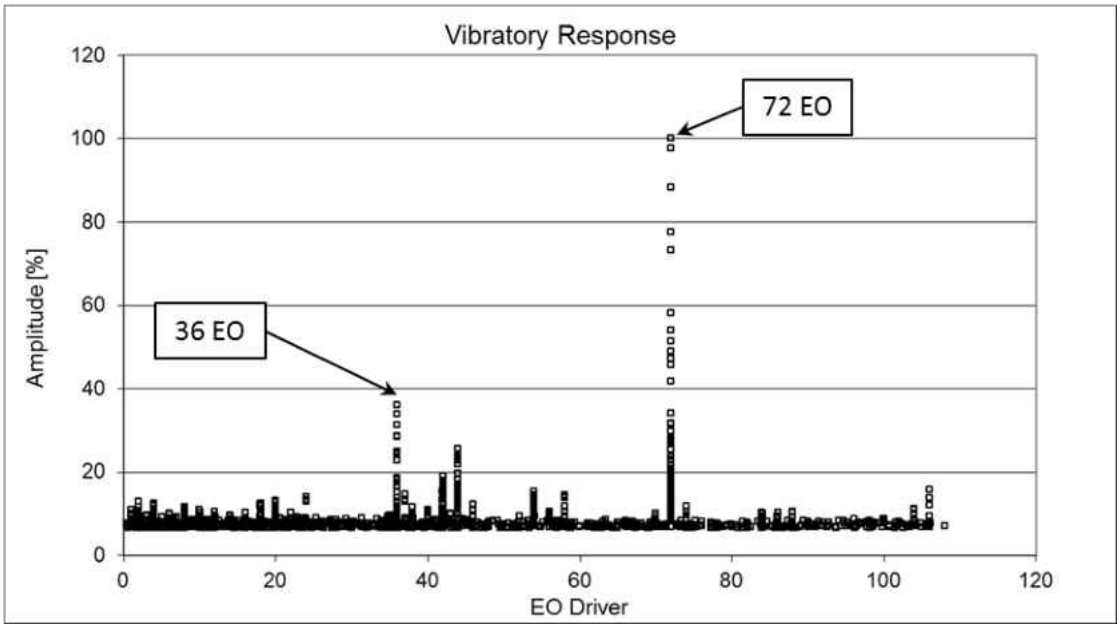

Figure 3.16: Test Data: Response Amplitude vs. Engine Order

The corresponding non-dimensionalized Campbell diagram can be seen in Figure 3.17. The plot points out that the calculated blade frequency was within 0.2% of the measured value, which was very accurate. The crossing with the 72 EO is also depicted at the off design point.

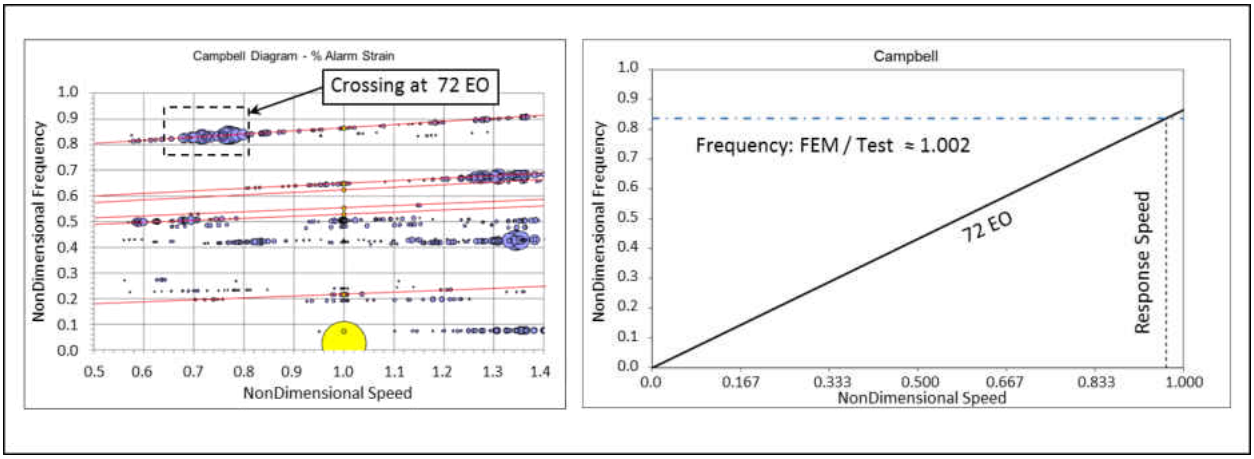

Figure 3.17: Test Data: Campbell Diagram

In summary, this data showed that the blade responded due to a 72 EO driver, which corresponded to the downstream vane count crossing near 97% speed. For this blade, the corresponding vibratory mode was a chord-wise second bending (CW2B) mode with an Eigen frequency near this crossing.

CHAPTER 4: RESULTS AND DISCUSSION

Throughout this project there were several CFD models utilized for validation of the harmonic balance solver and the variation of the tip gap, as summarized in Table 3.1. This chapter will cover these results in the same order presented in the table; but first, a word about convergence.

4.1 CFD Convergence

The convergence of a CFD simulation continues to be a topic of debate since there are different ways to judge convergence, and it is often left to the engineer to exercise judgment on when a run can be stopped. Momentum and energy residuals are typically used, and for turbomachinery applications, mass flow convergence is often monitored as well. Other parameters are additionally monitored depending on the specifics of a particular case. For this project, the work per cycle was also monitored, as was shown in the grid independence section.

The residuals for both the linearized and harmonic balance solvers are shown in Figure 4.1. At first glance, it is obvious that these residuals were not comparable between the two solvers. In LinearTrace only one value (L2 Residual) was tracked, and it reached a much lower level than any of the tracked residuals in StarCCM+. In most CFD codes, residuals typically drop to ~1E-04→1E-06, but in StarCCM+ the residuals were much higher. However, they had already plateaued, and more importantly, other parameters (mass flow and work per cycle) were also converged.

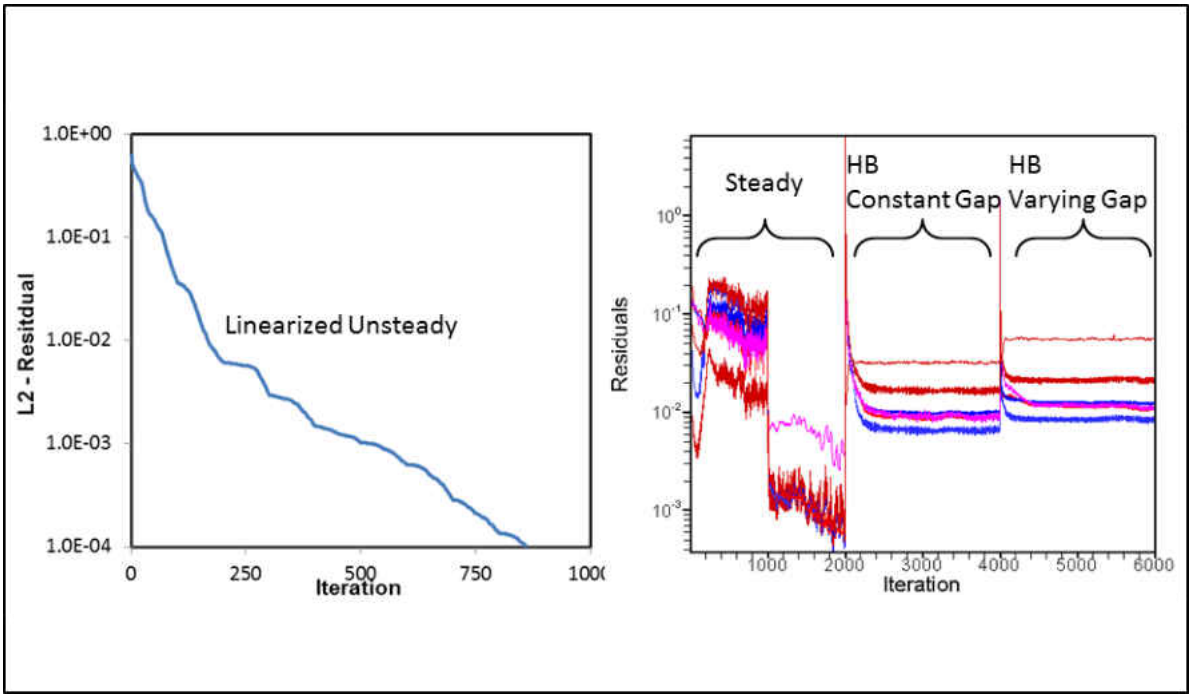

Figure 4.1: Residual Convergence

Figure 4.2 shows that the mass flow in the harmonic balance solution was also well converged. For the StarCCM+ solution, initial runs were taken to 15,000 iterations with no difference in the residuals, so the final runs were only taken to 6000 iterations. This figure also shows the unsteady pressure at a point approximately in the center of the airfoil pressure side. This was a convenient way to monitor the solution as it converged since the work per cycle was an external post-processing step. This unsteady pressure also showed the difference between the constant gap vs. gap variation studies, both of which were equally well converged.

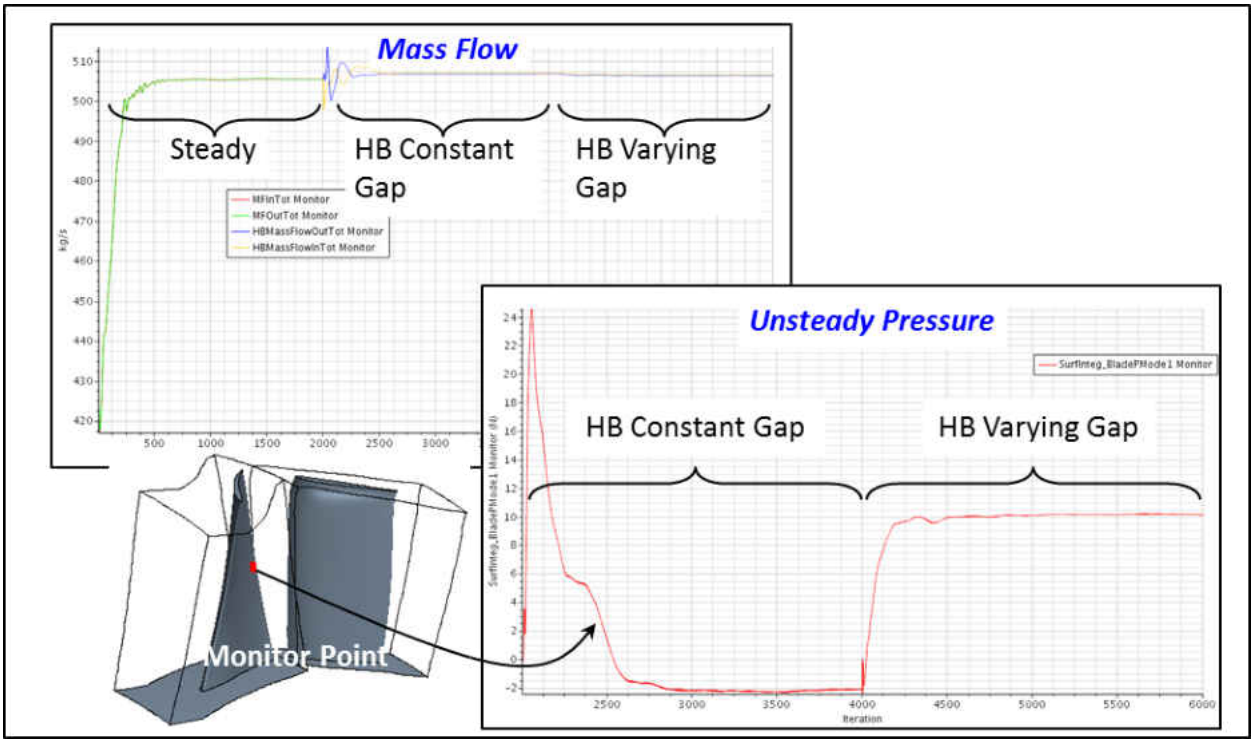

Figure 4.2: Mass Flow Convergence

The final parameter tracked for convergence was the work per cycle. The final values were already shown in the grid independence study, but in Figure 4.3 they are shown at several intervals through the convergence history. In reality this is the one parameter of most significance for this project, so its' convergence dictated when a particular run could be stopped. The figure highlights a very significant aspect of the calculations that was initially missed. Although the typical variables (mass flow & residuals) showed a converged solution, the work per cycle took longer to converge, and even after ~3,000 iterations (when mass flow and residuals were already

converged) there was a small variation. This simply underscored the difficulty, and sometimes ambiguity, of judging convergence on unsteady calculations.

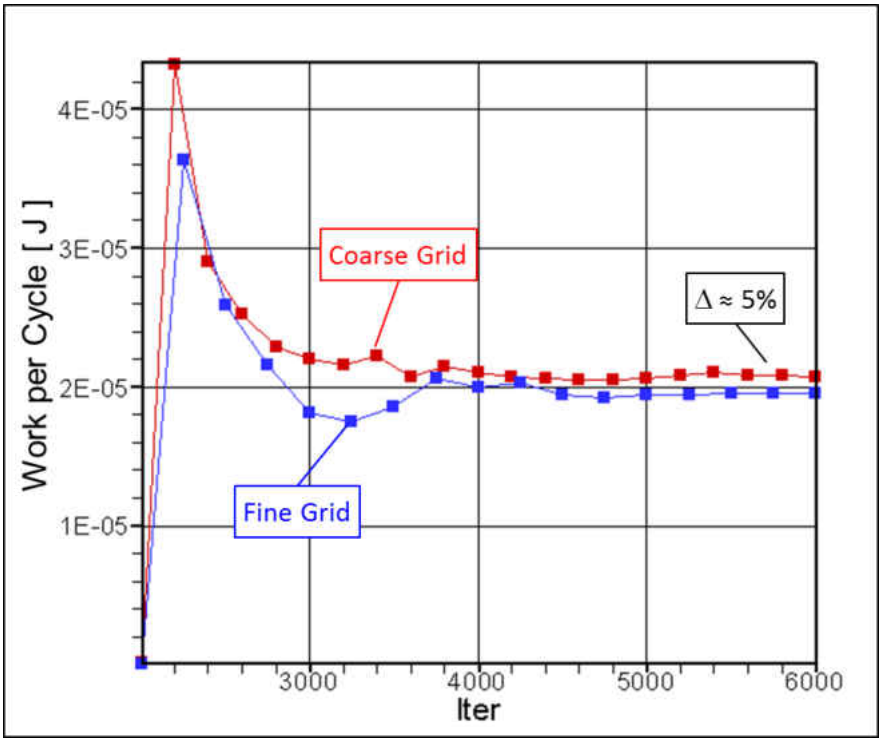

Figure 4.3: Work per Cycle Convergence

The next sections of this chapter show the initial calibration of the harmonic balance solver, followed by the results from the gap variation. This is presented in the same order as shown in Table 3.1.

4.2 Constant Gap: Steady Solution

The first step to validate the harmonic balance solver in StarCCM+ was to run a constant gap steady solution and compare it with the CFX steady solution. Figure 4.4 shows pressure contours from both codes on a blade-to-blade (BB) section at 10% span; the corresponding blade surface loading is shown as well. The span was defined at the blade leading edge (0% at the hub, 100% at the casing). So the actual blade tip was < 100% span, and the BB section shown (98.5%) was right below the tip surface.

In general, it can be seen that there was good agreement in the pressure distribution for both the blade and vane. There were only minor differences in the loading distribution (line plot) of the blade; vane loadings were almost identical (not shown). However, those differences in the blade (<2%) were limited to a small section (SS ~70% chord) and probably within the error in the analysis. Also evident from the figure, is that the steady solution in StarCCM+ implemented the same “mixing plane” assumption at the rotor-stator interface as CFX. The step change at the interface showed that there was no circumferential variation passed between the rotor and stator domain in either code. This was in contrast to when the unsteady (harmonic balance) solver was turned on (discussed later).

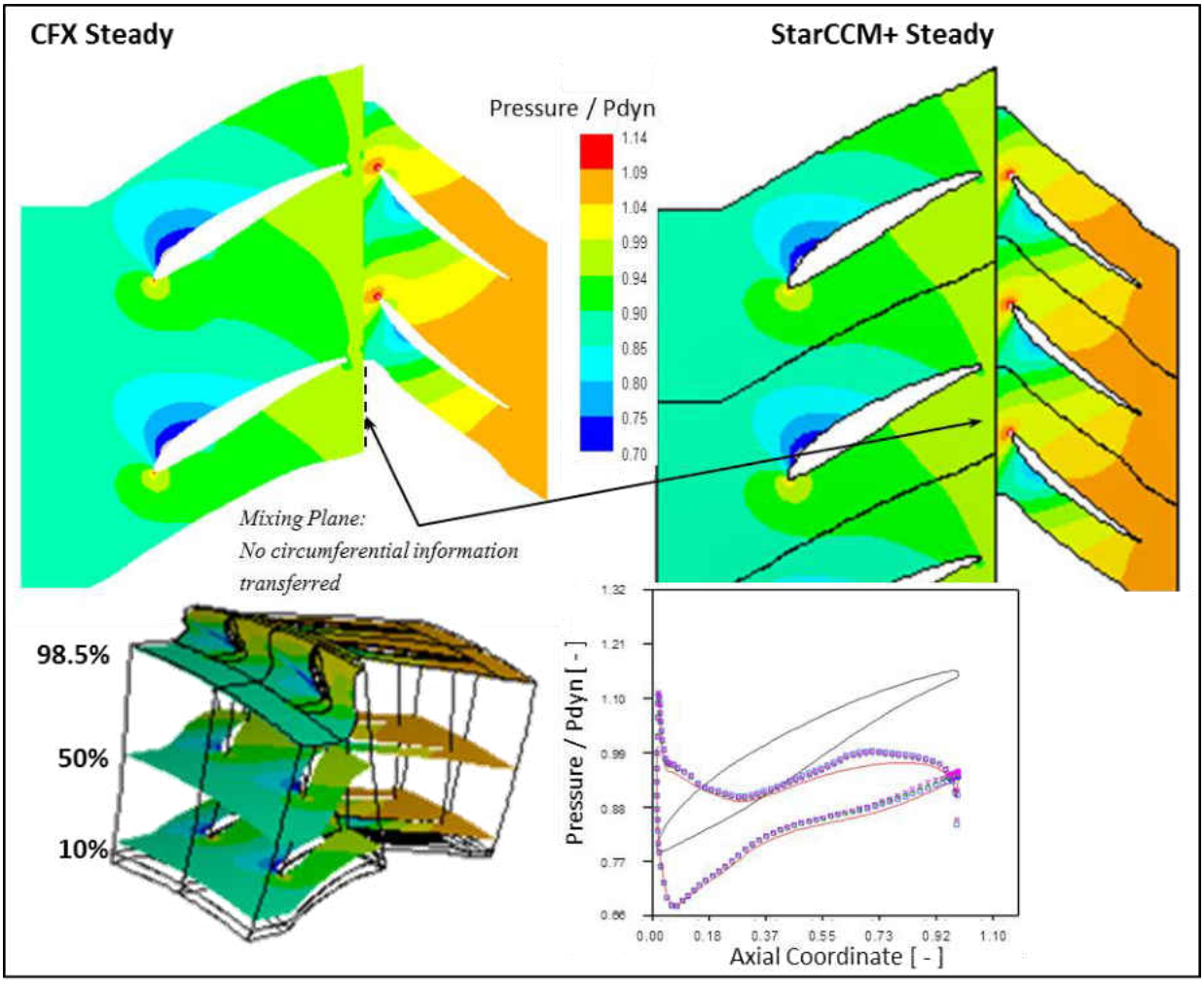

Figure 4.4: Steady Pressure: 10 span%

The pressure, temperature and Mach number are commonly used to compare steady solutions. However, variations in the tip leakage flow do not always come across clearly in these variables. For looking at the tip flow, contours of entropy better revealed the desired variations. Unfortunately, the CFX and StarCCM+ definitions of entropy were not directly comparable. Therefore, a text book definition was implemented in both

codes, as prescribed by Equation (4.1), with the reference state: *T*1=273.15 [K] and *P*1=101325 [Pa].

$$\Delta s_{1-2} = cp * ln\left({}^{T2}/_{T1}\right) - R * ln\left({}^{P2}/_{P1}\right) \qquad (4.1)$$

Similarly, contours of axial velocity replaced Mach in order to better show reversed flow regions. The final entropy and axial velocity contours also showed close agreement between the two solutions at 10% span, see Figure 4.5.

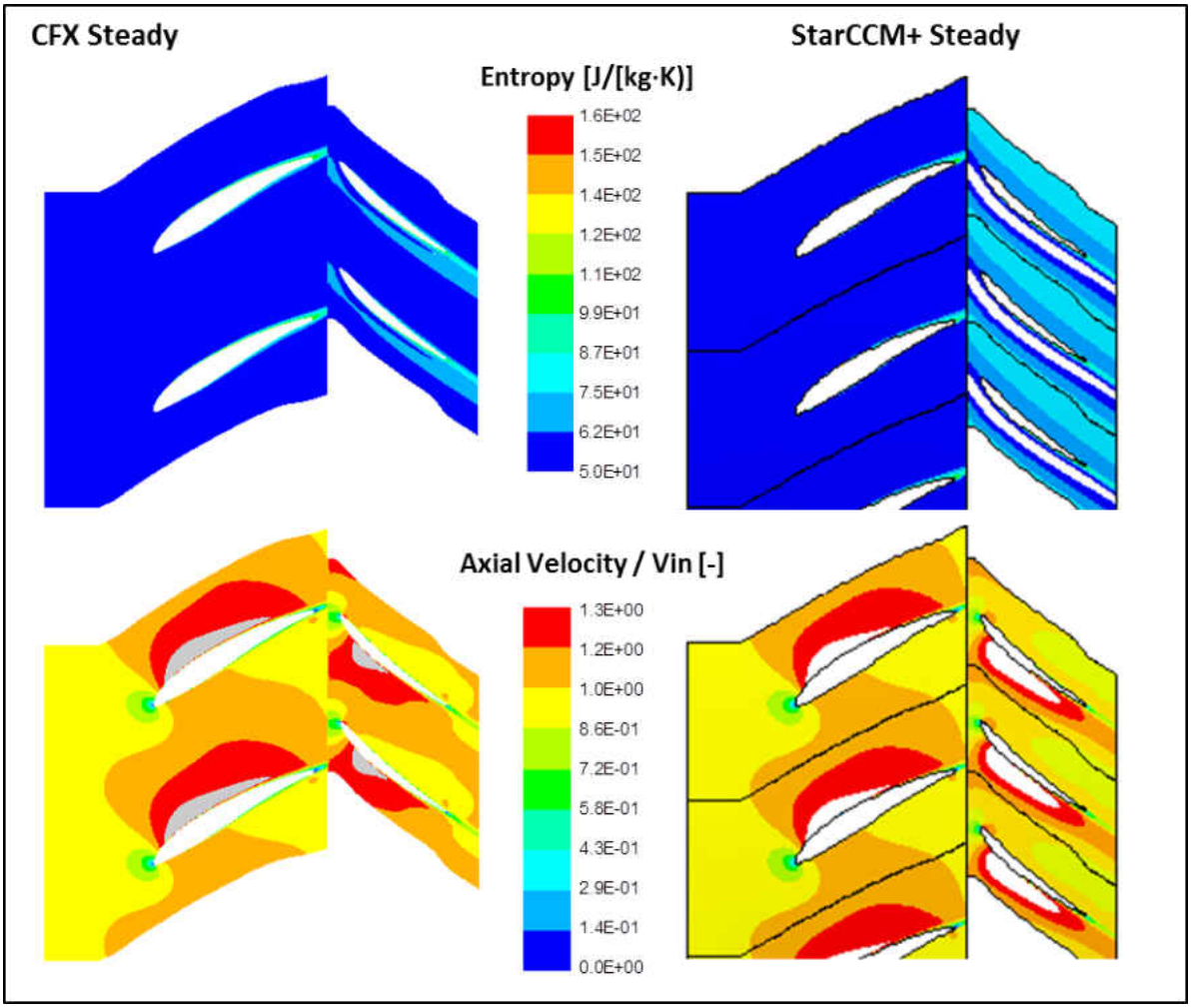

Figure 4.5: Steady Entropy and Axial Velocity: 10% span

Similar comparisons at 50% span are shown in Figure 4.6 and Figure 4.7. At this mid-span, the two solutions were even closer than near the hub. This was expected because this section was the furthest away from the end-walls, which are more susceptible to code specific treatments of the walls.

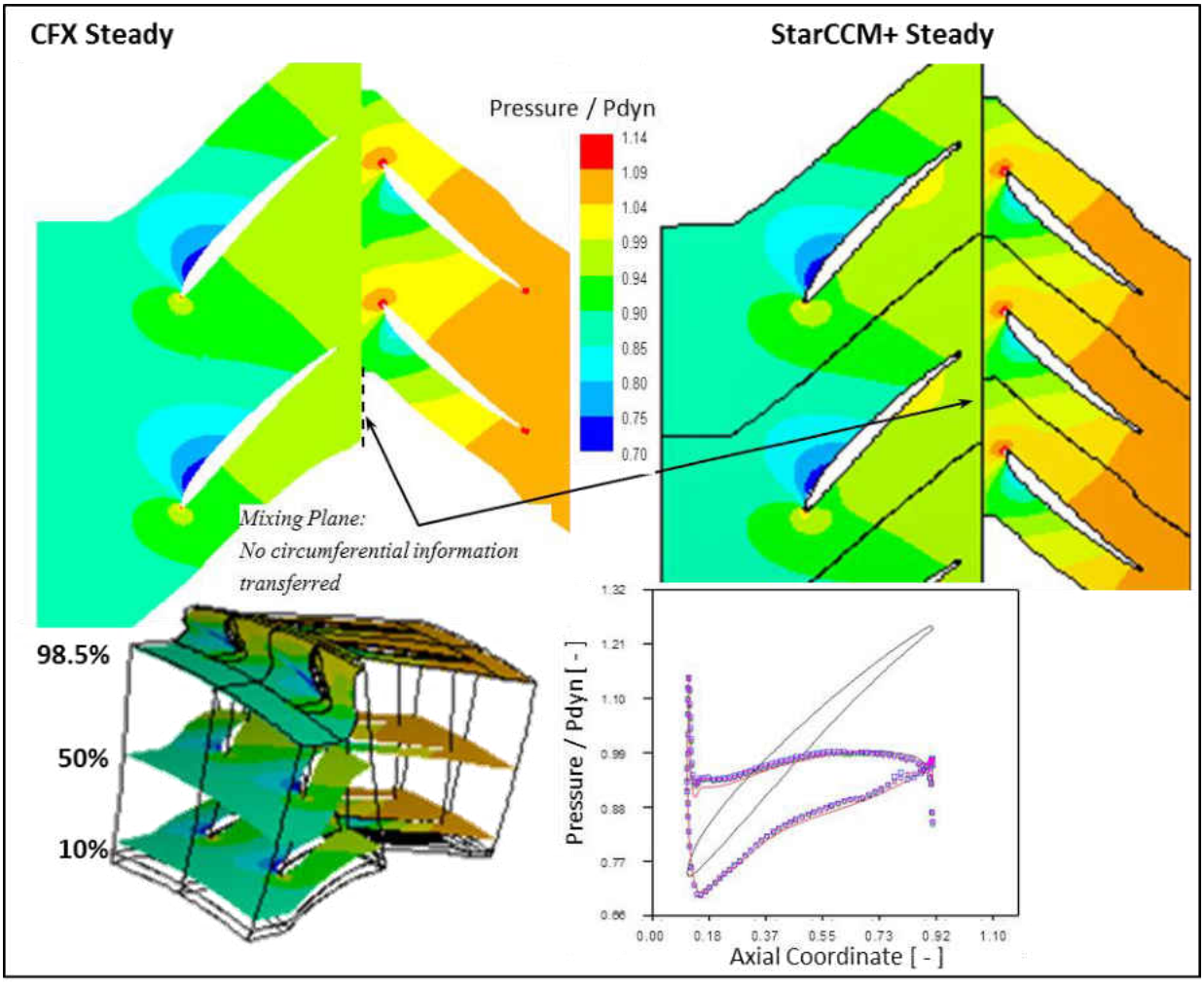

Figure 4.6: Steady Pressure: 50% span

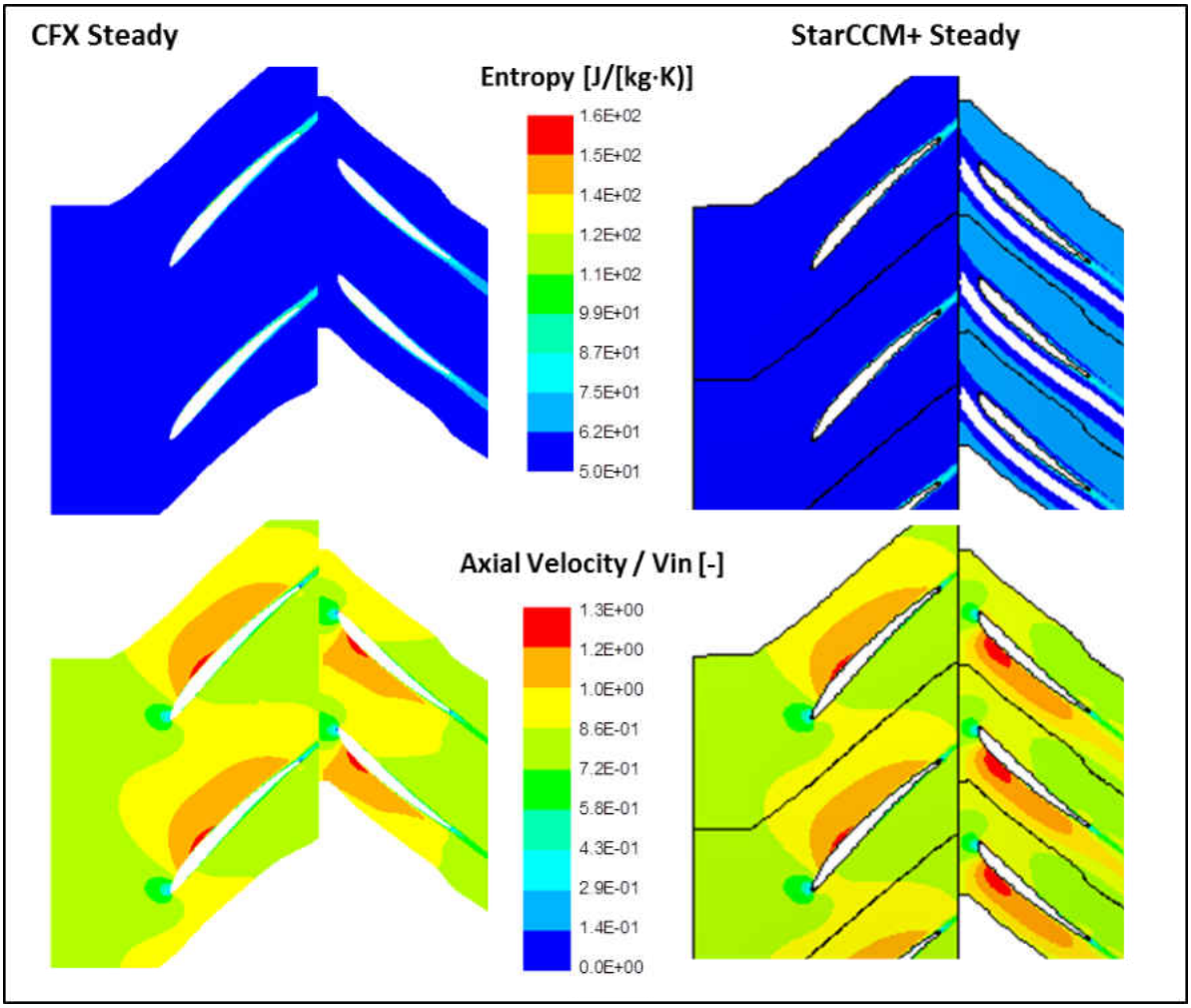

Figure 4.7: Steady Entropy and Axial Velocity: 50% span

Finally, the 98.5% span results are shown in Figure 4.8 and Figure 4.9. This span value was used in lieu of 90% because it was right below the blade tip, so it would better capture the phenomena sought. Again, very close agreement was observed at this span, which was a little pleasantly surprising. There were a few minor differences in the level of entropy, StarCMM+ being a little higher, but still very good agreement.

Because of its proximity to the tip, this location was examined in further detail as will be shown later.

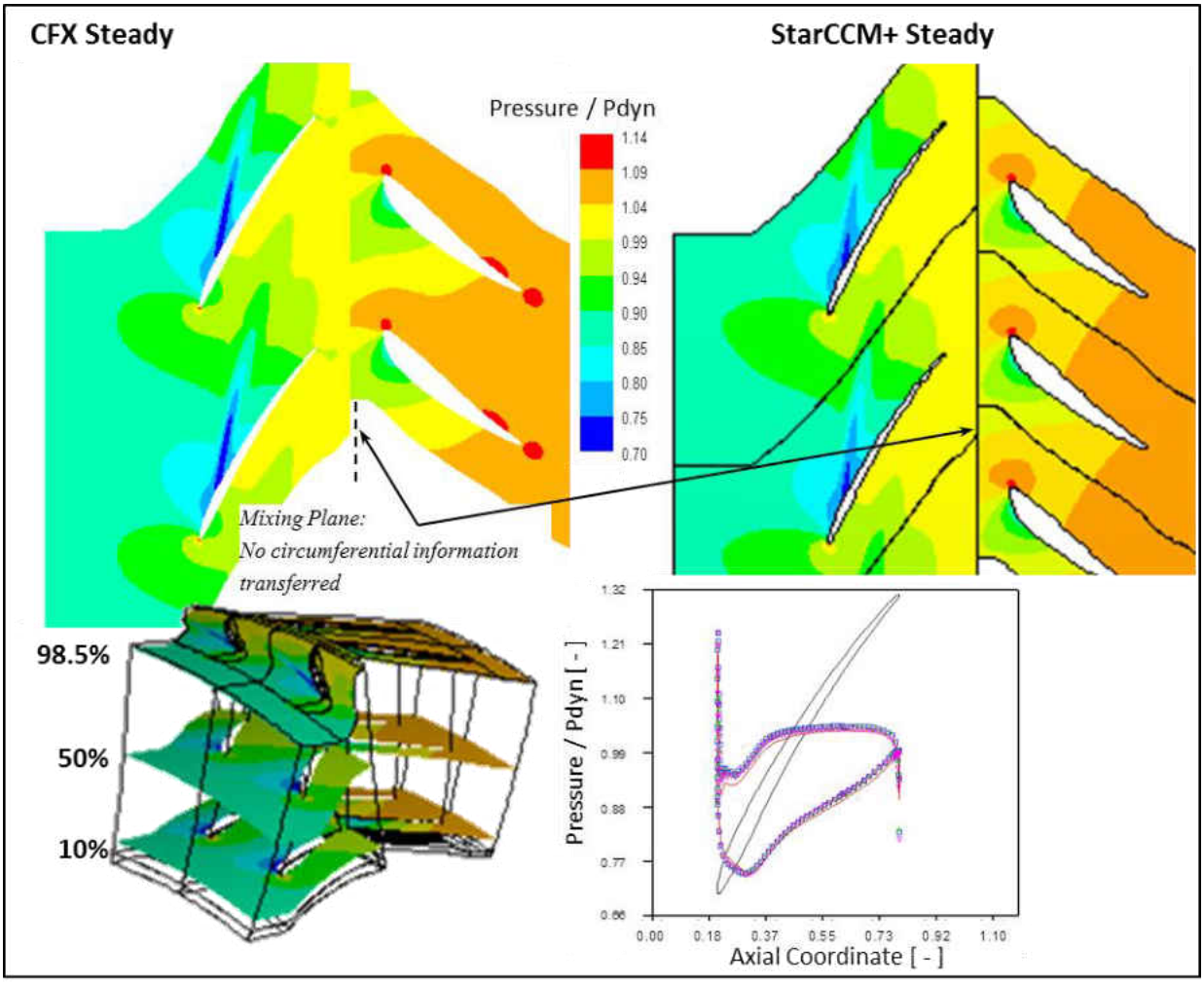

Figure 4.8: Steady Pressure: 98.5% span

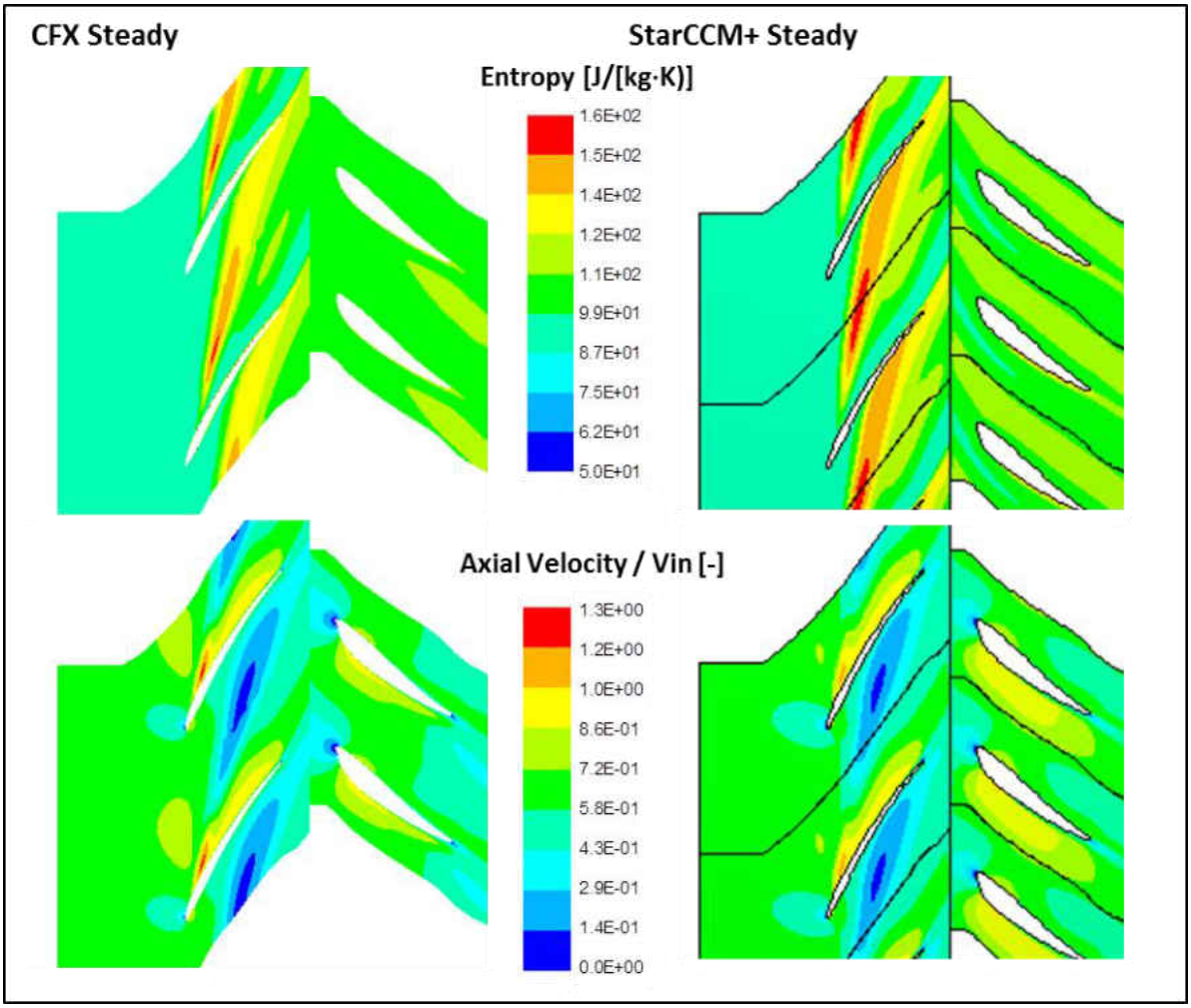

Figure 4.9: Steady Entropy and Axial Velocity: 98.5% span

A final comparison of the steady solutions was made by taking a plane perpendicular to the flow (S3 plane) at ~30% chord. A plot of entropy showed that across the span, the majority of the blade was at a lower entropy level in the center than the end walls for both solvers. This was the expected, and well known losses generated

by the end wall boundary layers. Near the OD, the region around the tip vortex was clearly defined with a higher entropy level, see Figure 4.10.

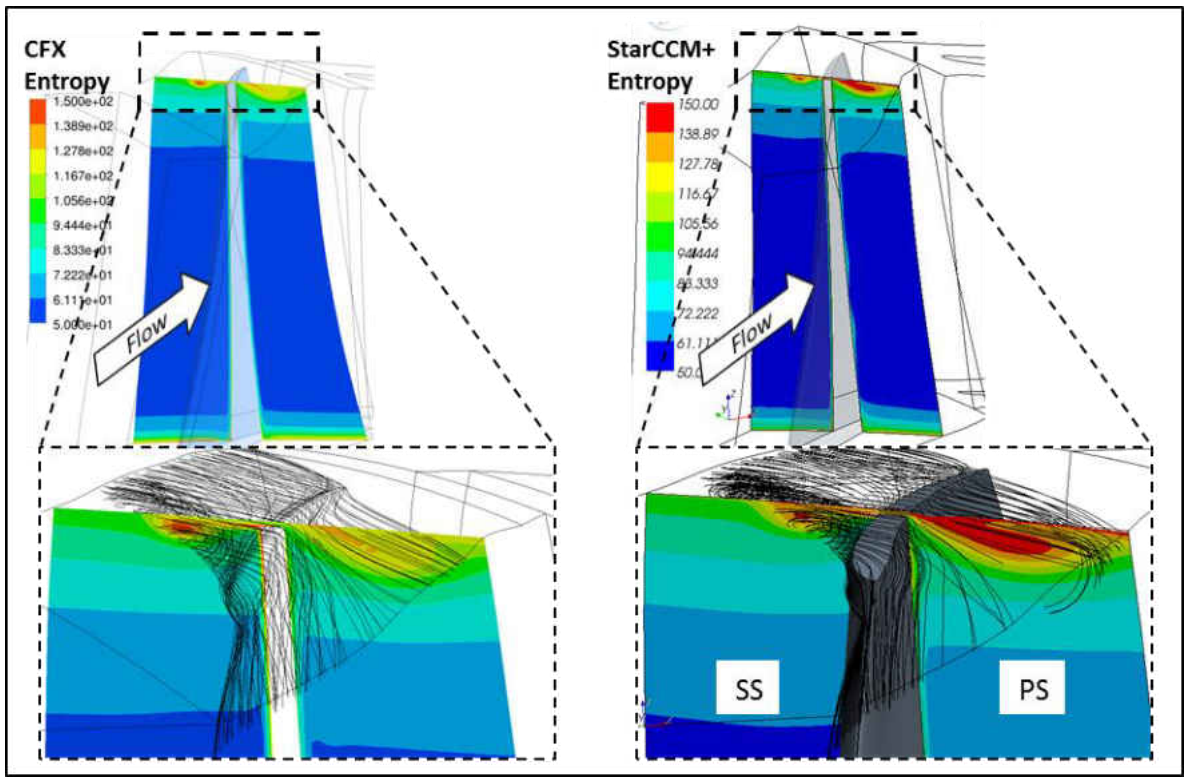

Figure 4.10: Steady Entropy at 30% Chord

The only difference between the two solutions was that StarCCM+ showed a little higher entropy in the tip vortex than CFX on the pressure side. This difference in the vortex intensity was not large in the steady solution, but became more significant in the unsteady flow, as will be shown.

The preceding figures confirm that the constant gap steady solution in StarCCM+ was in very good agreement to the trusted CFX steady solution. This was important in order to provide more confidence in the subsequent unsteady calculations in StarCCM+.

4.3 Constant Gap: Unsteady Solution

For the unsteady solution with a constant gap, a comparison between LinearTrace vs. StarCCM+'s harmonic balance solver was also a comparison between the time linearized vs. harmonic balance approaches. Since for the HB case the gap variation had not been turned on yet, this was as close to a back-to-back comparison as could be made between the two methods.

Before looking at the unsteady pressures, a quick check was made of the steady component of the HB solution (the zeroth term), which is equivalent to a time-averaged solution in a time-accurate solver. Figure 4.11 through Figure 4.13 show the steady pressure contours at 10, 50 and 98.5% spans. In each figure there are three pictures:

a) StarCCM+ HB zeroth term (*w0* term in Eq. 1.16)
b) StarCCM+ HB Physical Time=0 (entire Eq. 1.16 at t=0 [sec]). This is not really a "steady" plot, but rather a "snapshot in time"; however, it serves as a good reference to illustrate some of the differences in the unsteady solution.
c) Line plots of these 2 solutions (scatter points), plus the steady CFX case (solid line) for reference.

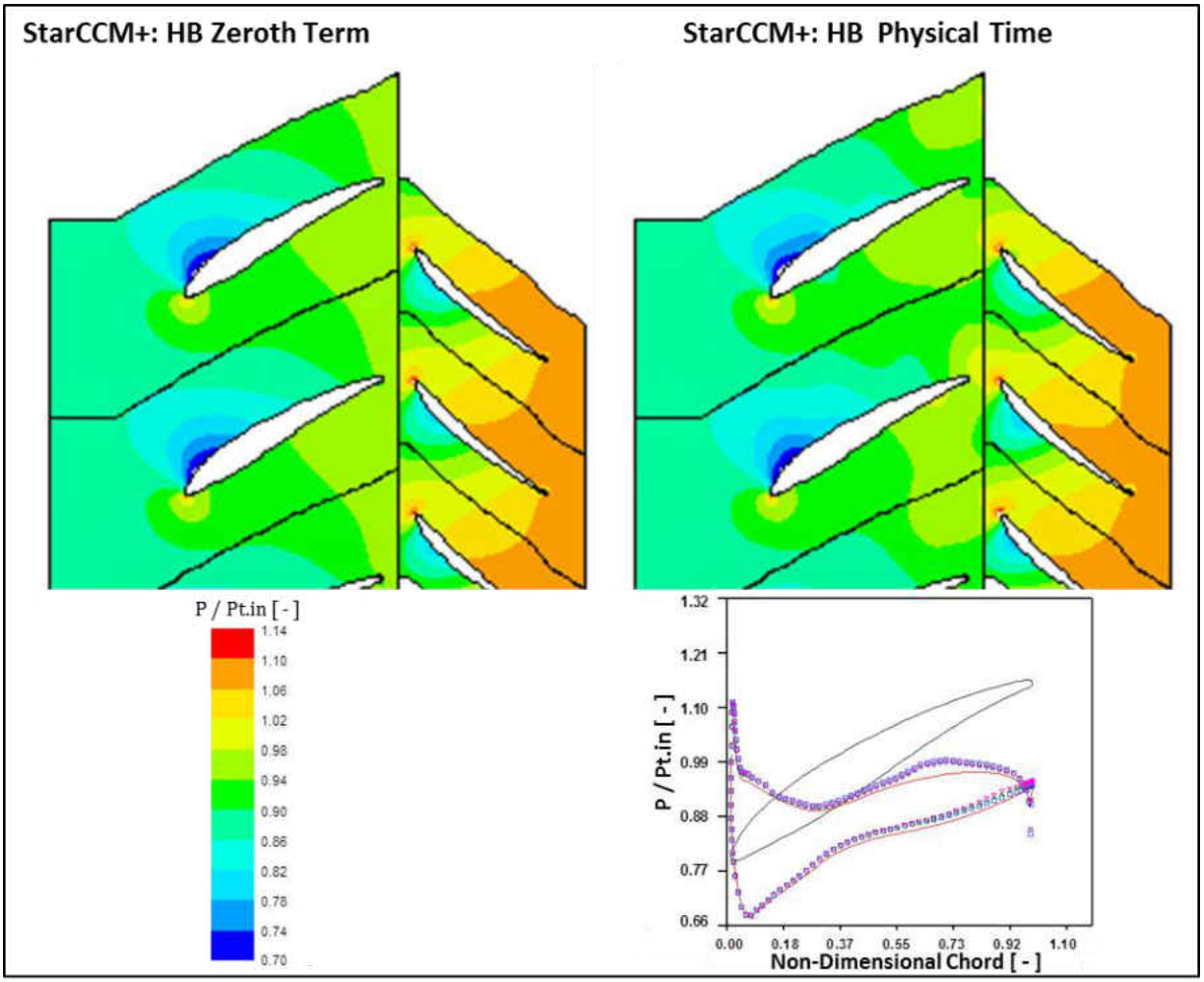

Figure 4.11: HB Fundamental Mode: Steady Pressure: 10% Span

At this span, there were small differences in the middle of the rotor passage near the trailing edge. The stator passage also showed small differences in the middle of the passage. However, the most notable new piece of information provided by these steady components of the unsteady solution was the upstream propagation of the potential field emanating from the stator leading edge. In the physical time solution there was a circumferential variation most clearly seen in the region between the rotor trailing edge

and the stator leading edge. In the zeroth term solution, this effect appeared to be averaged somewhat, so there was a clear step change at the rotor/stator interface plane. Just to clarify, both of these plots came from the same solution, but are just two different ways of post processing the results.

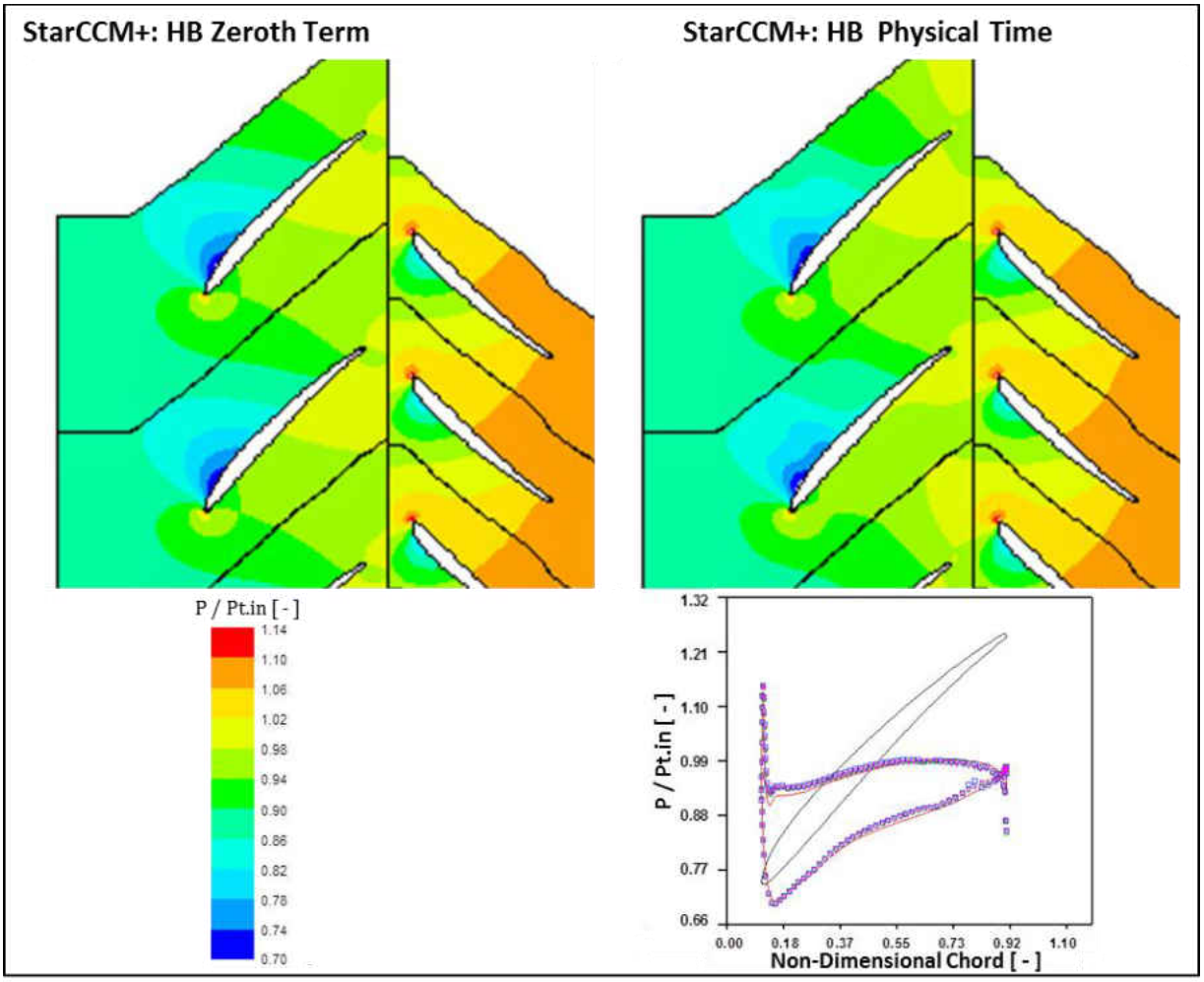

Figure 4.12: HB Fundamental Mode: Steady Pressure: 50% Span

At the 50% and 98.5% spans, the two steady solutions were again similar, with the same differences shown at 10%. They were also very close to the CFX steady solution, as demonstrated by the line plots.

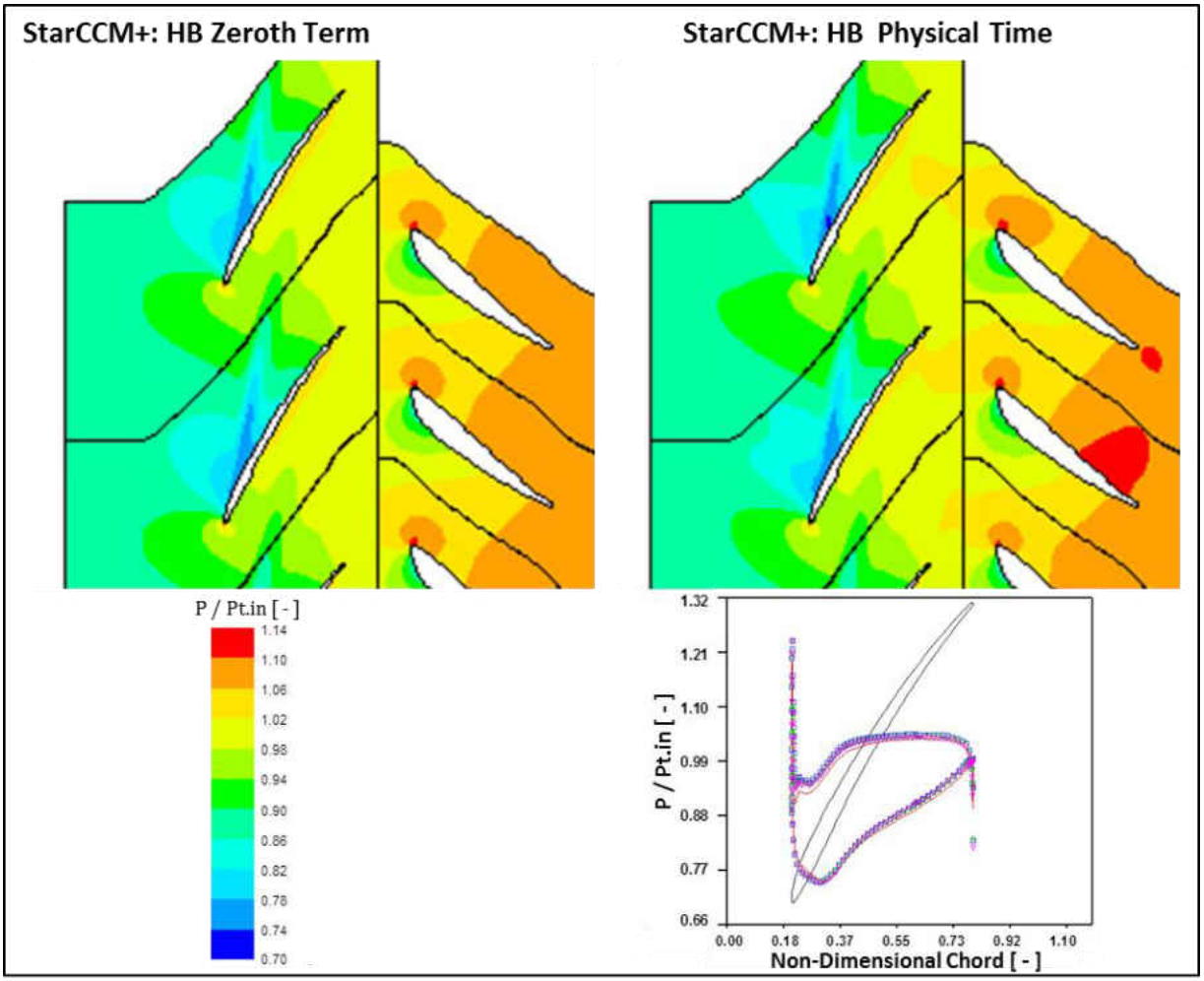

Figure 4.13: HB Fundamental Mode: Steady Pressure: 98.5% Span

The preceding plots showed that although the 4 steady solutions available at this point (CFX, StarCCM+ steady, StarCCM+ HB zeroth term and StarCCM+ HB physical time) were very close to each other, some new information was already provided by the harmonic balance solver. The circumferential variation at the interface plane provided by the HB solver was a consequence of the Fourier decomposition performed at this plane. This is what allows frequency domain solvers to model a full wheel with just a single passage, and a major deviation from the standard mixing plane assumption of steady solvers. This is of course necessary in order to capture the excitation from the downstream stator bow wave, as has been shown. The remainder of the flow field showed some smaller differences, which were also reflected in the blade loading. However, these were again in the order of the accuracy of the calculation (< 2%).

So far, only the “steady” flow (u_o) has been compared. Now, similar comparisons of the unsteady perturbation quantities ($\tilde{u}$) will be presented at the same locations. The unsteady pressure was compared between the unsteady baseline (LinearTrace) and the HB solution, both still with a constant gap. For the sake of brevity, only the real component of the unsteady pressure is shown.

At the first span location, Figure 4.14 shows very close agreement between the linearized and HB approaches. In both solvers, the only source of unsteadiness was the downstream stator bow wave. This can be seen entering the rotor domain, at the rotor-stator interface, as the peak (red and blue) pressure perturbations. Through the passage, both the magnitude and phase agreed well, which was also reflected in the blade loading shown in Figure 4.15.

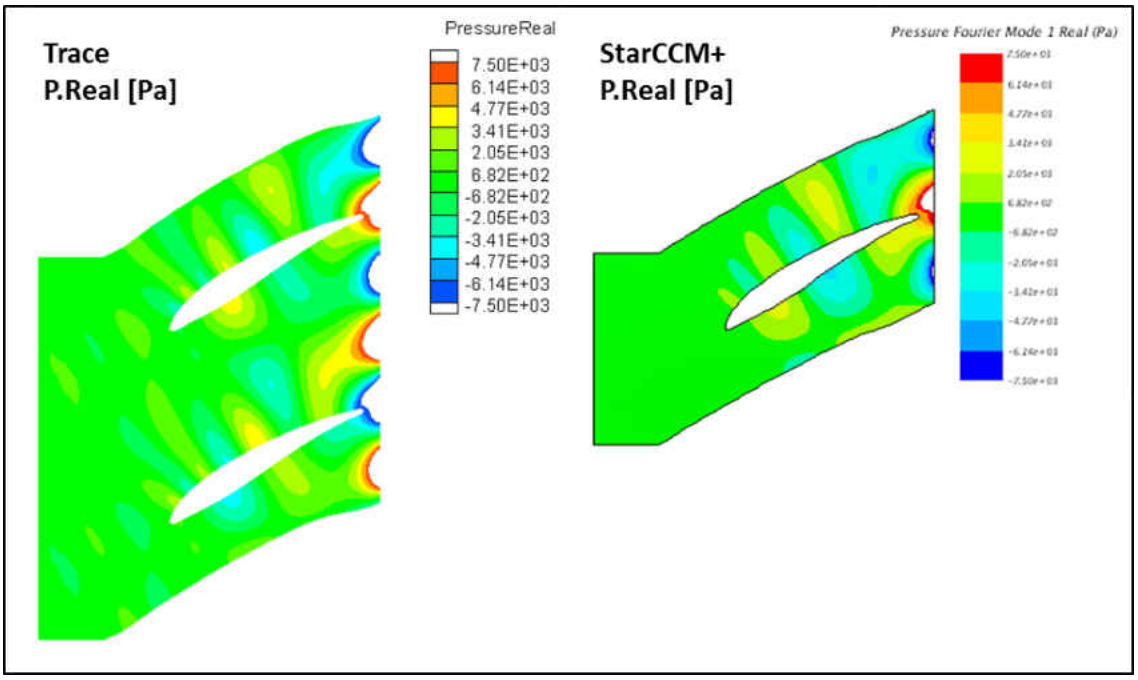

Figure 4.14: Constant Gap: Unsteady Pressure at 10% Span

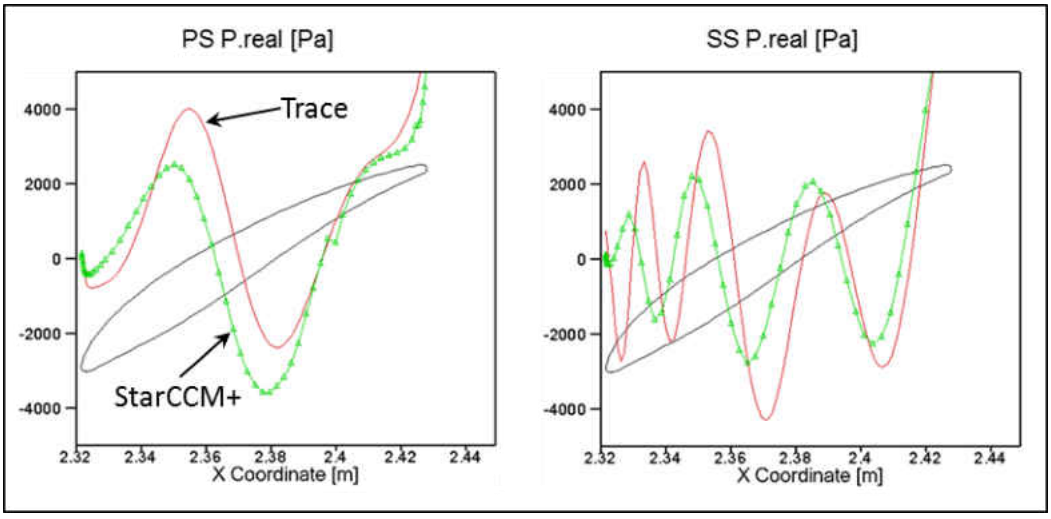

Figure 4.15: Constant Gap: Unsteady Loading at 10% Span

At the mid-span, Figure 4.16, the story began to change a little bit. LinearTrace showed a stronger perturbation entering the rotor passage, which impacted the PS trailing edge.

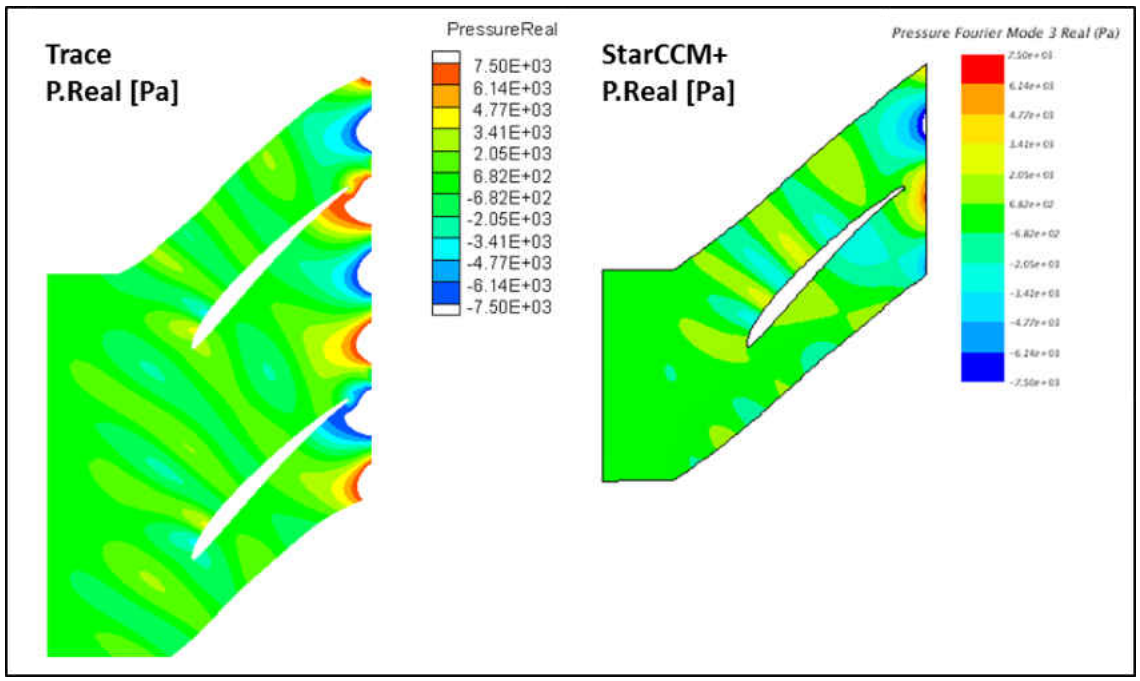

Figure 4.16: Constant Gap: Unsteady Pressure at 50% Span

Along the surface of the blade, Figure 4.17, this was flipped. Here, the HB solution showed a little stronger amplitude on the SS. On the pressure side, Trace did predict a much stronger amplitude near the trailing edge (as in the contour). For both PS and SS, the two solutions were still relatively in phase with each other, although some differences began to emerge.

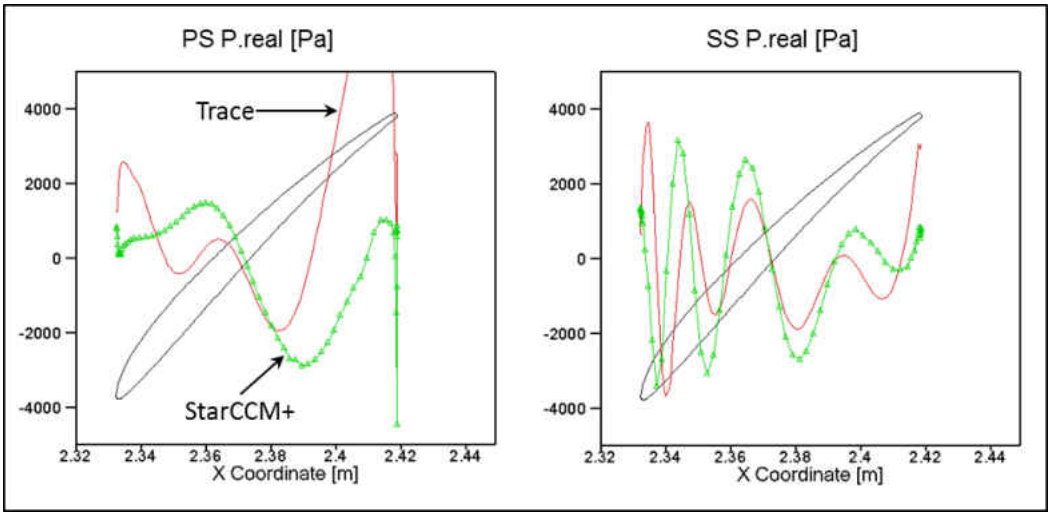

Figure 4.17: Constant Gap: Unsteady Loading at 50% Span

At the highest span, the trends were somewhat similar to the middle. LinearTrace predicted a stronger perturbation coming in, and this showed up on the entire chord. Overall, the loading showed relatively good agreement in phase for the SS, but the PS had a clear phase shift.

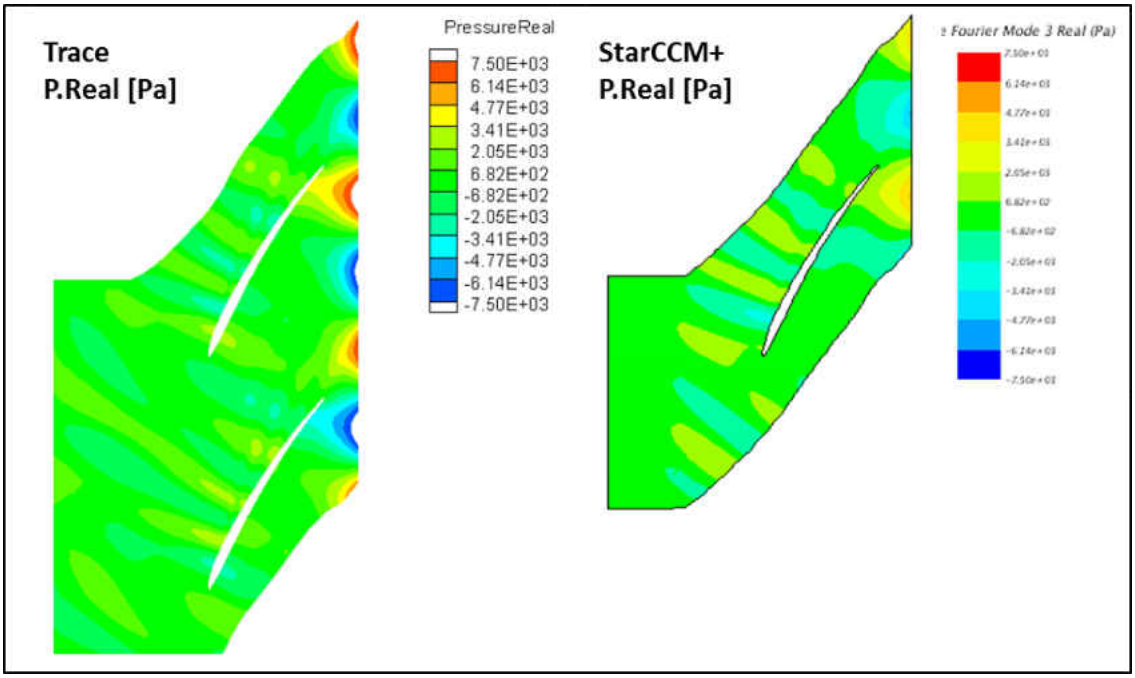

Figure 4.18: Constant Gap: Unsteady Pressure at 98.5% Span

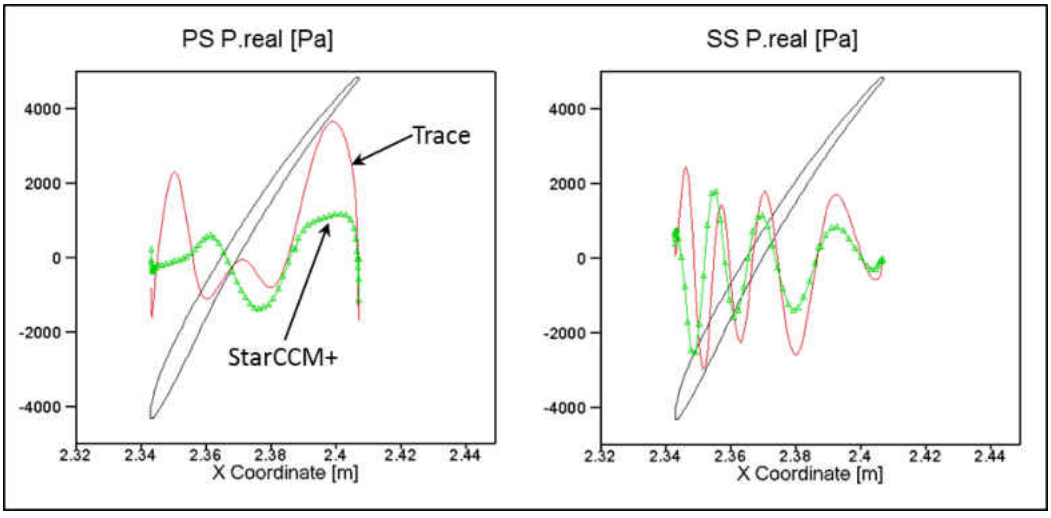

Figure 4.19: Constant Gap: Unsteady Loading at 98.5% Span

Although these two solutions were in relatively good agreement from a cursory look, there were some significant differences. This was the expectation, overall general agreement in trends and ballpark levels, but clear deviations when looking at the details.

The similarities in the unsteady solutions without gap variation gave a good level of confidence on the accuracy of the HB solution. At the same time, the differences underscored the sensitivity of the unsteady solution to the two approaches. This was expected because they are two fundamentally different unsteady solvers. The next step was to look at the gap variation.

4.4 Varying Gap: Steady Solution

The gap variation implemented in the single passage model was prescribed in chapter 3.3.1. However, as was mentioned earlier, a half wheel model was initially created and a steady solution obtained. This model had a gap variation built in, so it will be discussed at this point, followed by the equivalent solution using the single passage model.

4.4.1 Half Wheel Model

For the half wheel model, the rotor-stator interface implemented a mixing plane BC, so no circumferential variation was passed from the stator. Figure 4.20 shows this compared to the equivalent StarCCM+ steady single passage solution. The plot only

shows a few of the 24 passages, but they all had a similar behavior at this 50% span, as expected.

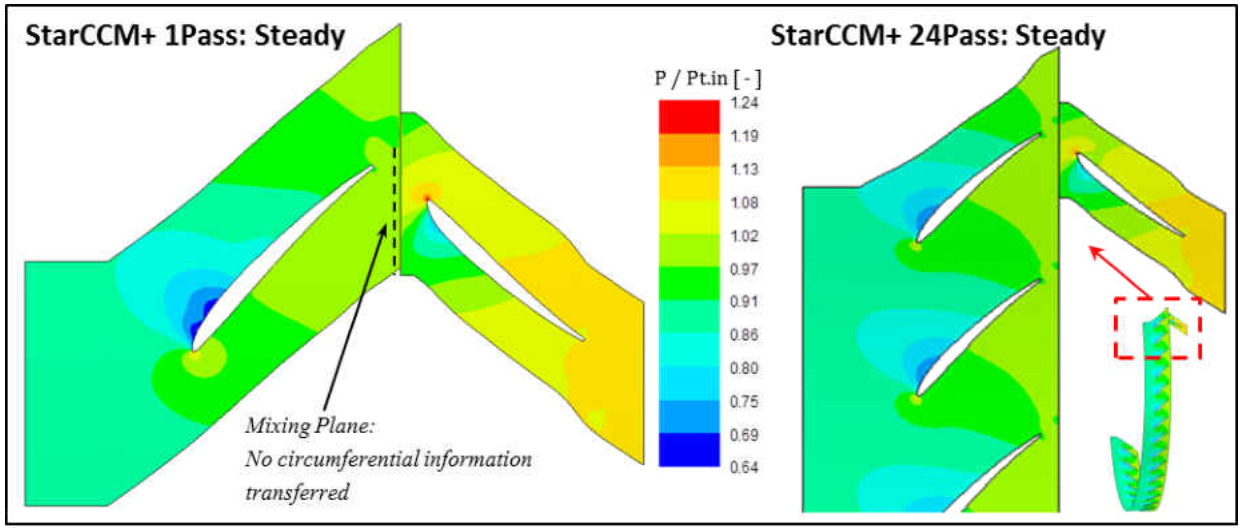

Figure 4.20: Varying Gap: Steady Pressure: Half Wheel

The corresponding loading at 50% span is shown in Figure 4.21. A comparison is made against the CFX steady solution (solid line), as previously done. For most of the airfoil, the CFX and StarCCM+ solutions were mostly similar, except in two regions. The first was in the front 20% chord, where the StarCCM+ solution predicted a slightly lower pressure. The second region was on the PS, in the aft portion of the blade. Here, the scatter points showed a clearly noticeable variation between passages. Since this 180^{o} model had the same mixing plane boundary condition on all passages, then the only source of variation was a different gap at each passage. This variation made sense in

that it only affected the aft portion of the PS. As the tip vortex crossed over the gap, it impinged on the aft region of the PS of the adjacent blade, as was shown in Figure 4.9. The fact that this effect, generated at the tip, could be felt near the mid-span was not expected. Mailach [77] reported that the blockage generated by the tip leakage flow diverted the flow toward the hub. This was seen especially at the rotor exit plane; however, this effect was reported to remain above ~80% span. In the present analysis this behavior is also present, but here it appears stronger. The remainder of the airfoil (along the chord), at this mid-span, showed no significant differences between passages.

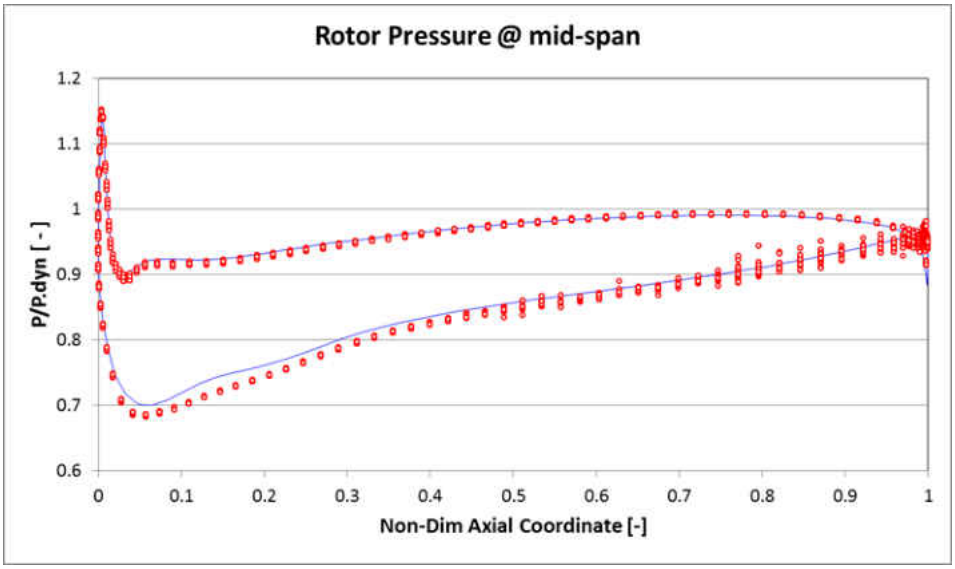

Figure 4.21: Varying Gap: Steady Loading 50% Span

A similar plot at 98.5% span showed much greater differences in the 180^{o} model across the different passages, as shown in Figure 4.22

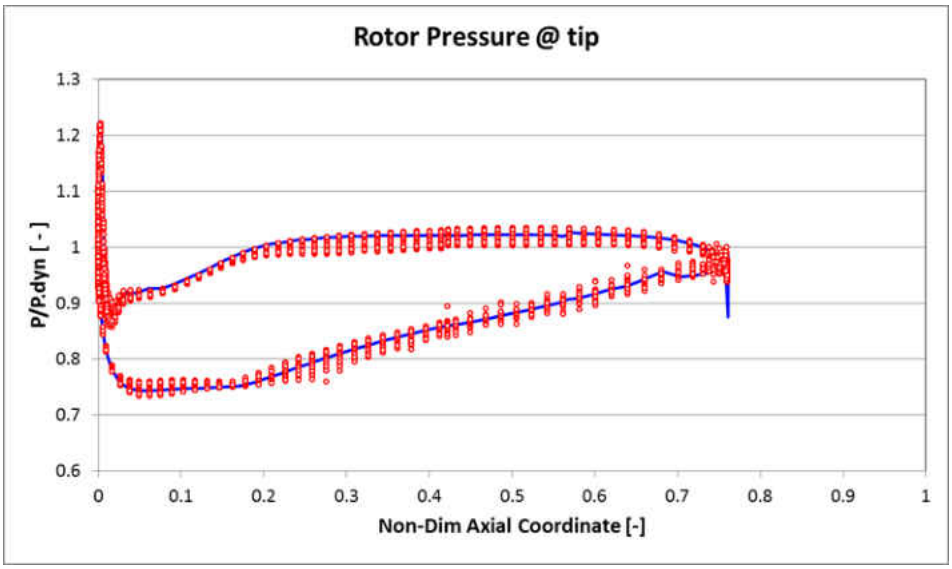

Figure 4.22: Varying Gap: Steady Loading 98.5% Span

This tip loading showed the expected trend, although the actual amplitude of the variation (~2.5%) was not really anticipated. This model was from the initial trial runs, so it was not post-process in detail. The reason to report on it here is to show some qualitative trends and differences that are still valuable, such as this tip loading.

When looking at the entropy at 30% chord in Figure 4.23, the differences between passages were better observed. The two passages shown corresponded to the smallest and largest gaps; 25% gap (left), and 175% gap (right). So these plots bounded the entropy variation from the 24 passages. As expected, the entropy field was very similar between the two passages for most of the blade except near the tip. Here, it was

evident that the stronger circulation in the larger gap generated more losses. In the smaller gap, the vortices were much weaker and generated a much smaller entropy field. In fact it was hard to distinguish the entropy from the boundary layer on the casing wall and the entropy form the tip vortex of the smaller gap.

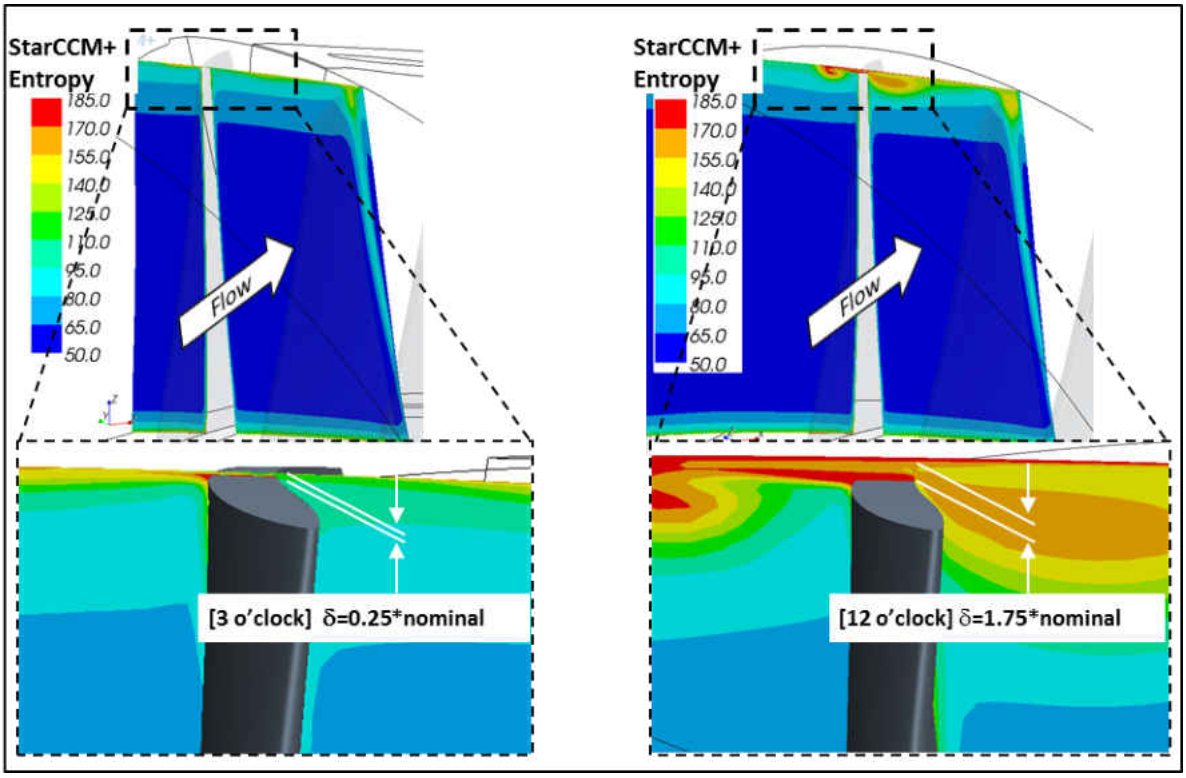

Figure 4.23: Steady Entropy: Half Wheel: 30% Chord

This half wheel model could not be run in unsteady mode (harmonic balance), due to convergence issues. It may have been a simple matter of further tuning the different settings to get it to converge. However, this was not attempted because it would not have captured the effect of the gap changing for any one particular blade. Instead each

blade had constant gap, albeit different from its neighbor. So the work per cycle for any particular blade would not really capture the gap variation sought.

4.5 Varying Gap: Unsteady Solution

After both the steady and unsteady solutions with a constant gap were satisfactorily compared against a trusted baseline, the gap variation was turned on. As mentioned earlier, the HB solver provided a steady component in the zeroth harmonic (discussed in chapter 4.3) and the unsteady perturbation quantities in the higher harmonics. For the unsteady case with a constant gap, there was only one harmonic of interest, the rotor passing frequency. Actually, from the rotor frame of reference, it was the stator passing frequency, a 72/rev occurrence. Now that the gap variation was activated, there were two harmonics of interest. The first one was the stator passing as before; the second harmonic was due to the gap variation. This was defined to occur at twice the engine rotation in order to form the ideal ovalization previously shown.

As a first check that the ovalization was generated as intended, the grid displacement was plotted as a function of time step. Figure 4.24 shows the results of the grid deformation at the tip gap provided by the solution. Here, the abscissa (horizontal axis) shows the circumferential location, which was derived from the "physical time" and the speed of rotation. The ordinate (vertical axis) has the gap (δ) normalized by the nominal value.

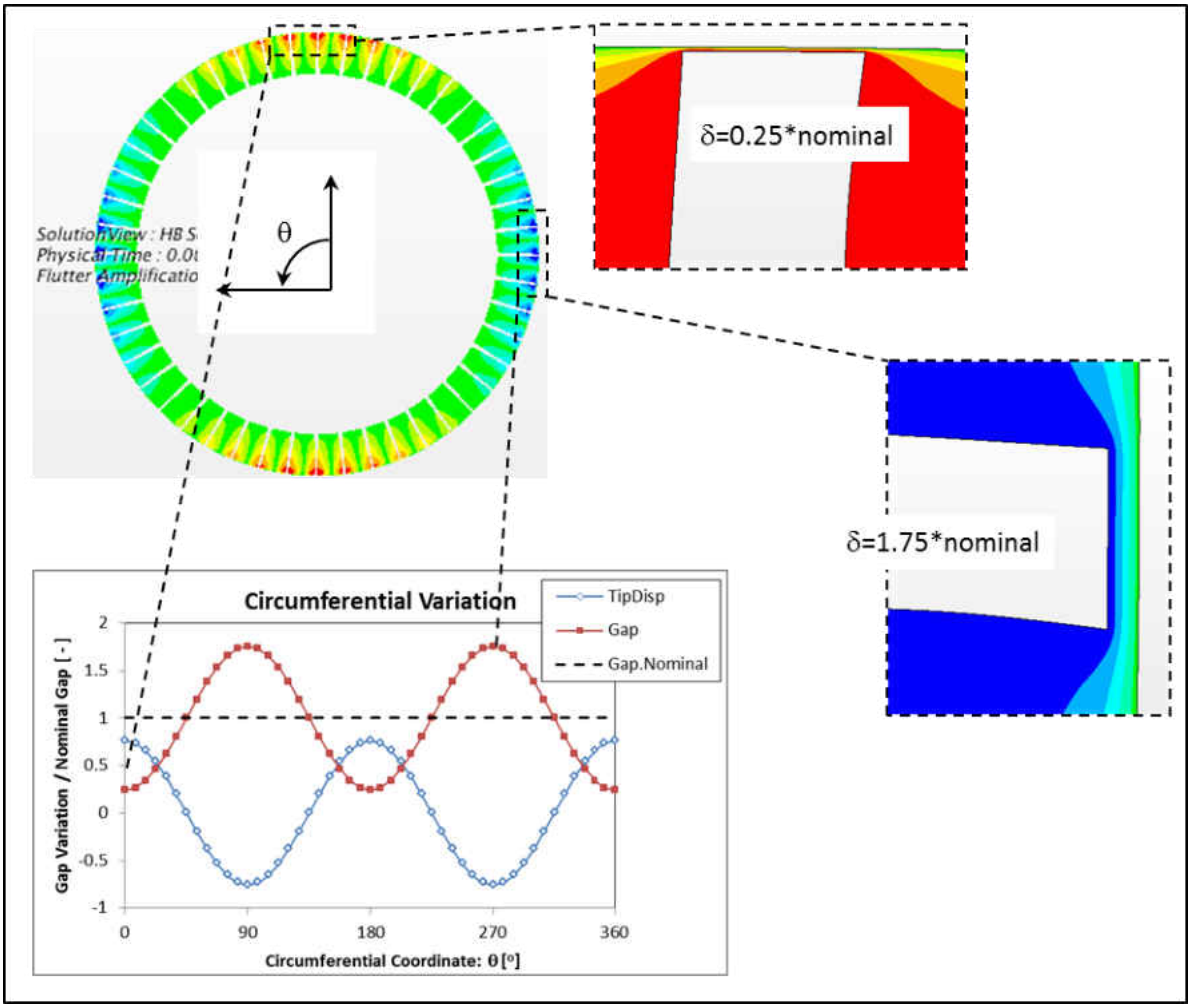

Figure 4.24: Circumferential Gap Variation: Results

The plot shows a trace across the circumferential coordinate for the maximum deflection at the blade tip. The HB solution was interrogated at time intervals of 1/48 [sec], so there was essentially one point per airfoil. The displacement went through two cycles with the maxima at 0^{o} and 180^{o} and the minima at 90^{o} and 270^{o}. This created the minimum gap at the vertical plane and the maximum at the horizontal. Of course this

is an arbitrary definition, which could have been rotated based on the definition of θ. The points where the gap crossed the dashed line corresponded to the passages equal to the nominal, which occurred every 45^{o}. Finally, it is obvious (but still worth pointing out) that this plot illustrates the harmonic content of the gap variation. It confirmed that the defined forcing function from the tip gap variation was indeed a 2/rev excitation, as specified.

4.5.1 Amplitude Variation ± 75%

The first model attempted had the amplitude of the gap variation at ±75% of the nominal, as was shown in Figure 4.24; this was the largest variation attempted. It was chosen as the first point to run because it was the most demanding in terms of the grid deformation. The larger mesh morphing had a larger likelihood of generating negative cells, so running this case successfully almost guaranteed that less severe gap variations could also be achieved. This was true not only for the grid deformation, but also in terms of convergence. This case was also anticipated to be the most useful because the effects of the largest variation were expected to come across more clearly than in cases with a lower deformation.

The effect of the gap variation can be seen from a direct comparison of the constant gap vs. gap variation in StarCCM+. A direct comparison to LinearTrace was not possible since LinearTrace was only run with a constant gap. The first basic comparison was of the unsteady pressure distribution (real component of the pressure perturbation) at the same 3 span heights shown before; see Figure 4.25 through Figure

4.27. The figures show contours of the constant vs. varying gap on the left, and the corresponding line plots on the right. For the line plots, the solid lines represent the LinearTrace solution (constant gap), shown just for reference, the green symbols are the StarCCM+ constant gap, and the magenta symbols are the StarCCM+ varying gap (±75% variation).

The first figure, at 10% span, had a relatively good agreement between the constant gap and varying gap. This was expected since the effect of the tip vortex has been shown to dominate the upper spans, Mailach [77]. The only meaningful difference was on the pressure side (PS) trailing edge (TE). Otherwise, the two solutions were in close agreement both in magnitude and phase.

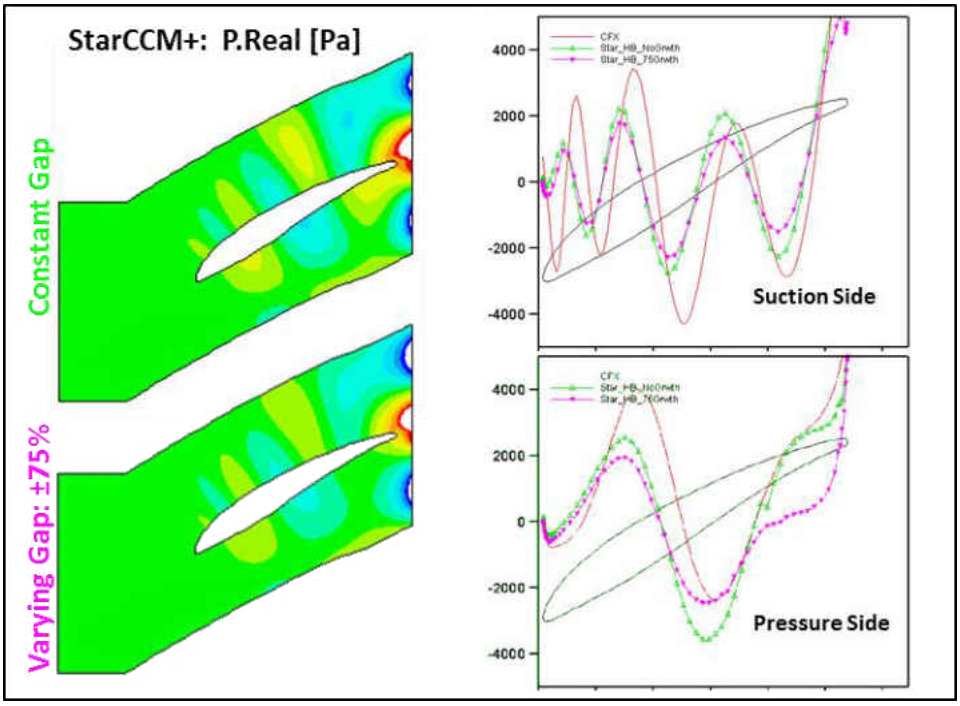

Figure 4.25: Constant vs. Varying Gap: Unsteady Pressure at 10% Span

At the 50% span, already some differences showed up due to the gap variation. In Figure 4.26, the suction side (SS) was in phase between the constant gap and varying gap, but the latter showed smaller amplitudes in most of the front part of the blade. On the PS, there was a much bigger difference, although the character of the curves was still similar between the two solutions. This was the first significant difference observed for the varying gap, and if followed the trend of the unsteady pressures from the constant gap solutions.

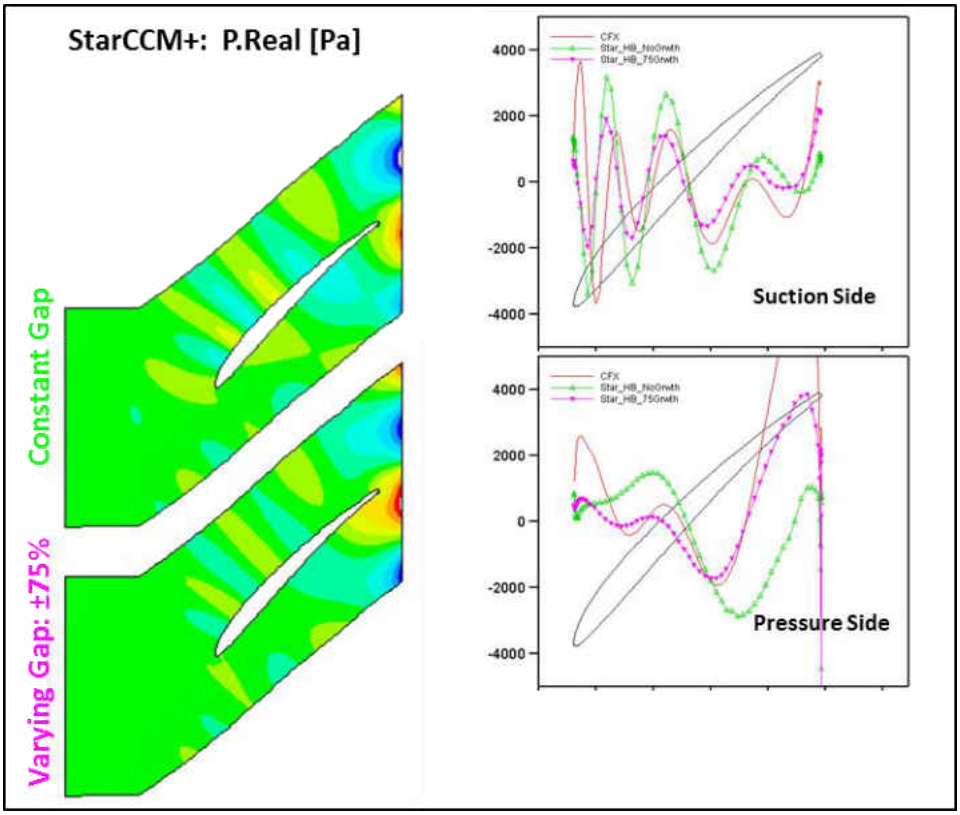

Figure 4.26: Constant vs. Varying Gap: Unsteady Pressure at 50% Span

Moving to the highest span (98.5%), the SS again seemed to be in relatively close agreement between the two solutions, while the PS was not only off on amplitude again, but now there was a phase shift of roughly one half of the period in the front part of the airfoil. This was again following the trend from the constant gap unsteady solutions.

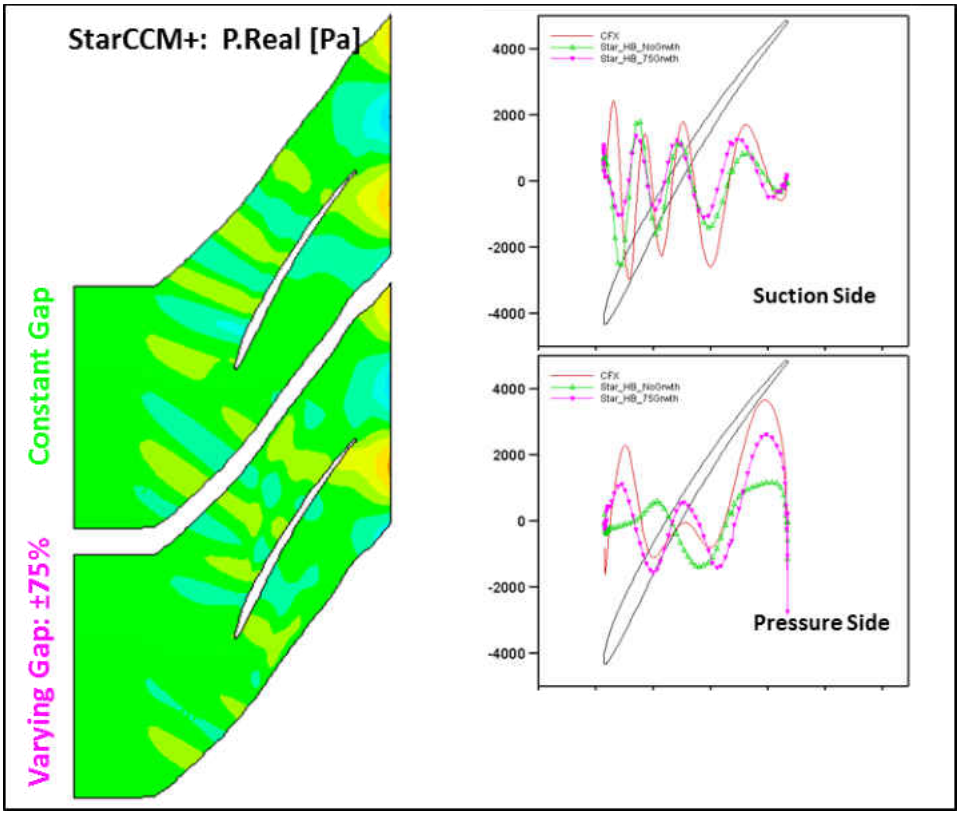

Figure 4.27: Constant vs. Varying Gap: Unsteady Pressure at 98.5% Span

These blade-to-blade plots already began to show the effect of the circumferential gap variation. However, a better visualization of the tip clearance vortex (TCV) was provided by the Q-criterion. In order to calculate this for the HB unsteady results,

several instantaneous solutions were selected. The points of interest were for θ values of 0, 49, 82 and 131 degrees in Figure 4.24. Location $\theta=0$ corresponded to when the gap reached 25% of nominal, so this was the tightest gap in the solution. For $\theta=82$, the gap was at the widest point (175% of nominal). Finally, points $\theta=49$ and $\theta=131$ were the ~nominal gap value.

Figure 4.28 shows the tip vortex evolution as the gap varied for these reference points.

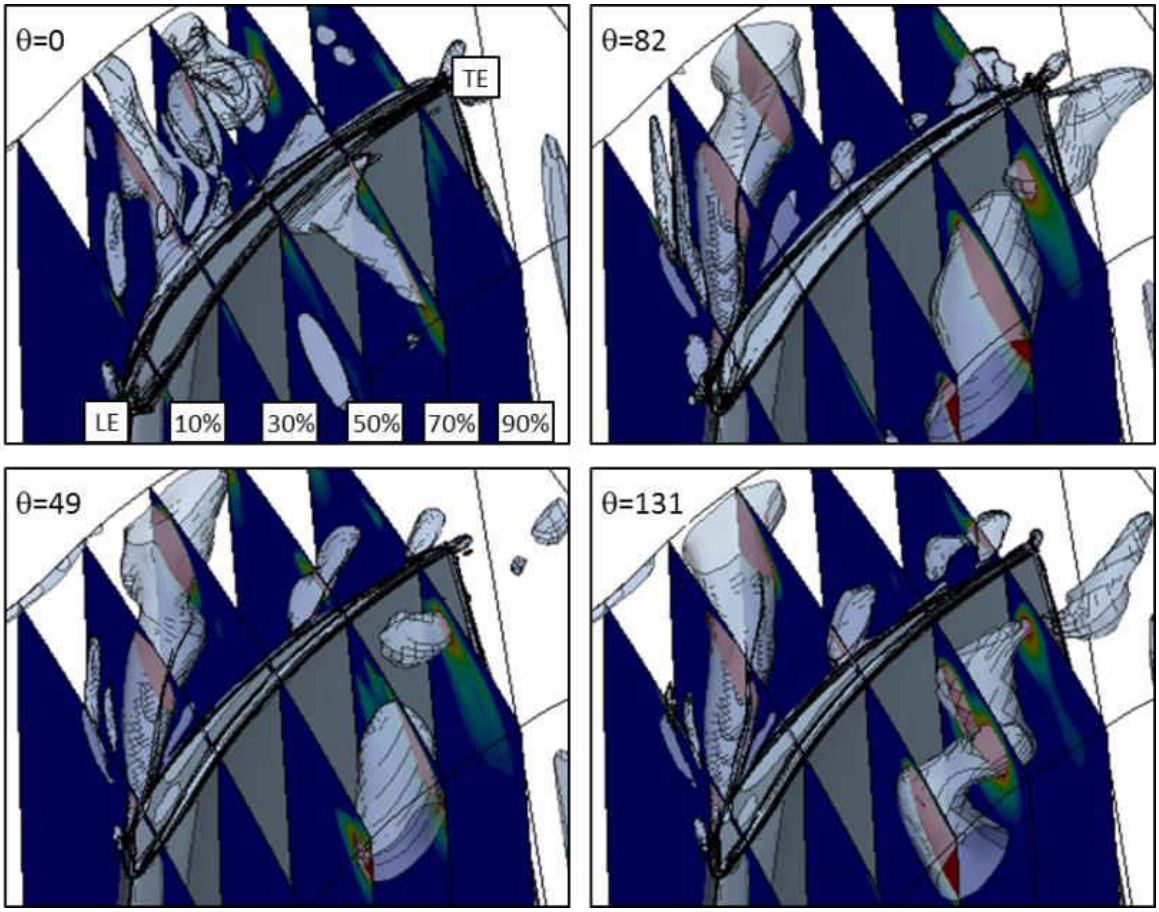

Figure 4.28: Tip Vortex Evolution

For the small gap (θ=*0*), the vortex was not well organized, so the core ended up looking a little 'dirty'. There was still an identifiable core emanating from the tip gap, but it got quickly mixed in with the larger momentum axial flow inside the passage. For the largest gap (θ=*82*), the tip clearance vortex was well formed and got much closer to the pressure side of the adjacent passage (as it crossed the periodic wall). In this case, the vortex barely missed the TE as it exited the passage. This is the likely source for the differences seen on the PS loadings previously shown. The other two points, corresponding to the ~nominal gap position (θ=*49* and θ=*131*), were similar, but not exactly. Aside from numerical noise, one might expect these to yield very close solutions, but the analysis showed that these points depended on whether the gap was opening or closing. When the gap was opening (θ=*49*), the vortex was starting to take shape, so the nominal gap vortex was still not well formed. Conversely, when the gap was closing (θ=*131*), the vortex was already well defined, so the nominal gap seemed a little stronger.

Corresponding contours of this Q-criterion for three circumferential locations (θ=*0, 49* and *82*) were also plotted for five axial positions (10, 30, 50, 70 and 90% of chord) in Figure 4.29

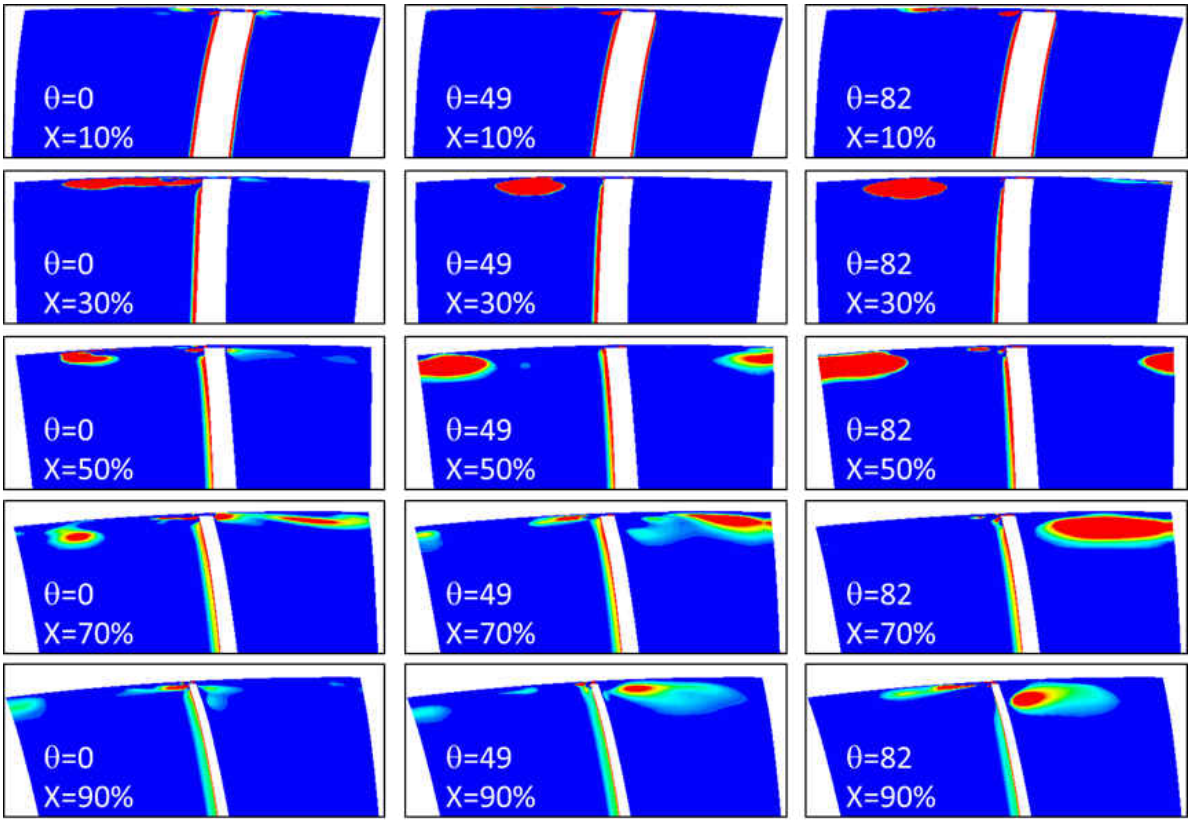

Figure 4.29: Q-criterion: ±75% Variation

The figure reiterates and clarifies the evolution of the vortex along the passage for different circumferential locations. Looking across the rows, it is evident how the vortex grows as the gap increases. This is best shown for *x=50%*, but also true for the other axial locations.

To complement the visualization of this tip vortex evolution, the entropy was plotted on a BB cut at 98.5% span over one half engine revolution (0^o to 180^o) see Figure 4.30 and Figure 4.31. From this sequence of snap shots there were a few additional points that became evident. First of all, the passage was copied over one pitch in each direction to illustrate how the solution varied (periodically) from one passage to the next,

as well as over time. The plots again showed that the vortex was smallest at the tightest gaps (θ=0° & 180°). At these two locations, the entropy again showed an unorganized vortex. It did not even impact the adjacent blade, but rather exited the passage and dissipated almost completely. This was in contrast to the largest gap (θ=90°), where there was a clear definition of the tip vortex, and it impacted the adjacent blade. Actually, the effect remained present at the exit of the domain, although with a lower intensity.

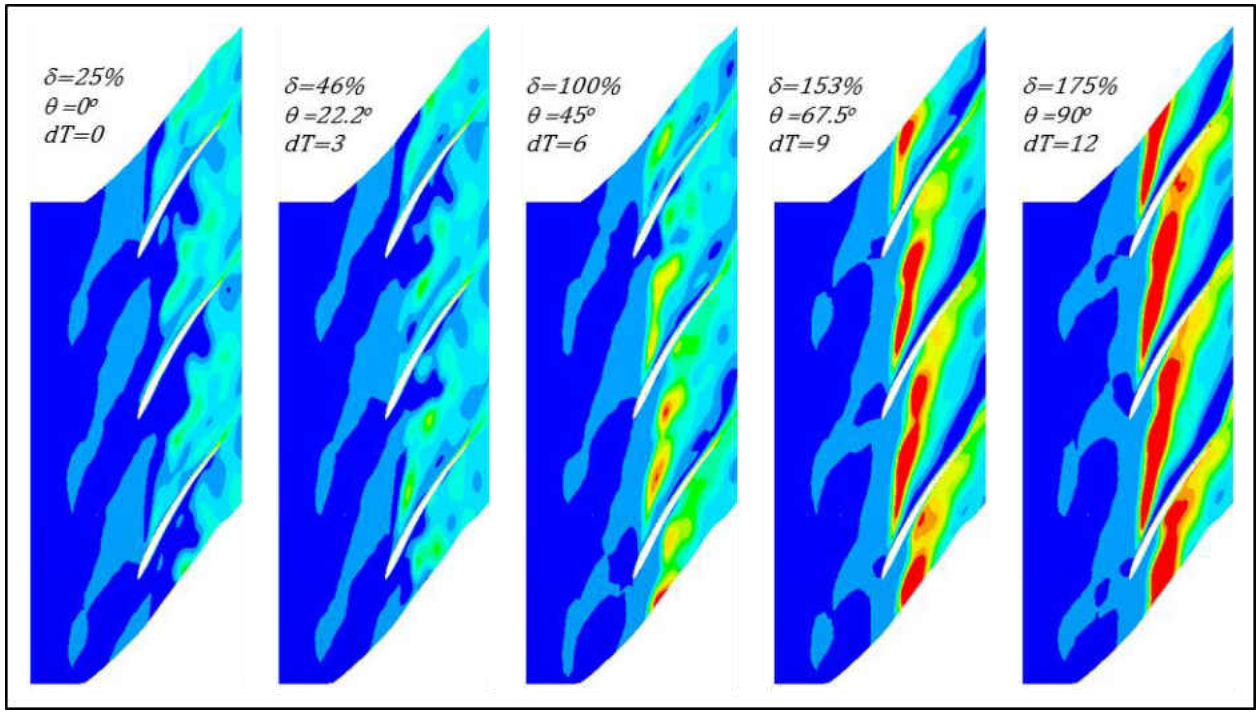

Figure 4.30: Tip Entropy: Gap Variation ±75%: BB 98.5: θ=0° → 90°

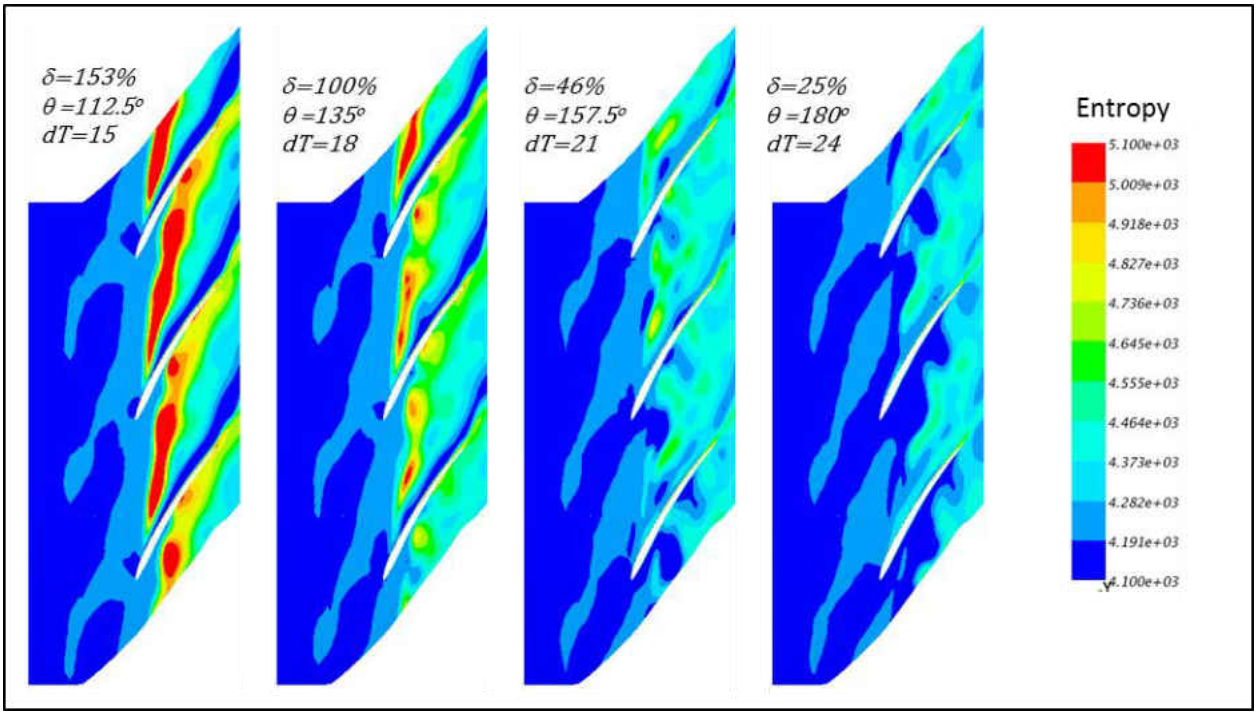

Figure 4.31: Tip Entropy: Gap Variation ±75%: BB 98.5%: θ=112.5° → 180°

The differences in the tip vortex as the gap varied made physical sense. The larger gap had a stronger vortex and generated more entropy, while the opposite was true when the tip gap was reduced. However, these plots did not show how this effect was transported half way down the blade, as suggested by the unsteady pressure BB contours at 50% span. Fortunately, this could be seen by unsteady velocity vectors on an S3 plane cut at 30% chord, see Figure 4.32. The suction side of the blade (left side) had a radial component that migrated downward from the tip until ~25% span. Although this radial component was relatively small (vector magnitudes were constant), it was still enough to carry part of the effect from the gap variation down the airfoil

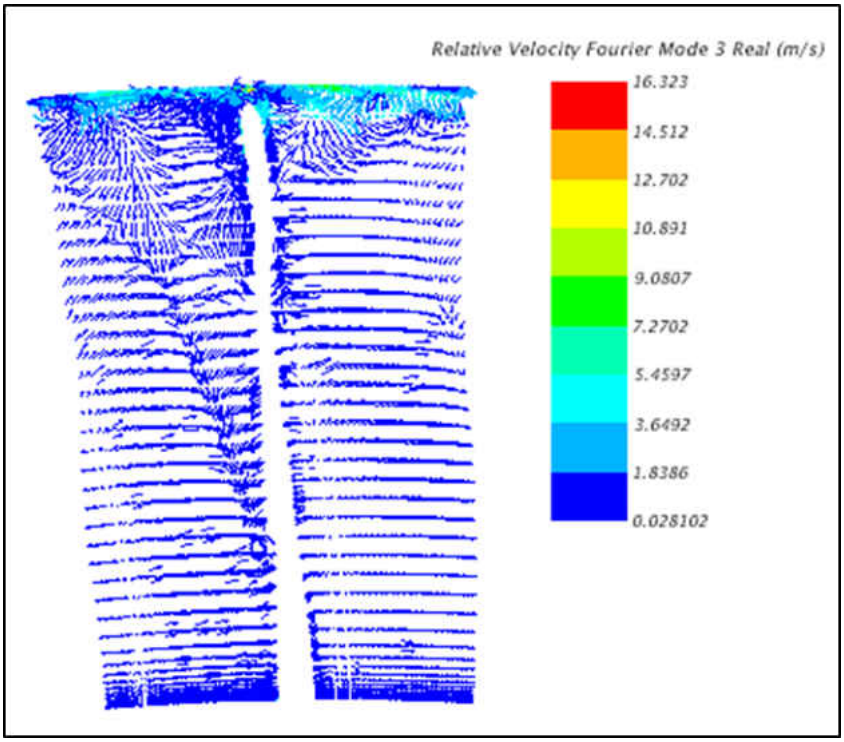

Figure 4.32: Axial Velocity Perturbation: 30% Chord

4.5.2 Amplitude Variation ± 5%

As previously mentioned, this analysis was repeated for several tip gap variations. However, only the ±5% will be further discussed in this section. Figure 4.33 shows the same sequence of entropy snap shots for this smaller gap variation on the exact same contour levels. As can be appreciated form the images, the pattern in the variation was very similar to the larger gap variation. However, the wake remained mostly unchanged as the gap opened and closed. Also, the vortex intensity was lower, and a little different

at the nominal position (δ=100%), where it was expected to be the same as in the ±75% gap variation nominal position.

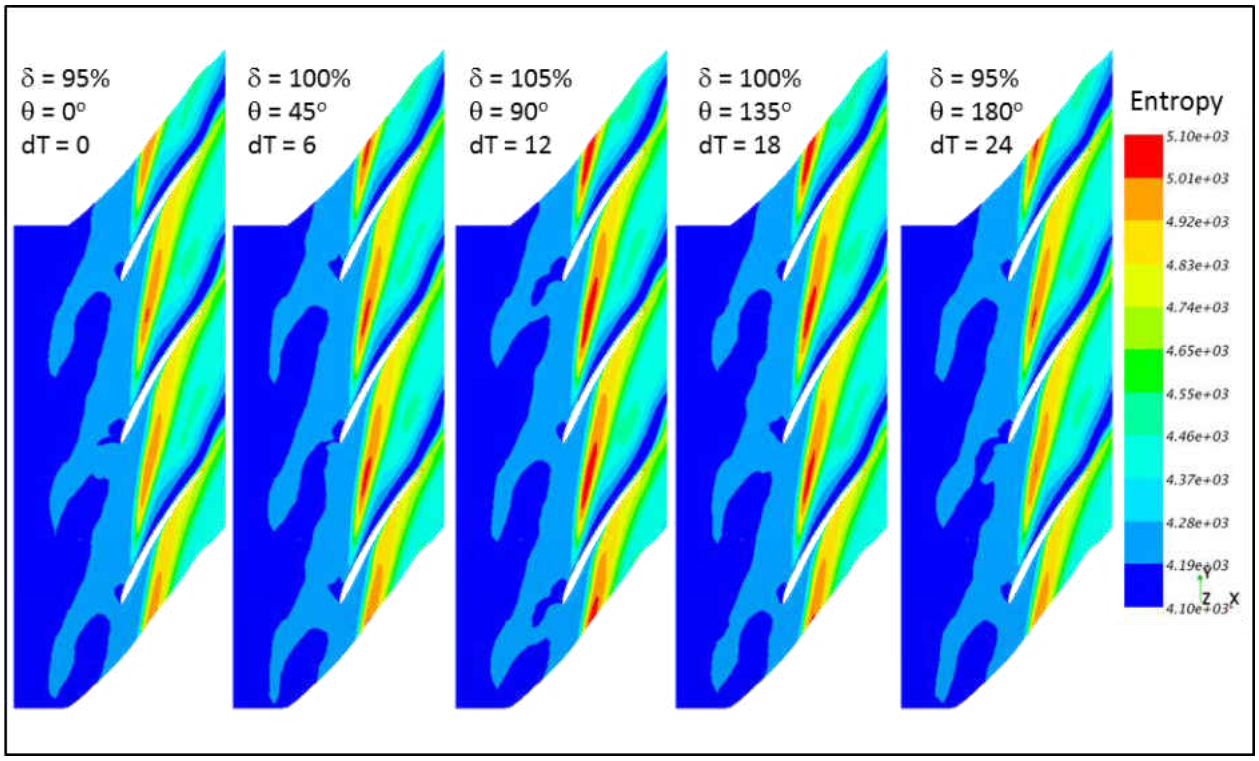

Figure 4.33: Tip Entropy: Gap Variation ±5%: BB 98.5%: θ=0° → 180°

In general, the tip vortex in the larger gap variation was much more unorganized and experienced an overall higher level of entropy than the lower variation. This small gap variation almost seemed as no variation at all, as seen in the steady solution (Figure 4.9).

4.6 Work Per Cycle

The work per cycle is presented in this section for both the constant gap and varying gap solutions. As mentioned earlier, this is a common way to quantify the aeroelastic impact on a blade, and was the figure of merit in the grid independence study shown in Figure 3.6. That figure only showed the work per cycle for the case where there was no gap variation, and directly compared it to the baseline (LinearTrace solution). It also showed that the harmonic balance (StarCCM+) solution predicted an unsteady work that was ~40% of the linearized (Trace) work. Although some differences were expected, this was larger than anticipated. However, Li [60] also showed discrepancies in the order ~3x (although in the opposite direction) between time linearized and harmonic balance solvers. Nevertheless, the importance of this quantity lies in the relative comparisons across models, not so much in absolute values.

Now that the gap variation was introduced into the analysis, the mesh sensitivity was again calculated for the case of ±75% variation. In Figure 4.34 both the 1st and 2nd modes (vane passing and tip gap variation frequencies) are plotted as a function of grid size. Here, the 1100k mesh was confirmed to be adequate for the calculations.

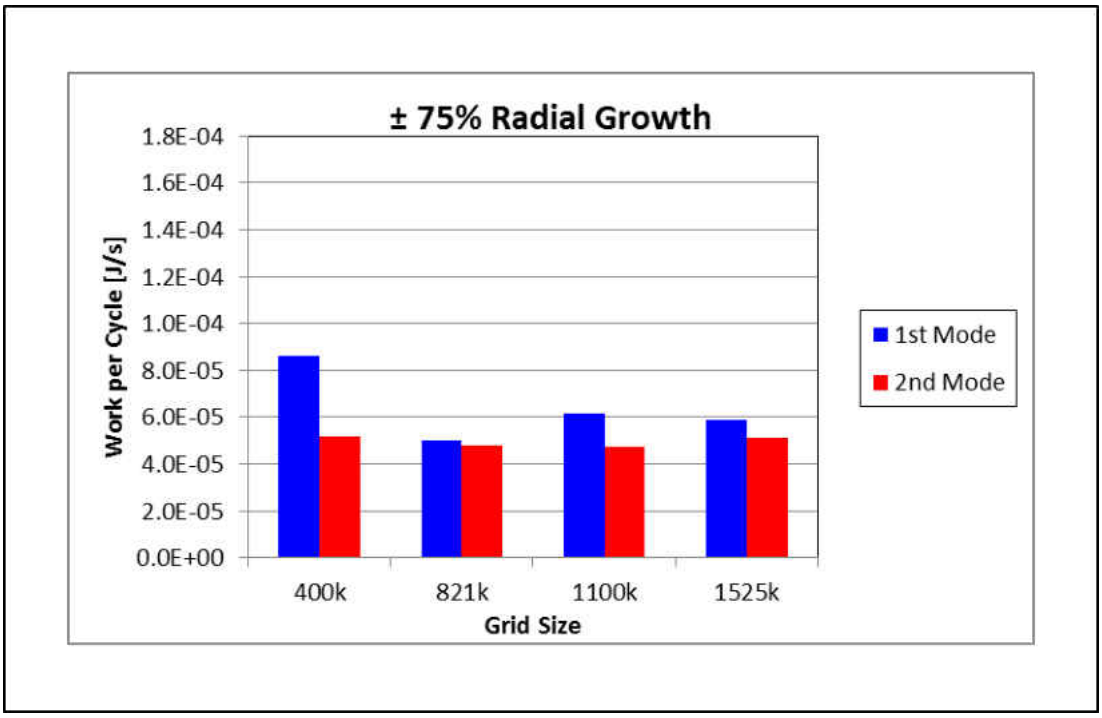

Figure 4.34: Grid Sensitivity Including Gap Variation

Further calculations were conducted for gap variations of: ±50%, ±25%, ±10% and ±5%. Figure 4.35 and Figure 4.36 show the work per cycle normalized by the work from the case with no gap variation, plotted vs. Gap Amplitude Variation for the 1st and 2nd harmonic modes. The figures show that the work for the 2nd mode changed linearly with gap variation, which was not surprising. However, the work generated by the 1st mode was only minimally affected by the gap variation (2nd mode). There was only a ~3% variation in work by going from the max variation of ±75% down to ±5%. Contrary to expectations, the work per cycle increased as the gap variation decreased between ±75% and ±25%. Below ±25% level, there was a reversal and the work dropped as the

gap got smaller, which was the expected trend. Unfortunately, it is difficult to assess whether this bend in the curve has a physical significance, or if it is just within the error of the calculation. The only conclusion that was clear from this plot was that the work per cycle was not strongly dependent on the amount of gap variation.

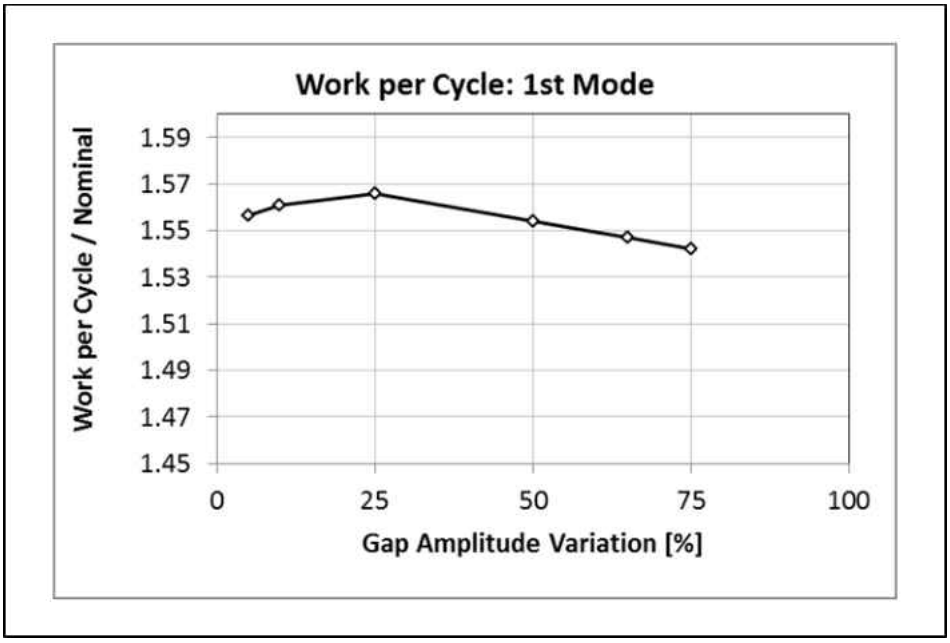

Figure 4.35: Work vs Gap Variation: 1st Mode

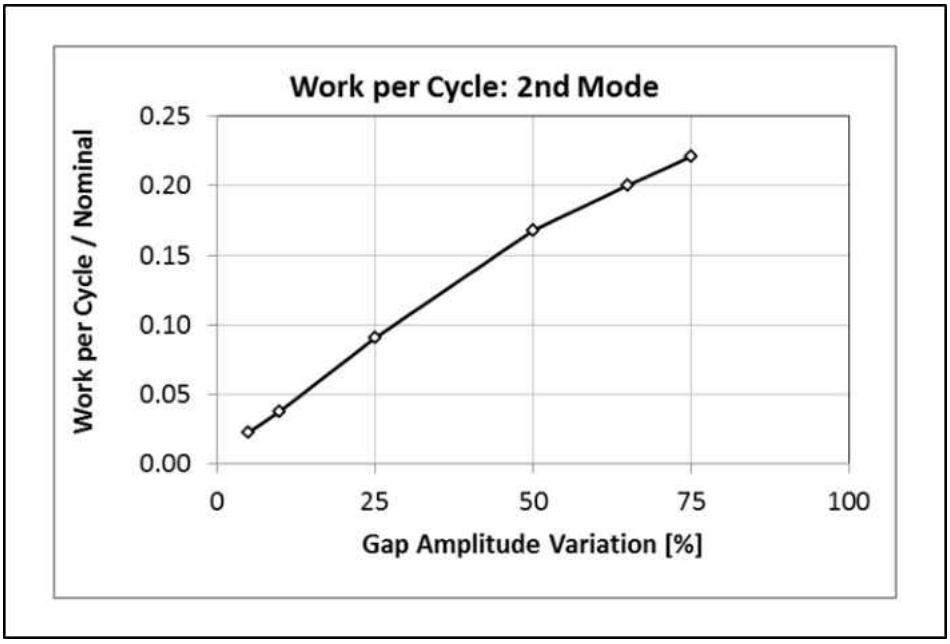

Figure 4.36: Work vs Gap Variation: 2nd Mode

CHAPTER 5: CONCLUSIONS

As mentioned earlier, the expectation was that the unsteady work contribution from the second mode (tip gap variation) would be significant. Instead, it was a relatively small contributor. This meant that the casing ovalization did not have a significant impact on the aeroelastic response of this blade. In order to confirm that this was in fact the correct conclusion from this study (a sanity check), and isolate any potential sources of error, the data was analyzed from a purely unsteady aerodynamic point of view, and a purely aeroelastic point of view. These conclusions are discussed next.

5.1 Unsteady Aerodynamic Impact

The aerodynamic effect of the casing ovalization was quantified by changes in the radial distribution of total-to-total efficiency, shown in Figure 5.1. This efficiency was calculated between a plane just upstream of the LE (in) and the Exit (out) plane of the Blade 1 domain, per Equation (5.1).

$$\eta_{tot-tot} = \frac{(Pt.out/Pt.in)^{\frac{\gamma-1}{\gamma}}-1}{(Pt.out/Pt.in)-1} \qquad (5.1)$$

This calculation was performed by doing a circumferential average for each plane to get a radial distribution of the pressures, then applying this equation at every radial point.

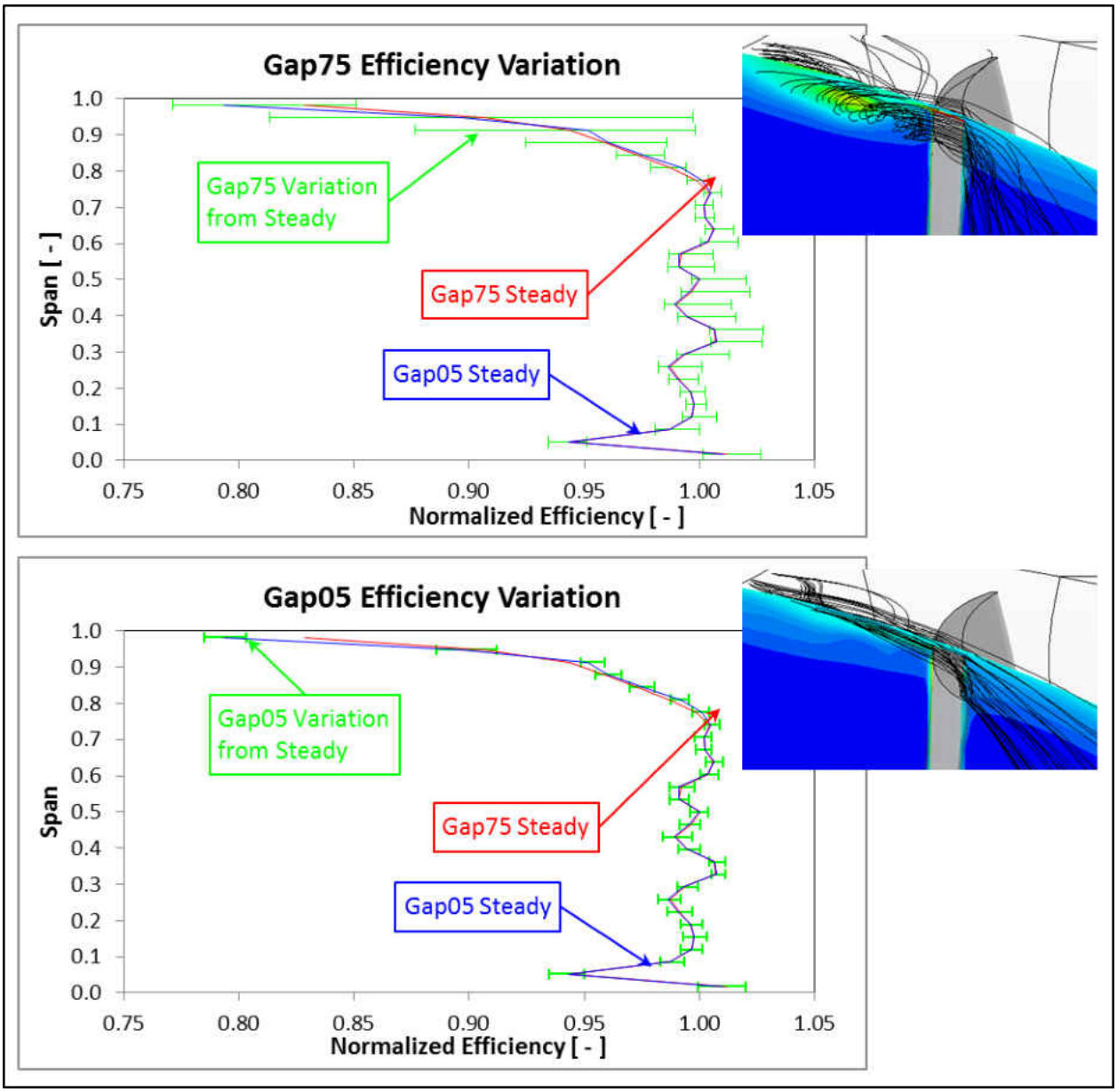

Figure 5.1: Total-to-Total Efficiency

The top chart in the figure shows the steady efficiencies for both gap variations (±75% and ±5%) as the solid red and blue lines, which were nearly identical. The green

error bars in the top chart showed the difference in the ±75% case between each time point, and the steady value. So these error bars say that there was a large scatter in efficiency when the case had the maximum ovalization. This of course makes sense, since the large gap showed larger entropy levels (low efficiency), while the small gap showed the opposite.

The bottom chart shows the same steady efficiencies (solid red and blue lines), but now the green error bars represent the efficiency scatter for the ±5% gap variation. This plot showed a much smaller efficiency scatter, confirming that a smaller amount of ovalization would correspondingly cause a smaller effect on efficiency.

As a further check, the points at 50% and 90% spans were plotted versus time point (i.e. circumferential location around the wheel), as shown in Figure 5.2. The figure shows that at 50% span (top chart), the unsteady efficiency (blue line) oscillated about the steady efficiency (red line) with low amplitude, so not much impact at mid-span. A similar oscillation was shown at 90% span (bottom chart), but with a much greater amplitude. So the large casing ovalization did experience a significant difference in efficiency in an instantaneous sense (good efficiency at the tight gap locations / poor efficiency at the large gap locations). However, the sinusoidal shape of the curve suggested that if it was integrated over time (or circumferential location), the good and bad efficiency locations would balance each other out giving a net zero effect.

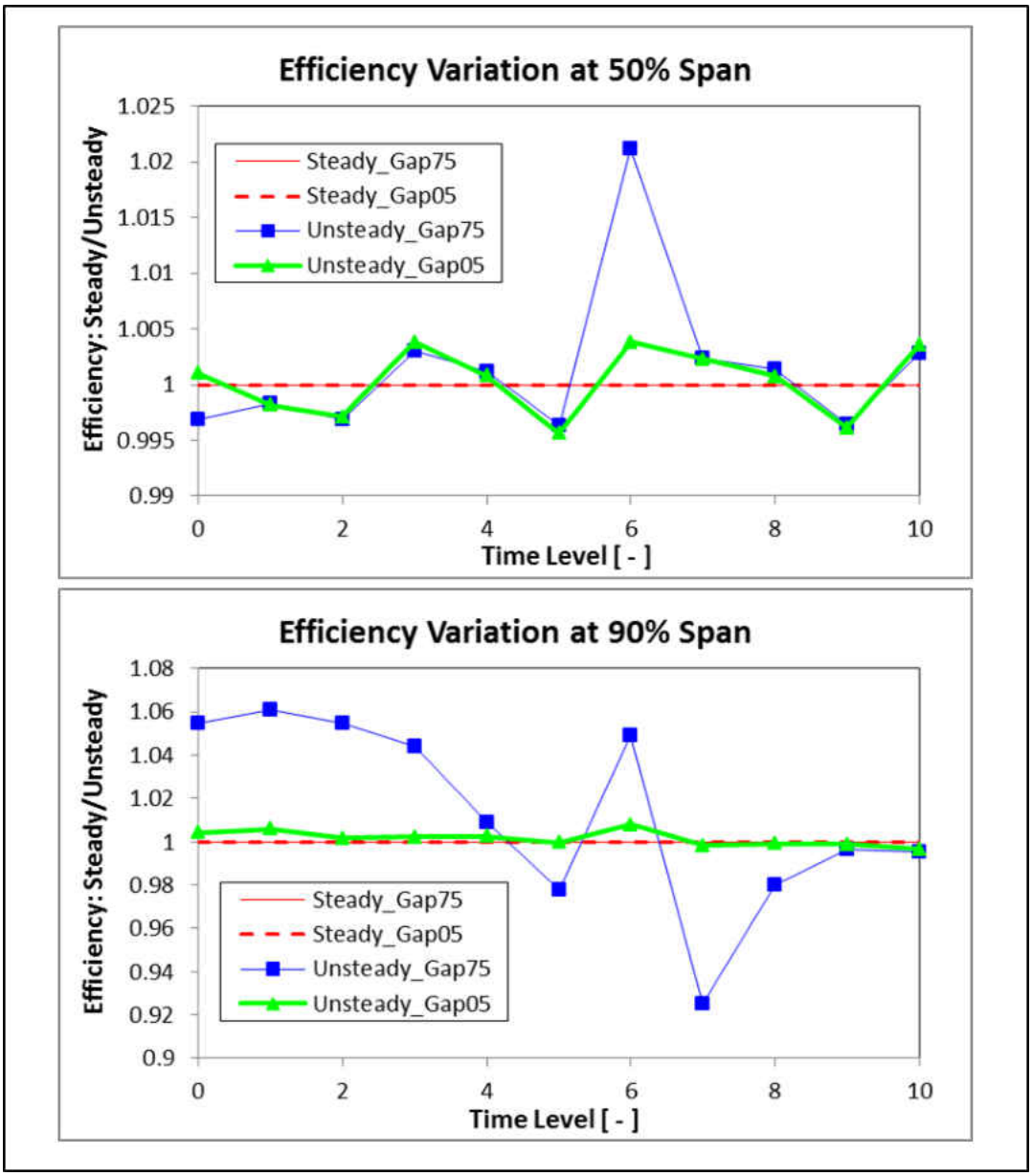

Figure 5.2: Efficiency Variation Over Time

A final check of the unsteady aero was to make three unsteady runs of different constant gaps (175%, 100% and 25% of the nominal gap). Figure 5.3 shows the radially

averaged efficiencies (condensing the radial distribution into one value) for these three cases (labeled Mode0), normalized by the 100% gap (nominal gap) case. Clearly, the rotor efficiency was pretty linear with the gap size. So this confirms that the model predicted good efficiency with the small gap, and vice versa with the large gap. Also, the loss in efficiency in the large gap was roughly the same magnitude as the gain in the small gap. This helps to clarify why there was a cancelling effect between the small and large gaps. The figure also highlights the fact that the steady efficiency was higher than the unsteady efficiency (~3.5% - 4% higher). This is likely due to unsteady effects (that generate losses) being averaged out by the steady solver.

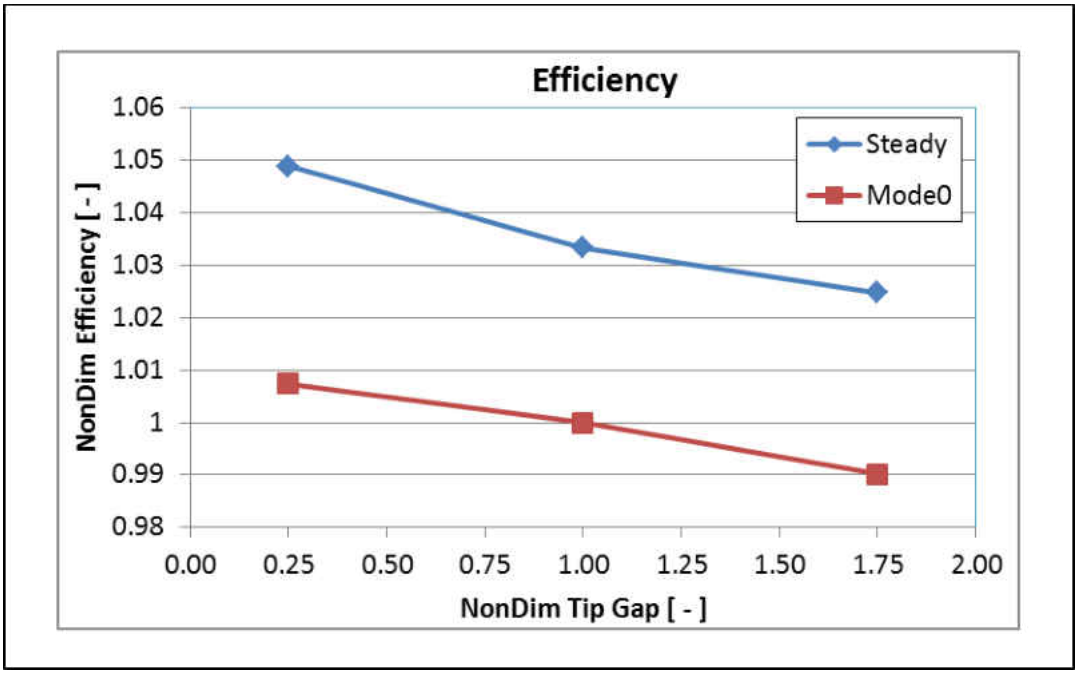

Figure 5.3: Constant Gaps Efficiency

5.2 Aeroelastic Impact

The second approach to verify the work per cycle results from Figure 4.35 was to look at the modal displacements in more detail. Figure 5.4 and Figure 5.5 below, show the unsteady work on the surface of the blade for the two extremes of tip gap variation amplitudes. The plots also show the two main contributors, unsteady pressure and modal displacement, along with the resulting work. As it is evident, the changes in the unsteady pressure on the airfoil surface were negligible between Gap75 and Gap05; the unsteady work differences were negligible as well. However, the CFD models showed that the two different gap extremes had a significantly different tip vortex structures in an instantaneous manner. So the question remained whether the work per cycle simply followed the counter balancing effect shown in aero efficiency, or if the mode shape itself could be the reason why the ovalization did not seem to impact the work per cycle. The reason to suspect the mode shape was that the deflection analyzed was a chord-wise second bending mode. This particular deflection exhibits a “C” shape (LE and TE moves in one direction, while the mid-chord in the opposite direction), so it could be that the work from the LE and TE counterbalanced the work from the center of the airfoil. One way to eliminate this uncertainty was to analyze a different mode shape in which the entire airfoil tip moved in the same direction (i.e. one of the flexural modes).

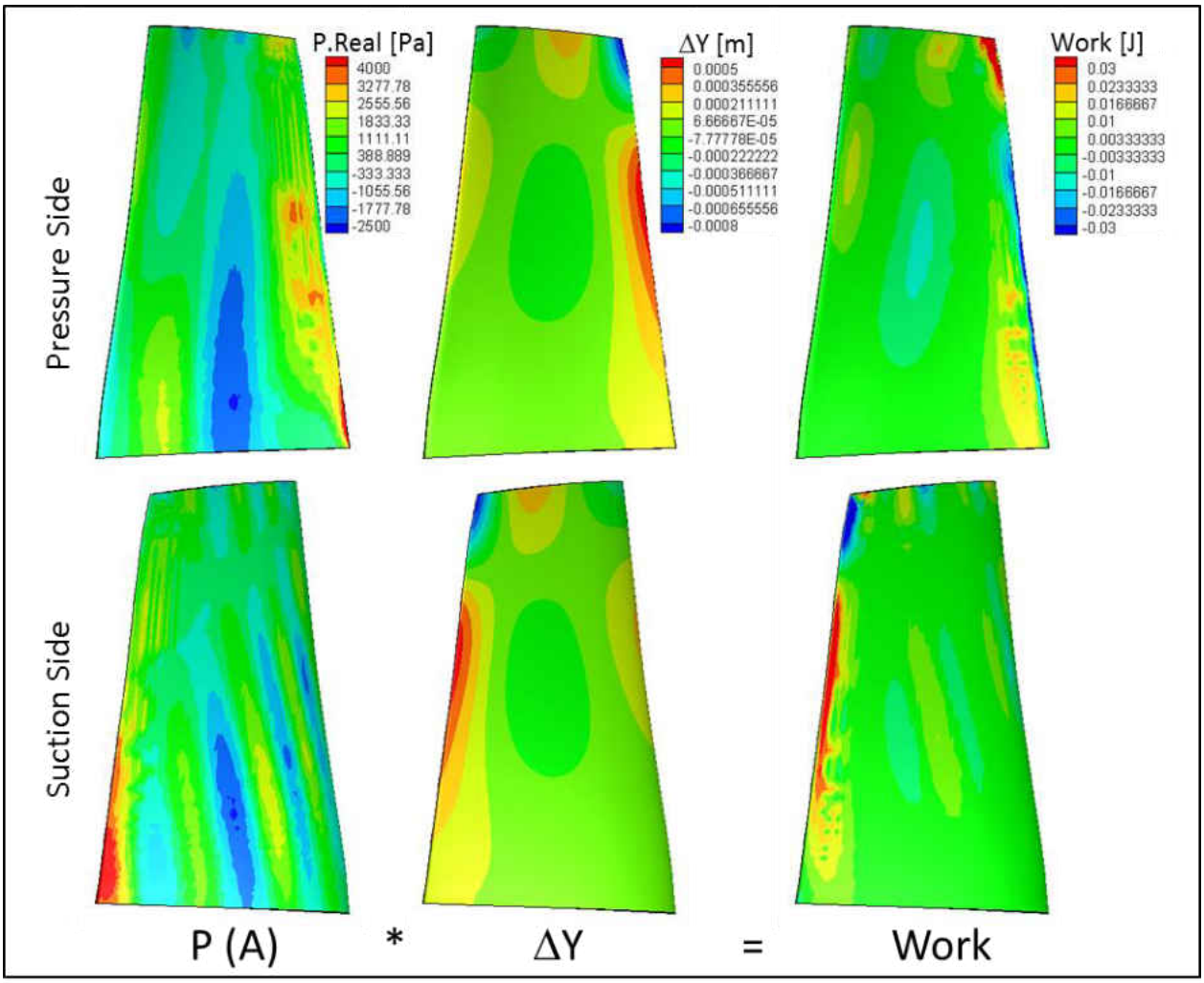

Figure 5.4: Unsteady Work: ±75% Gap

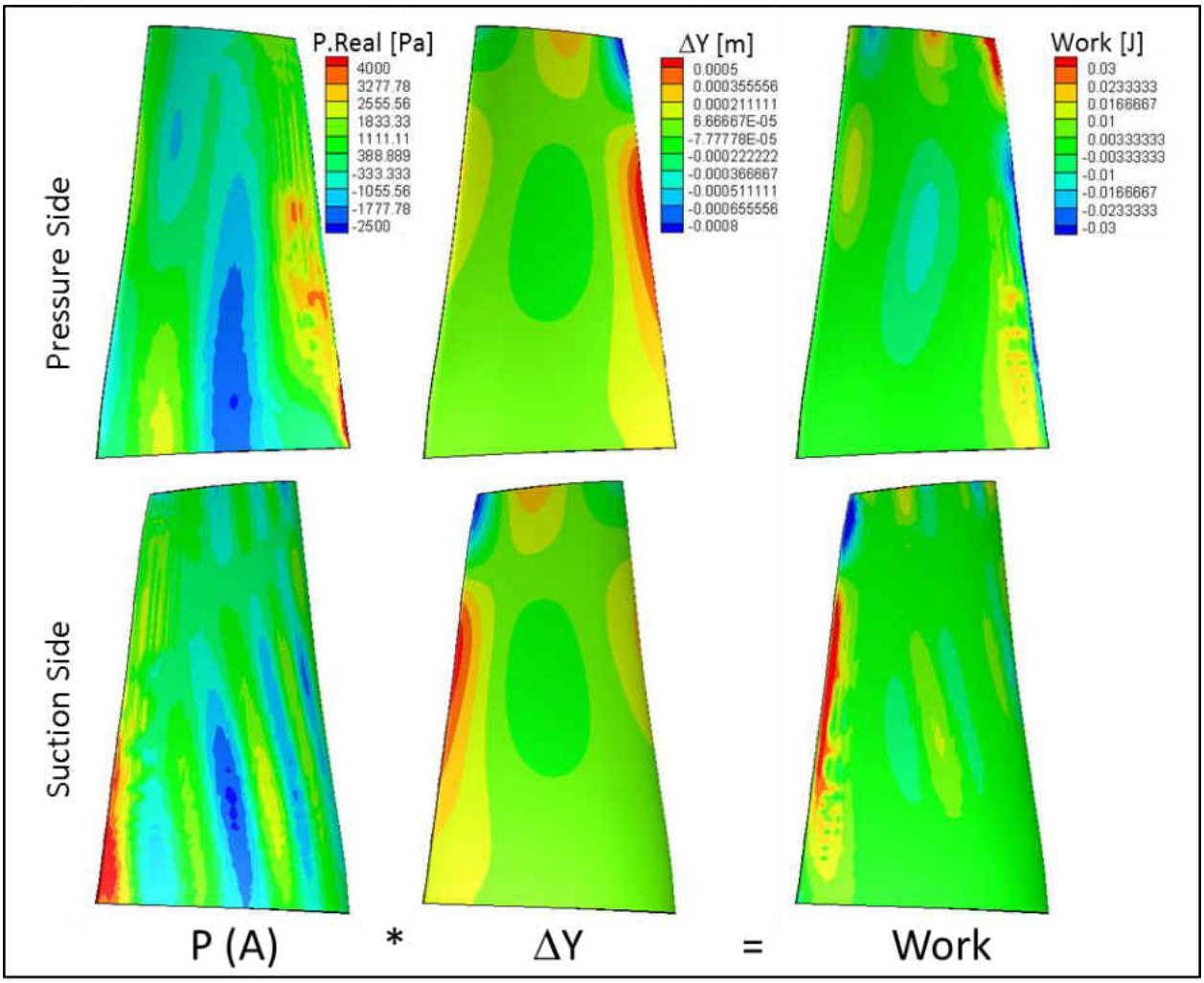

Figure 5.5: Unsteady Work: ±5% Gap

Therefore, as a purely academic exercise, all the Eigen modes extracted (total of 36) in the FEM were utilized in the calculation of the work per cycle for the largest and smallest gap variations. In general, it would not be valid to compare the work per cycle from two different Eigen modes because they occur at different frequencies. So they have different levels of energy and would not get excited by the same harmonics from the unsteady flow. So the point of this trade study was simply to determine if a different blade deflection could be more sensitive to the gap variation. Also, since the mode shape deflections for the analysis were normalized to unity (instead of the mass matrix), then the corresponding work contains this normalization and the different amplitudes of the deflections were not a factor.

In Figure 5.6 the circumferential deflections for some of the 36 Eigen modes are shown. Mode 13 is the chord-wise second bending deflection used up to this point. Other deflections to note are the flexural (bending) modes (1^{st} bending=mode1; 2^{nd} bending=mode4), because they have the entire tip moving in the same direction.

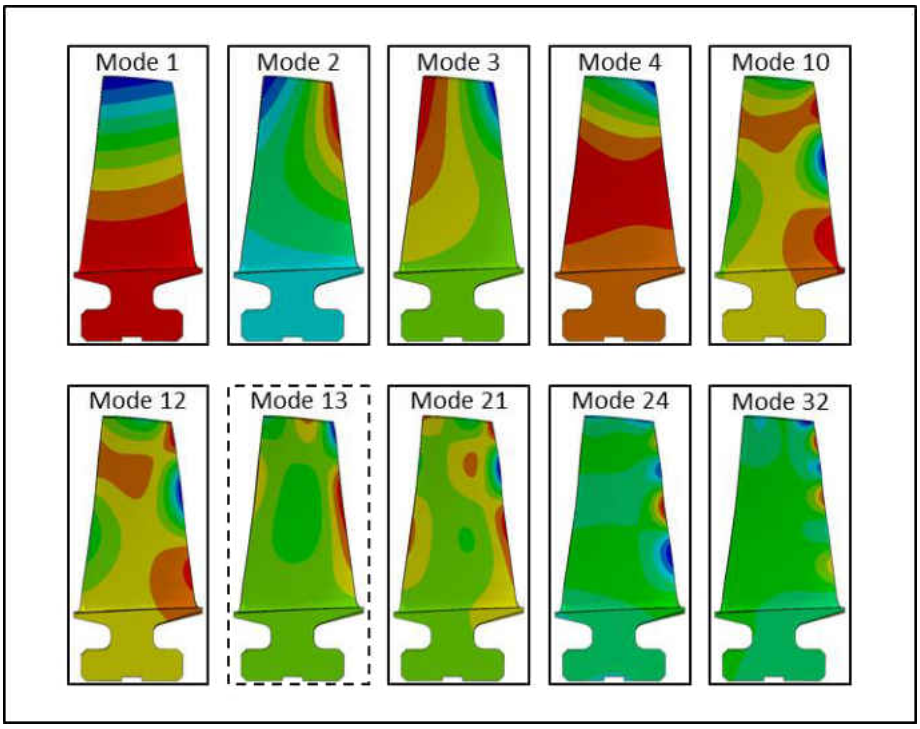

Figure 5.6: Eigen Vectors from all modes

The corresponding work per cycle for all modes was plotted and normalized by the work in mode 1, as shown Figure 5.7. In the figure, the blue bars correspond to the gap variation of ±75%, and the red bars to the ±5% case.

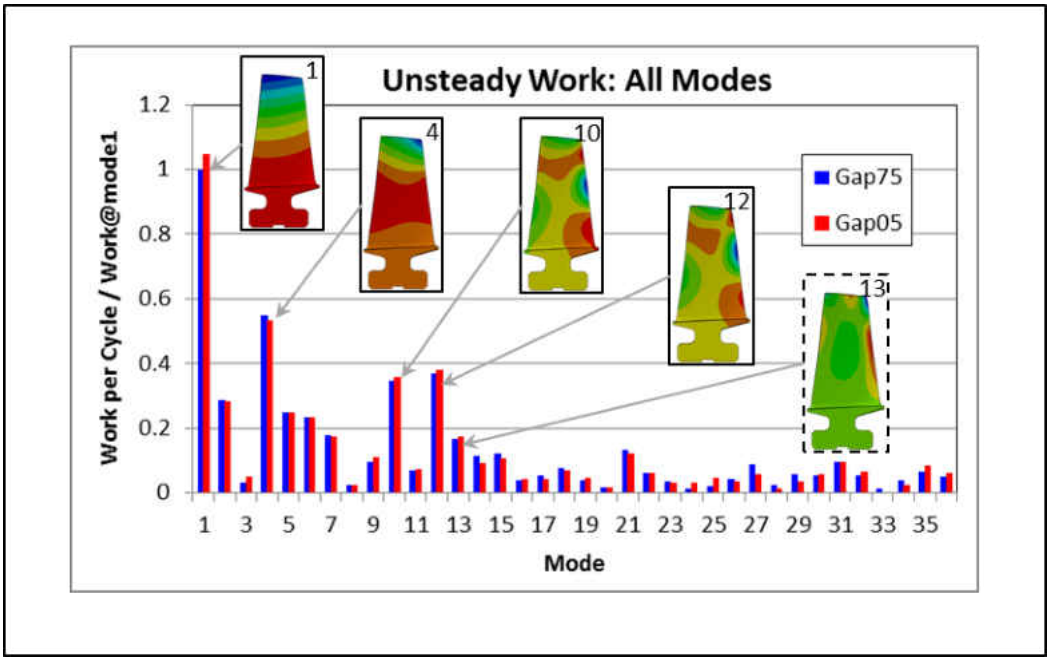

Figure 5.7: Work per Cycle from all modes

As expected, the 1st bending mode (mode #1) resulted in the largest work per cycle. Next, was the 2nd bending mode (mode #4) at roughly half the level of mode 1. Modes 10 and 12 had the next highest work; they appeared to be a 3rd bending mode, although not as easily identified. The last mode highlighted was the 13th mode, which was the one used previously. The figure also confirms the general expected trend that the higher modes are most often not a problem (low work value). They occur at higher frequencies (shown in the next figure), so they are more difficult (not impossible) to excite because they require more energy. They are often referenced as “high energy” modes, and have intricate deflections (see mode 24 and 32 in Figure 5.6). So in this hypothetical case where all the modes were excited by the same unsteady aerodynamic

loading, the general trend of work level dropping from the lower modes to the higher ones was in keeping with expectations.

Next, the difference between the two gap variation conditions at each mode was plotted in Figure 5.8; the value of the y-axis was defined as:

$$WorkVariation = \frac{(Gap75 - Gap05)}{Gap75@mode1} * 100 \qquad (5.2)$$

On the same figure, the frequency for each mode is plotted on the right y-axis, and normalized by the frequency of the 1st mode for reference.

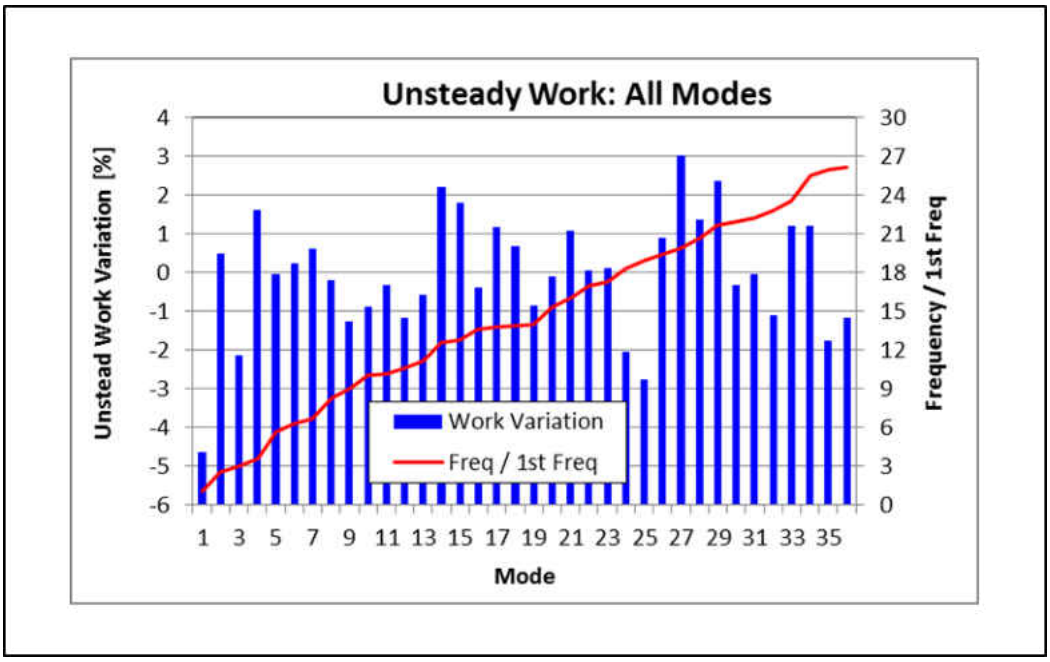

Figure 5.8: Sensitivity to Ovalization

In this plot, a positive value for the bars (left y-axis) means that ovalization increased the work, which is a negative effect on the aeromechanic response, and vice versa. This figure shows that even when the casing had the largest ovalization (gap variation ±75%), there was little difference in the work per cycle, relative to a small amount of ovalization (±5% gap variation). This was true for all of the modes examined (most had <2% difference), with only mode1 showing a slightly higher dependence on the ovalization (~ -4.5%). As a matter of fact, there was not even a trend identified in the direction in which the ovalization affected each mode. For some modes there was a positive impact (% change was negative), while for other modes the ovalization had a negative impact (% change was positive).

5.3 Concluding Remarks

The circumferentially varying tip gap was expected to introduce an excitation in addition to that produced by the downstream vane. The analyses conducted here demonstrated this as quantified by the work per cycle of the second mode. Also as expected, the work for this second mode increased with the size of the gap variation. Furthermore, it was expected that this new excitation would be a significant contributor to the overall work per cycle. However, the work contribution from the gap variation (2nd mode) was very small compared to the work contribution from the downstream vane (1st mode). The final result was that the gap variation (casing ovalization) did not have a significant impact on the aeroelastic response of the blade.

The unsteady efficiency showed that the models behaved as expected when examined at instantaneous “time” points (different locations around the wheel). However, there was an unexpected canceling effect between the large and small gap locations. Furthermore, this effect was carried onto the work per cycle, even for mode shapes with large tip participation.

This averaging effect of ovalization shows a potential to leverage it for the benefit of the engine. For example: a stall condition is generally described as separated flow in one airfoil pushing the flow on the adjacent blade, hence causing it to separate. This is continued in a cascading manner to the point where enough separation generates stalling of the row. The ovalization showed an effect opposite to this cascading deterioration. So if the casing is contoured correctly, it can average out the negative influence from one airfoil with the rest of the wheel, hence preventing (or delaying) a stall condition. Of course this would require further study in a follow-on project.

Intuitively, it was expected that the circumferentially varying gap would increase the aeromechanic response of the blade, but experience does not automatically point to casing ovalization as a main suspect for aeromechanic field issues. Most forced response problems typically come from excitations occurring at integer multiples of the surrounding hardware counts and/or inlet disturbances.

Permission for Use Statement:

The content of this paper is copyrighted by Siemens Energy, Inc. and is licensed to the University of Central Florida for publication and distribution only. Any inquiries regarding permission to use the content of this paper, in whole or in part, for any purpose must be addressed to Siemens Energy, Inc. directly.

APPENDIX
LESSONS LEARNED

In the process of obtaining the results reported in the previous section, there were many failed calculations conducted. These failed attempts still provided valuable insights into developing the methodology finally employed. This section provides a brief overview of the major aspects that should be considered when undertaking an analysis such as this:

1. Software Versions: For the StarCCM+ steady solution there were several turbulence models available. Several were tested and did not show significant differences in the flow variables investigated. This included the SST model, which was picked for the initial runs in this project. This was conducted in version 8.04 of the software; however, later runs were executed with the newer version 9.06. Unfortunately, the later version only allowed for the k-w model to be used with the harmonic balance solver. Use of the previous turbulence with the new version simply crashed immediately. There were pros and cons to reverting to the previous version, and in the end, it was decided to use the latest version. This meant that there was a significant amount of re-work necessary to run everything with the new version. Of course this could not have been foreseen and avoided. So the lesson learned was to keep consistency in the software revision used (i.e. not switch in the middle of the project) and fully document the version and different options used.
2. Grid Sensitivity: The initial grid sensitivity study conducted increased overall mesh density and also reduced the 1st cell height. This did not have a noticeable effect on the CFX and LinearTrace solutions, which was a little

unexpected, but a good thing. It just meant that both of these solvers (CFX and LinearTrace) were insensitive to a grid refinement beyond the density already achieved. On the other hand, this type of grid refinement had a strange effect on the StarCCM+ solution. At first glance, the residuals and mass flow convergence did not reveal a major problem. However, when looking at the flow variables on the surface of the blade, it was evident that the solution was not fully converged. Figure A 1 below shows a case that seemed otherwise converged, but close inspection at the blade surface steady pressure revealed an un-converged pressure loading. This was due to the “all y+ models” option of the harmonic balance turbulence model. Simply turning this option off (as well as other attempted work-arounds) did not resolve the problem, so the grid refinement had to be redone. In the end the grid density was increased in all three Cartesian directions, but the 1st cell height was left relatively large; at the level of the coarsest mesh. This provided a grid independent solution with surface values within reasonable/expected distributions.

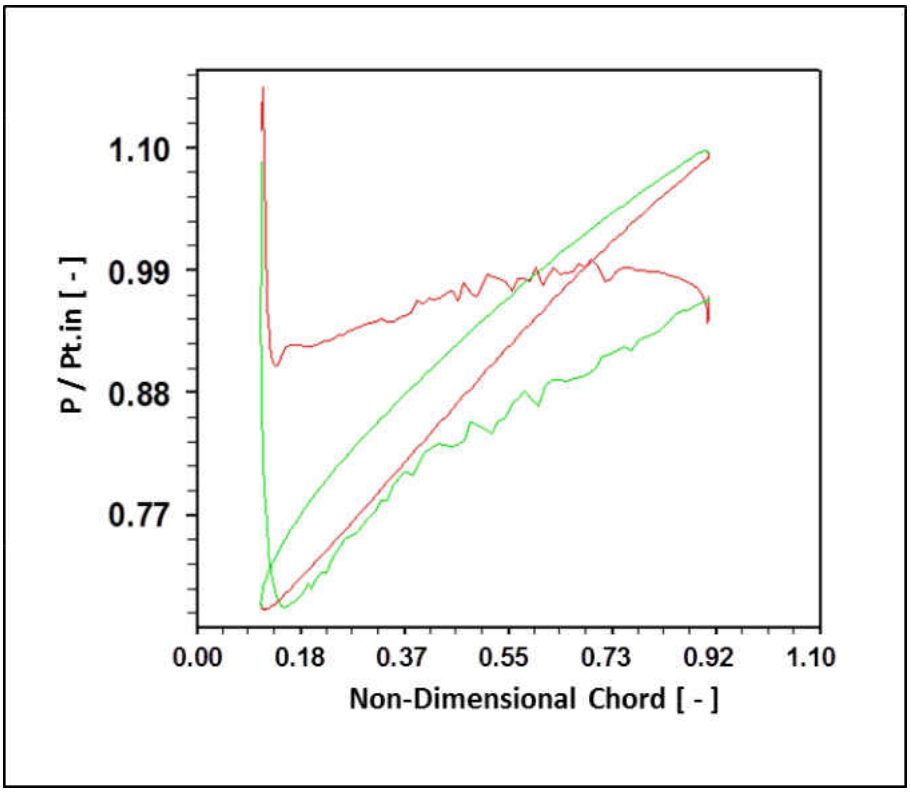

Figure A 1: Un-converged Blade Loading

REFERENCES

[1] Zhang, H., Deng, X., Chen, J., Huang, W. (2005). Unsteady tip clearance flow in an isolated axial compressor rotor. Journal of Thermal Science, v 14, n 3, pp 211-219.

[2] Du, J., Lin, F., Zhang, H., Chen, J. (2008). Numerical Simulation on the Effect of Tip Clearance Size on Unsteadiness in Tip Clearance Flow. Journal of Thermal Science v 17, n 4, pp 337-342.

[3] Kang, Y., Kang, S. (2006). Prediction of the fluid induced instability force of an axial compressor. Proceedings of FEDSM2006 (Fluids Engineering Summer Meeting).

[4] Im, H., Chen, X., Zha, G. (2010). Detached Eddy Simulation of Unsteady Stall Flows of a Full Annulus Transonic Rotor. Proceedings of ASME Turbo Expo 2010: Power for Land, Sea and Air, June 14-18, 2010, Glasgow, UK.

[5] Chen, J., Hathaway, M. (2007). Pre-Stall Behavior of a Transonic Axial Compressor Stage via Time-Accurate Numerical Simulation. ASME Turbo Expo 2007: Power for Land, Sea and Air, May 14-17, 2007, Montreal, Canada.

[6] Moffatt, S., He, L. (2003). Blade forced response prediction for industrial gas turbines part I: Methodologies. American Society of Mechanical Engineers, International Gas Turbine Institute, Turbo Expo (Publication) IGTI, v 4, p 407-414, 2003, Proceedings of the ASME Turbo Expo 2003. Volume 4: Oil and Gas Applications, Structures and Dynamics, Scholar Lecture, Conference: 2003 ASME Turbo Expo, June 16, 2003 - June 19, 2003, Sponsor: International Gas Turbine Institute, ASME, .

[7] Moffatt, S., Ning, W., Li, Y., Wells, R., He, L. (2005). Blade forced response prediction for industrial gas turbines. Journal of Propulsion and Power, v 21, n 4, p 707-714, July/August.

[8] Mailach, R., Lehmann, I., Vogeler, K. (2008). Periodical unsteady flow within a rotor blade row of an axial compressor - Part II: Wake-tip clearance vortex interaction. Journal of Turbomachinery, v 130, n 4, October.

[9] Kang, Y., Kang, S. (2010). Prediction of the nonuniform tip clearance effect on the axial compressor flow field. Journal of Fluids Engineering, Transactions of the ASME, v 132, n 5, p 0511101-0511109, May.

[10] Besem, F., Kamrass, J., Thomas, J., Tang, D., Kielb, R. (2014). Vortex-induced vibration and frequency lock-in of an airfoil at high angles of attack. Proceedings of the ASME Turbomachinery Exposition, ASME Turbo Expo 2014, June 16 - 20, 2014, Dusseldorf, Germany.

[11] DLR (n.d.). Trace wiki portal. http://www.trace-portal.de/wiki/index.php/Main_Page.

[12] Au-Yang, M. (2001). Flow-induced vibration of power and process plant components. New York : ASME Press, 2001 (original from University of Michigan).

[13] Fric, T., Villareal, R., Auer, R.O., James, M.L., Ozgus, D., Staley, T.K. (1998). Vortex Shedding From Struts in an Annular Exhaust Diffuser. Journal of Turbomachinery, January 1998, v 120, pp 187.

[14] Kielb J., Hoyniak D., Yeo S., (2005). Probabilistic Assessment of Variability in Vibratory Response from Strain Gage & NSMS Measured During Engine Tests. HCF Conference 2005, New Orleans, LA..

[15] Pullan, G., Young, A., Day, I., Greitzer, E., Spakovszky, Z. (2012). Origins and structure of spike-type rotating stall. Proceedings of ASME Turbo Expo 2012 GT2012 June 11-15, 2012, Copenhagen, Denmark.

[16] Platzer, M., Carta, F. (1987). Agard manual on aeroelasticity in axial-flow turbomachines volume 1: unsteady turbomachinery aerodynamics. Specialized Printing Services Limited, Copyright © AGARD.

[17] Tannehill J.C., Anderson, D.A., Pletcher, R.H. (1997). Computational Fluid Mechanics and Heat Transfer 2nd Ed.. Copyright © 1997 Taylor & Francis.

[18] Cumpsty, N.A. (1989). Compressor Aerodynamics. Copyright © 1989 by Longman Group UK.

[19] Verdon, J. M. (1989). The Unsteady Aerodynamic Response to Arbitrary Modes of Blade Motion. Journal of Fluids and Structures, v 3, pp 255-274.

[20] Dobrzynski, B., Saathoff, H., Kosyna, G. (2008). Active flow control in a single-stage axial compressor using tip injection and endwall boundary layer removal. Proceedings of the ASME Turbo Expo 2008: Power for Land, Sea and Air, June 9-13, 2008, Berlin,Germany.

[21] Frechette, L.G., McGee, O.G., Graf, M.B. (2004). Tailored Structural Design and Aeromechanical Control of Axial Compressor Stall Part II - Evaluation of

Approaches. Transactions of the ASME. The Journal of Turbomachinery, v 126, n 1, 52-62, Jan. 2004, ISSN: 0889-504X, DOI: 10.1115/1.1644555, Publisher: ASME, USA.

[22] Jothiprasad, G., Murray, R., Essenhigh, K., Bennett, G., Saddoughi, S., Wadia, A., Breeze-Stringfellow, A. (2011). Control of tip-clearance flow in a low speed axial compressor rotor with plasma actuation. Journal of Turbomachinery, v 134, n 2, June 29.

[23] Geng, S., Zhang, H., Chen, J., Huang, W. (2007). Unsteady tip clearance flow pattern in an isolated axial compressor rotor with micro tip injection. Journal of Thermal Science, v 16, n 4, p 309-320, November.

[24] Vo, H., Tan, C., Greitzer, E. (2008). Criteria for Spike Initiated Rotating Stall. Journal of Turbomachinery, JANUARY 2008, Vol. 130 / 011023-1.

[25] Hah, C., Voges, M., Mueller, M., Schiffer, H. (2010). Characteristics of tip clearance flow instability in a transonic compressor. Proceedings of the ASME Turbo Expo, v 7, PARTS A, B, AND C, pp 63-74.

[26] Bae, J., Breuer, K., Tan, C. (2005). Active control of tip clearance flow in axial compressors. Journal of Turbomachinery, v 127, n 2, pp 352-362, April.

[27] Weichert, S.A. (2011). Tip Clearance Flows in Axial Compressors: Stall Inception and Stability Enhancement. PhD Dissertation, Cambridge.

[28] Doukelis, A., Mathioudakis, K., Papailiou, K. (1998). Effect of tip clearance gap size and wall rotation on the performance of a high-speed annular compressor cascade. International Gas Turbine & Aeroengine Congress & Exhibition, Stockholm, Sweden — June 2–June 5.

[29] Sakulkaew, S., Donahoo, E., Cornelius, C., Tan, C.S., Montgomery, M. (2012). Compressor efficiency variation with rotor tip gap from vanishing to large clearance. Proceedings of ASME Turbo Expo 2012 GT2012 June 11-15, 2012, Copenhagen, Denmark.

[30] Wang, Z., Jia, X., Cai, R. (2002). Influence of blade tip clearance shapes on aerodynamic performance of an axial flow compressor stator. Proceedings of the Institution of Mechanical Engineers, Part A: Journal of Power and Energy, v 216, n 5, pp 395-401.

[31] Mohan, K., Guruprasad, S.A. (1994). Effect of axially non-uniform rotor tip clearance on the performance of a high speed axial flow compressor stage. American Society of Mechanical Engineers (Paper), pp 1-8.

[32] Ma, H., Zhang, J., Zhang, J. (2010). Experimental study of effects of one kind of tangentially non-uniform tip clearance on the flow field at an exit of a compressor cascade passage. Journal of Thermal Science, v 19, n 1, p 7-13, March 2010, ISSN: 10032169, DOI: 10.1007/s11630-010-0007-7.

[33] Glen S., Dwain D., Grant I., David G. (2010). The performance of a generic non-axisymmetric end wall in a single stage, rotating turbine at on and off-design conditions. Proceedings of ASME Turbo Expo 2010: Power for Land, Sea and Air GT2010-22006.

[34] Praisner, T.J., Allen-Bradley, E., Grover, E.A., Knezevici, D.C., Sjolander, S.A. (2007). Application of non-axisymmetric endwall contouring to conventional and high-lift turbine airfoils. ASME Turbo Expo 2007: Power for Land, Sea and Air GT2007-27579.

[35] Xudong, H., Haixin, C., Song, F. (2008). CFD Investigation on the circumferential grooves casing treatment of transonic compressor. Proceedings of the ASME Turbo Expo, v 6, n PART A, pp 581-588.

[36] Nezym, V. (2007). A statistical model for the effect of casing treatment recesses on compressor rotor performance. Experimental Thermal and Fluid Science 31 (2007) 1165–1176.

[37] Hajmrie, K., Fiala, P., Chilkowich, A., Shiembob, L. (2004). Abradable Seals for Gas Turbines and Other Rotary Equipment. Proceedings of the ASME Turbo Expo 2004, v 4, pp 673-682.

[38] Lu, X., Zhu, J., Chu, W., Wang, R. (2005). The effects of stepped tip gap on performance and flowfield of a subsonic axial-flow compressor rotor. Proceedings of the ASME Turbo Expo, v 6 PART A, pp 373-380.

[39] Zhu, J., Sun, L., Lu, X. (2005). Experimental investigation on the layout of tip clearance for an axial-flow compressor rotor. 43rd AIAA Aerospace Sciences Meeting and Exhibit - Meeting Papers, p 8671-8679, 2005, 43rd AIAA Aerospace Sciences Meeting and Exhibit - Meeting Papers, Conference: 43rd AIAA Aerospace Science.

[40] Cameron, J., Bennington, M., Ross, M., Morris, S., Corke, T. (2007). Effects of steady tip clearance asymmetry and rotor whirl on stall inception in an axial compressor. ASME Turbo Expo 2007: Power for Land, Sea and Air, May 14-17, 2007, Montreal, Canada.

[41] Morris, S. C., Cameron, J. D., Bennington, M. A., McNulty, G. S., Wadia, A. (2008). Performance and short length-scale disturbance generation in an axial compressor with non-uniform tip clearance. Proceedings of the ASME Turbo Expo, v 6, n PART A, p 667-679.

[42] Hah, C., Bergner, J., Schiffer, H. (2008). Tip clearance vortex oscillation, vortex shedding and rotating instabilities in an axial transonic compressor rotor. Proceedings of the ASME Turbo Expo 2008: Power for Land, Sea and Air, June 9-13, 2008, Berlin,Germany.

[43] Campbell, W. (1924). The protection of steam trubine disk wheels from axial vibration. General Electric Review, Vol XXVII, No 6, June.

[44] Custer, C. (2009). A Nonlinear Harmonic Balance Solver for an Implicit CFD Code: OVERFLOW 2. Dissertation, Department of Mechanical Engineering and Materials Science in the Graduate School of Duke University.

[45] Mayorca, M., Vogt, D., Fransson, T., Martensson, H. (2012). A New Reduced Order Modeling for Stability and Forced Response Analysis of Aero-Coupled Blades Considering Various Mode Families. Journal of Turbomachinery, v 134, n 5, May 8.

[46] Vahdati, M., Sayma, A., Imregun, M., Simpson, G. (2007). Multibladerow forced response modeling in axial-flow core compressors. Journal of Turbomachinery, v 129, n 2, pp 412-422, April.

[47] Schmitt, S. (2003). Simulation of Flutter and Forced Response in Turbomachinery Blade Rows. D L R - Forschungsberichte, n 22, 2003, Language: German.

[48] Im, H., Zha, G. (2012). Simulation of non-synchronous blade vibration of an axial compressor using a fully coupled fluid/structure interaction. Proceedings of ASME Turbo Expo 2012, June 11-15, 2012, Copenhagen, Denmark.

[49] Wu, X., Vahdati, M., Sayma, A., Imregun, M. (2005). Whole-annulus aeroelasticity analysis of a 17-bladerow WRF compressor using an unstructured Navier–Stokes solver. International Journal of Computational Fluid Dynamics, Vol. 19, No. 3, 2005, 211–223.

[50] Zhang, M., Hou, A., Wang, Q. (2011). Numerical investigation of blade vibration response induced by inlet distortion in axial compressor. Tuijin Jishu/Journal of Propulsion Technology, v 32, n 4, p 466-470+503, August.

[51] Gorrell, S., Okiishi, T., Copenhaver, W. (2002). Stator-rotor interactions in a transonic compressor: Part 2 - Description of a loss producing mechanism. Proceedings of the ASME TURBO EXPO 2002, June 3-6, 2002, Amsterdam, The Netherlands.

[52] Hutton, T., Leger, T., Johnston, D., Wolff, J. (2004). High spatial resolution upstream forced response in a transonic compressor. Journal of Propulsion and Power, v 20, n 4, p 751-754, July/August.

[53] Di Mare, L., Simpson, G., Mueck, B., Sayma, A. (2006). Effect of bleed flows on flutter and forced response of core compressors. Proceedings of the ASME Turbo Expo, v 5 PART B, p 1115-1122.

[54] Bailie, S., Ng, W., Wicks, A., Copenhaver, W. (2002). Effects of flow control on forced response and performance of a transonic compressor. American Society of Mechanical Engineers, International Gas Turbine Institute, Turbo Expo (Publication) IGTI, v 1, p 67-74.

[55] Chen, J., Webster, R., Hathaway, M., Herrick, G., Skoch, G. (2006). Numerical simulation of stall and stall control in axial and radial compressors.. Collection of Technical Papers - 44th AIAA Aerospace Sciences Meeting, v 7, p 4868-4880, 2006, Collection of Technical Papers - 44th AIAA Aerospace Sciences Meeting.

[56] Hah, C., Bergner, J., Schiffer, H. (2006). Short length-scale rotating stall inception in a transonic axial compressor – criteria and mechanisms. Proceeding of GT2006 ASME Turbo Expo 2006: Power for Land, Sea and Air, May 8-11, 2006, Barcelona, Spain.

[57] Dhandapani, S., Vahdati, M., Imregun, M. (2008). Forced response and surge behaviour of IP core-compressors with ice-damaged rotor blades. Proceedings of ASME Turbo Expo: Power for Land, Sea, and Air, June 9-13, 2008, Berlin, Germany.

[58] Gorrell, S., Yao, J., List, M. (2009). Full annulus high fidelity fan and compressor simulations. Department of Defense Proceedings of the High Performance Computing Modernization Program - Users Group Conference, HPCMP-UGC 2009, p 46-56.

[59] Vahdati, M. (2007). A numerical strategy for modelling rotating stall in core compressors. International Journal for Numerical Methods in Fluids, v 53, n 8, p 1381-1397, March 20.

[60] Li, J., Schmitt, S., Canon, D. (2015). Wake and Potential Interactions in a Multistage Compressor. Proceedings of the 14th International Symposium on

Unsteady Aerodynamics, Aeroacoustics & Aeroelasticity of Turbomachines ISUAAAT14, 8-11 September 2015, Stockholm, Sweden.

[61] Smith, N.R., Key, N. (2015). Flow Visualization for Investigating Stator Losses in a Multistage Axial Compressor. Experiments in Fluids, v 56, p 94.

[62] Thomson, W.T., Dahleh, M.D. (1998). Theory of Vibration with Applications, 5th Ed.. Copyright © 1998, 1993 by Prentice Hall, Inc..

[63] Takacs, G., Rohal-IIkiv, B (2012). Model Predictive Vibration Control. Copyright © Springer-Verlag London Limited.

[64] Mikolajczak, A.A., Arnoldi, R.A., Snyder, L.E., Stargardter, H. (1975). Advances in Fan and Compressor blade Flutter Analysis and Predictions. Journal of Aircraft, v 12, n 4, pp 325-332, April.

[65] Hall, K., Thomas, J., Ekici, K., Voytovich, D. (2003). Frequency Domain Techniques for Complex and Nonlinear Flows in Turbomachinery. American Institute of Aeronautics and Astronautics Paper 2003-3998.

[66] Ni, R., Sisto, F. (1976). Numerical Computation of Nonstationary Aerodynamics of Flat Plate Cascades in Compressible Flow. Transactions of the ASME:Journal of Engineering for Power, v 98, pp. 165–170..

[67] Bisplinghoff, R.L., Ashley, H., Halfman, R.L. (1995). Aeroelasticity. Copyright © 1995 by Addison-Wesley Publishing Company, Inc..

[68] Dowell, E.H., Crawley, E.F., Curtis, H.C., Peters, D.A., Scanlan, R.H., Sisto, F. (1995). A Modern Course in Aeroelasticity (3rd Ed.). Copyright © 1995 Springer Science+Business Media.

[69] Weisshaar, T.A (2012). Aeroelasticity, an introduction to fundamental problems. Purdue University © 1995 (3rd ed. 2012).

[70] Garrick, I.E., Reed, W.H. (1981). Historical Development of Aircraft Flutter. Journal of Aircraft, v 18, n 11, pp 897-912, November.

[71] Bilah, K.Y., Scanlan, R.H. (1991). Resonance, Tacoma Narrows bridge failure, and undergraduate physics textbooks. American Journal of Physics, v 59, n 2, February.

[72] Kielb, R. (2012). Aeromechanical Design of Turbomachinery Blades. Short course presented at Siemens Inc..

[73] Brandvik, T., Pullan, G (2010). SBLOCK: A Framework for Efficient Stencil-Based PDE Solvers on Multi-core Platforms. CIT 2010 : The 10th IEEE International Conference on Computer and Information Technology.

[74] Reid, C. (1969). The Response of Axial Flow Compressors to Intake Flow Distortion. Gas Turbine Conference & Products Show, Cleveland, Ohio, March 9-13, 1969, of The American Society of Mechanical Engineers.

[75] Im, H., Zha, G. (2012). EFFECTS OF ROTOR TIP CLEARANCE ON TIP CLEARANCE FLOW POTENTIALLY LEADING TO NSV IN AN AXIAL COMPRESSOR. Proceedings of ASME Turbo Expo 2012, June 11-15, 2012, Copenhagen, Denmark.

[76] El–Sayed, A., Ibrahim, M. (2010). Numerical Investigation of Different Tip Clearance Shape Effects on Performance of an Axial Flow Compressor Stage. The Online Journal on Power and Energy Engineering (OJPEE) v 1, n 2.

[77] Mailach, R., Vogeler, K. (2004). Aerodynamic blade row interactions in an axial compressor - Part II: Unsteady profile pressure distribution and blade forces. Journal of Turbomachinery, v 126, n 1, pp 45-51, January.